UC Santa Cruz

UC Santa Cruz Electronic Theses and Dissertations

Title

Fast Frequency Estimator Based on Extended Kalman Filter

Permalink

https://escholarship.org/uc/item/1p9249vz

Author

Jin, Lin

Publication Date

2020

Peer reviewed|Thesis/dissertation

eScholarship.org Powered by the California Digital Library
University of California

UNIVERSITY OF CALIFORNIA
SANTA CRUZ

FAST FREQUENCY ESTIMATOR BASED ON EXTENDED KALMAN FILTER

A dissertation submitted in partial satisfaction of the
requirements for the degree of

DOCTOR OF PHILOSOPHY

in

ELECTRICAL ENGINEERING

by

Lin Jin

March 2020

The Dissertation of Lin Jin
is approved:

Kenneth Pedrotti, Chair

Donald Wiberg

Sung-Mo Steve Kang

Ahmet Ali Yanik

Quentin Williams
Acting Vice Provost and Dean of Graduate Studies

Copyright © by

Lin Jin

2020

Table of Contents

List of Figures

List of Tables

Abstract

Fast Frequency Estimator

Based on Extended Kalman Filter

by

Lin Jin

Estimating the frequency and phase of a signal is a fundamental problem in signal processing and communication. Extended Kalman Filter (EKF) is one of the approaches, and most of the implementations are in digital technologies. The fast frequency estimator (FFE), as an application of extended Kalman Filter, is an analog circuit which can determine the amplitude, frequency and phase of a sine wave signal with noise. This work has built and analyzed the model of a continuous-time FFE. We approximately derive the FFE transfer function in steady state, which is a second-order type-2 feedback system. Compared with a second-order type-2 phase-locked loop (PLL), the bandwidth of the FFE is a variant during the acquisition. Thus, the architecture of FFE breaks the tradeoff between loop bandwidth and acquisition time with changeable loop dynamics, which is a main improvement over the PLL. The design and operation of the FFE are described in detail and verified by simulations using Cadence SpectreRF. The circuit of the FFE is divided into three main blocks: the main oscillator block performing the update of the state equations, and the K and P matrix blocks, which solve the Riccati equation of the analog FFE. A quadrature LC oscillator and a two-stage ring oscillator with injection signals are proposed to implement the main oscillator block and K matrix block, respectively. A simplified implementation of the P matrix block is proposed based on the study of the phase of all the signals. The FFE could be used instead of the PLL in the application

of Clock Recovery. Compared with the PLL, the FFE achieves much more rapid acquisition with changeable loop dynamics.

To my daughter

Evelyn

with love

Acknowledgments

I would like to thank my husband and my daughter who gave me support to complete my research work. I express my best thanks to my advisers, as I will not have the current achievement, on research and life, without the supervision and help from Prof. Ken Pedrotti and Prof. Don Wiberg. I would also thank other members of the reading committee, Prof. Steve Kang, and Prof. Ali Yanik, for their helpful suggestions on the thesis, and would thank Chengcheng Xu, for giving me enlightenment in the cooperative project. The students in our lab as well gave me a lot of help, and I would like to present my thanks to Dr. Mark McDonald, Dr. Tianchi Zeng, and Azzam Qureshi.

Chapter 1

Introduction

Estimating the frequency and phase of a signal is a fundamental problem in signal processing and communication. A variety of approaches have been developed. For instance, Fisher information is applied to estimating signal parameters in the presence of noise [1], and fast Fourier transform (FFT) based maximum likelihood estimation (MLE) has been proposed in [2] to derive practical algorithms on a finite number of discrete noisy observations. Furthermore, many well established methods to estimate instantaneous frequency (IF) were reviewed in [3], including differentiation of the phase and smoothing thereof, adaptive frequency estimation techniques, and extraction of the peak from time-varying spectral representations.

In this study, we focus on the use of the extended Kalman filter (EKF). In literature, the design and parameterization of EKF frequency estimation has been discussed in [4][5][6]. The majority of Kalman filter applications are implemented in digital computers. Also, most modern systems employ digital technologies to perform the functions once performed by analog circuits. However, analog circuits design helps to provide more fundamental knowledge for the digitalizing of analog functions. Moreover, the steady state of continuous-time estimators can be analyzed in frequency domain, which is an advantage over discrete-time

estimators [7]. In chapter 2, the model of fast frequency estimator (FFE) is derived in both discrete time and continuous time based on the extended Kalman filter. Implemented in Matlab, the choices of optimal noise covariances Q and R are studied for the discrete-time estimator. To implement the frequency estimator in continuous time, analog circuit design is considered and verified in simulation using the Cadence Spectre simulator. This is a novel approach, because all the previous Kalman filter research was done digitally. This is due to the difficulty in solving the associated Riccati equations.

The phase locked loop (PLL) has been studied for almost a century since the first description appeared in 1920's [8]. With the fast development of integrated circuits (IC), the PLL has been widely used since the 1970's [9]. There are advanced applications in communication, power and control systems in the past decades [10][11][12]. The tracking behavior has been studied according to the type of PLL [13]. The type-1 PLL can track the input frequency, but the phase error may not be zero. The type-2 PLL can track both the input frequency and phase. In 1955, Jaffe and Rechtin showed that a PLL is equivalent to a Wiener filter when the carrier frequency is known [14]. The Wiener filter is the steady state equivalent of the Kalman filter. In chapter 3, we approximately derive the FFE transfer function in steady state, which is a second-order type-2 feedback system. The bandwidth of the FFE is a variant during the acquisition. Thus, the architecture of FFE breaks the tradeoff between loop bandwidth and acquisition time with changeable loop dynamics. This is a main improvement over the PLL.

In chapter 4, two analog circuit structures are proposed to implement the FFE, based on G_mC and LC structures, separately. The circuit of the FFE is divided into three main blocks: the main oscillator block performing the update of the state equations, and the K and P matrix blocks, which solve the Riccati equation

of the analog FFE. Then, the basic issues in FFE circuit design are discussed. Namely, these are the requirements for the integrator corner frequency, loss and frequency detuning tolerance.

We begin in chapter 5 with the design and implementation of each of the 3 blocks in the FFE. We choose the LC oscillator as the main oscillator to achieve better phase noise performance. A coupled LC oscillator is designed to generate quadrature outputs, and its model is derived based on the concept of injection. There are several advantages for the K matrix block using a ring oscillator, rather than an LC oscillator. The ring oscillator is compact, has less coupling to and from other circuits, and has easy availability of multiple phases [15]. To avoid the feedback within the K and P matrix blocks, simplification in implementation is considered and verified by simulation. The performance of the FFE is simulated with GlobalFoundries $0.13\mu m$ 8HP process.

There are mainly four contributions in this work. First, we designed the continuous-time FFE, and its transfer function was derived in steady state. Second, we proposed two analog circuit structures to implement FFE, based on G_mC and LC, separately. We then proposed the quadrature LC oscillator and the two-stage ring oscillator to implement the main oscillator block and K matrix block, respectively. Finally, we studied the phase of all the signals and proposed a simplified implementation of the P matrix block, correspondingly.

Chapter 2

Kalman Filter

The Kalman filters have been widely used in control theory for applications, like navigation, trajectory optimization, etc [16][17]. We introduce, in this section, the basic theory of the Kalman filter and then discuss the fast frequency estimator based on the extended Kalman Bucy filter.

2.1 Kalman filter

The Kalman filter (KF) [18] is a recursive estimator, which compares its predictions with the incoming data and uses the difference to maintain a covariance matrix, which keeps track of how well the data is matching the model. If the model fits the data well, the covariance matrix tends to a matrix of zeros. The basic Kalman filter is in discrete-time form. The input of the system is denoted as $\overrightarrow{u(k)}$, a known time sequence. The state space variable $\overrightarrow{x(k)}$ at time k is derived from the state model at time $(k-1)$ as,

$$\overrightarrow{x}(k) = \overrightarrow{\Phi}(k-1)\overrightarrow{x}(k-1) + \overrightarrow{B}(k)\overrightarrow{u}(k) + \overrightarrow{w}(k), \tag{2.1}$$

where for the model of the input,

$\overrightarrow{\Phi}_k$ is the state transition model applied to the previous state $\overrightarrow{x}_{k-1}$;

$\overrightarrow{B}_k$ is the control-input model applied to the input vector $\overrightarrow{u}_k$;

$\overrightarrow{w}_k$ is the process noise assumed to follow a normal distribution N with mean 0 and covariance Q_k.

The observation $\overrightarrow{z(k)}$ at time k is from the model,

$$\overrightarrow{z}(k) = \overrightarrow{H}(k)\overrightarrow{x}(k) + \overrightarrow{v}(k), \tag{2.2}$$

where

$\overrightarrow{H}_k$ is the observation model which maps the real state space variable $\overrightarrow{x(k)}$ into the observed space;

$\overrightarrow{v}_k$ is the observation noise assumed to follow normal distribution N with mean 0 and covariance R_k.

The state estimate is denoted as $\overrightarrow{\hat{x}(k)}$ at each time step k. The Kalman filter makes two estimates of the state at each step: a prediction estimate, $\overrightarrow{\hat{x}}_-$, and an updated estimate, $\overrightarrow{\hat{x}}_+$. $\overrightarrow{\hat{x}}_+(k)$ is used to denote the estimate of $\overrightarrow{x}$ at time k given observations up to and including at time k. $\overrightarrow{\hat{x}}_-(k)$ is used to denote the estimate of $\overrightarrow{x}$ at time k given observations up to and including at time $(k-1)$.

$$\hat{x}_-(k) = E[x(k)|z(1), z(2), \cdots, z(k-1)], \tag{2.3}$$

$$\hat{x}_+(k) = E[x(k)|z(1), z(2), \cdots, z(k)]. \tag{2.4}$$

A covariance matrix is modified for both the prediction and update step. The notation $P(k)$ is used to denote the covariance of the estimation error, which is divided into the + and − steps as follows. $P_-(k)$ denotes the covariance of the estimation error of $\hat{x}_-(k)$, and $P_+(k)$ denotes the covariance of the estimation

error of $\hat{x}_+(k)$.

$$P_-(k) = E[(x(k) - \hat{x}_-(k)) - (x(k) - \hat{x}_-(k))^T], \tag{2.5}$$

$$P_+(k) = E[(x(k) - \hat{x}_+(k)) - (x(k) - \hat{x}_+(k))^T]. \tag{2.6}$$

These relationships are depicted in Figure 2.1.

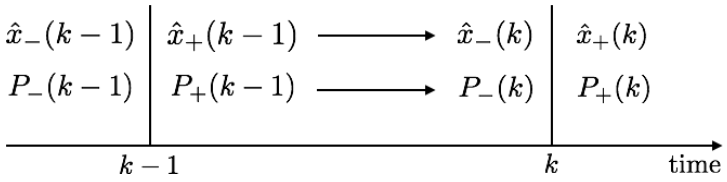

Figure 2.1: Timeline for a prediction and an updated estimates and estimation error covariances.

The process is carried out as follows:

Prediction Steps:

State Prediction Extrapolation

$$\overrightarrow{\hat{x}}_-(k) = \overrightarrow{\Phi}(k-1)\overrightarrow{\hat{x}}_+(k-1) + \overrightarrow{B}(k)\overrightarrow{u}(k), \tag{2.7}$$

Error Covariance Extrapolation

$$P_-(k) = \Phi(k-1)P_-(k-1)\Phi(k-1)^T + Q(k), \tag{2.8}$$

Eq. (2.8) is called the Riccati equation [19]. $P(k)$ is a positive symmetric matrix. $P(k) = P^T(k)$.

Update steps:

Kalman Gain Matrix

$$K(k) = P_-(k)H^T[H(k)P_-(k)H(k)^T + R(k)]^{-1}, \tag{2.9}$$

State Estimate Update

$$\overrightarrow{\hat{x}}_{+}(k) = \overrightarrow{\hat{x}}_{-}(k) + K(k)[\overrightarrow{z(k)} - H\overrightarrow{\hat{x}}_{-}(k)], \tag{2.10}$$

Error Covariance Update

$$P_{+}(k) = P_{-}(k)[I - K(k)H(k)]. \tag{2.11}$$

2.2 Extended Kalman filter

The Kalman filter provides the optimal solution to the tracking problem in the linear Gaussian environment [20]. The extended Kalman filter (EKF) is the nonlinear version of the Kalman filter [18]. In the extended Kalman filter, we linearize the nonlinear system around the Kalman filter estimate. The model is similar to the Kalman filter, and the difference is the state transition model f and observation model h, which do not need to be linear functions.

$$\overrightarrow{x}(k) = \overrightarrow{\phi}(\overrightarrow{x}(k-1), \overrightarrow{u}(k)) + \overrightarrow{w}(k), \tag{2.12}$$

$$\overrightarrow{z}(k) = \overrightarrow{h}(\overrightarrow{x}(k)) + \overrightarrow{v}(k). \tag{2.13}$$

Unlike the Kalman filter, functions ϕ and h cannot be applied to the covariance directly. Instead, the Jacobian matrix is computed at each step. As follows, the extended Kalman filter is derived by linearizing the signal model and using the KF equations to calculate the gain matrix.

Prediction steps:

System Linearization

$$\Phi(k) = \left.\frac{\partial \phi}{\partial x}\right|_{\hat{x}_+(k-1),u(k)}, \tag{2.14}$$

$$H(k) = \left.\frac{\partial h}{\partial x}\right|_{\hat{x}_-(k)}, \tag{2.15}$$

State Prediction Extrapolation

$$\overrightarrow{\hat{x}}_-(k) = \Phi(\overrightarrow{\hat{x}}_+(k-1), \overrightarrow{u}(k)), \tag{2.16}$$

Error Covariance Extrapolation

$$P_-(k) = \Phi(k-1)P_+(k-1)\Phi(k-1)^T + Q(k), \tag{2.17}$$

Update steps:

The gain matrix $K(k)$ is calculated based on the KF equations for the linearized system,

$$K(k) = P_-(k)H(k)^T[H(k)P_-(k)H(k)^T + R(k)]^{-1}, \tag{2.18}$$

The gain matrix, together with the nonlinear signal model, is used to generate the filtered state estimate at the next time instant.

State Estimate Update,

$$\overrightarrow{\hat{x}}_+(k) = \overrightarrow{\hat{x}}_-(k) + K(k)[z(k) - H\overrightarrow{\hat{x}}_-(k)], \tag{2.19}$$

Error Covariance Update

$$P_+(k) = P_-(k)[I - K(k)H(k)]. \tag{2.20}$$

2.3 Fast frequency estimator model

A discrete-time single tone signal can be expressed as $z(k) = a(\sin k\omega T_s + \phi) + v(k)$, where

$z(k)$ instantaneous signal;

a amplitude;

k sampling constant;

ω radian frequency;

T_s sampling time;

ϕ phase;

$v(k)$ observation noise, follows a normal distribution N with mean 0 and covariance $R(k)$.

The estimated signal $\hat{z}(k)$ can be written as $\hat{z}(k) = z(k) - v(k)$.
It is known that the consecutive samples of a sinusoid signal satisfy

$$\begin{aligned} \hat{z}(k+1) &= a\sin[(k+1)\omega T_s + \phi] && (2.21) \\ &= a\sin(k\omega T_s + \phi)\cos(\omega T_s) + a\cos(k\omega T_s + \phi)\sin(\omega T_s). && (2.22) \end{aligned}$$

To accurately estimate ω from the above model, the EKF can be applied. We denote the estimated signal x_1 and x_2 as in phase and quadrature with z, separately, and x_3 as the radian frequency of z. Assuming the frequency ω varies slowly enough, i.e. $x_3(k+1) = x_3(k) = \omega$ is assumed constant, the state space vector is given as

$$\overrightarrow{x}(k) = \begin{pmatrix} x_1 \\ x_2 \\ x_3 \end{pmatrix} = \begin{pmatrix} \sin(k\omega T_s + \phi) \\ \cos(k\omega T_s + \phi) \\ \omega \end{pmatrix} \qquad (2.23)$$

$$\overrightarrow{x}(k+1) = \begin{pmatrix} a\sin[(k+1)\omega T_s + \phi] \\ a\cos[(k+1)\omega T_s + \phi] \\ \omega \end{pmatrix} \tag{2.24}$$

$$= \begin{pmatrix} a\sin(k\omega T_s + \phi)\cos(\omega T_s) + a\cos(k\omega T_s + \phi)\sin(\omega T_s) \\ a\cos(k\omega T_s + \phi)\cos(\omega T_s) - a\sin(k\omega T_s + \phi)\sin(\omega T_s) \\ \omega \end{pmatrix} \tag{2.25}$$

$$= \begin{pmatrix} x_1(k)\cos(x_3(k)T_s) + x_2(k)\sin(x_3(k)T_s) \\ -x_1(k)\sin(x_3(k)T_s) + x_2(k)\cos(x_3(k)T_s) \\ x_3(k) \end{pmatrix} \tag{2.26}$$

$$= \begin{pmatrix} \cos(x_3(k)T_s) & \sin(x_3(k)T_s) & 0 \\ -\sin(x_3(k)T_s) & \cos(x_3(k)T_s) & 0 \\ 0 & 0 & 1 \end{pmatrix} \begin{pmatrix} x_1(k) \\ x_2(k) \\ x_3(k) \end{pmatrix} \tag{2.27}$$

Now the EKF may be able to estimate the constant $x_3(k) = \omega$. Then the measurement equation is

$$\hat{z}(k) = [1\ 0\ 0]\,\hat{x}(k) + v(k), \tag{2.28}$$

Thus, according to the EKF model, there is

$$\overrightarrow{x}(k+1) = \phi(\overrightarrow{x}(k)) + w(k), \tag{2.29}$$

$$\overrightarrow{z}(k) = h(\overrightarrow{x}(k)) + v(k), \tag{2.30}$$

where

$$\phi(k) = \begin{pmatrix} \cos(x_3(k)T_s) & \sin(x_3(k)T_s) & 0 \\ -\sin(x_3(k)T_s) & \cos(x_3(k)T_s) & 0 \\ 0 & 0 & 1 \end{pmatrix}, \tag{2.31}$$

$$h(k) = x_1(k). \tag{2.32}$$

$\overrightarrow{w}(k)$ is the process noise assumed to follow a normal distribution N with mean, 0 and covariance, $Q(k)$. As x_1 and x_2 are the noiseless transformations of the frequency x_3, the corresponding Q are all zeros except for $Q(3,3) = q$, where q is the variance of the frequency.

$\overrightarrow{v}(k)$ is the measurement noise assumed to follow normal distribution N with mean, 0 and covariance, $R(k)$.

Applying the EKF theory to the above model, a nonlinear recursive filter for estimating the frequency of a single sinusoid in white noise is obtained as follows,

$$\Phi(k) = \frac{\partial \phi}{\partial x} = \tag{2.33}$$

$$\begin{pmatrix} \cos(x_3(k)T_s) & \sin(x_3(k)T_s) & -T_s x_1(k)\sin(x_3(k)T_s) + T_s x_2(k)\cos(x_3(k)T_s) \\ -\sin(x_3(k)T_s) & \cos(x_3(k)T_s) & -T_s x_1(k)\cos(x_3(k)T_s) - T_s x_2(k)\sin(x_3(k)T_s) \\ 0 & 0 & 1 \end{pmatrix}, \tag{2.34}$$

$$H(k) = [1\ 0\ 0]\,, \tag{2.35}$$

$$\overrightarrow{\hat{x}}_-(k) = \overrightarrow{\Phi}(\overrightarrow{\hat{x}}_+(k-1), \overrightarrow{u}(k)), \tag{2.36}$$

$$P_-(k) = \Phi(k-1)P_+(k-1)F(k-1)^T + Q(k), \tag{2.37}$$

$$K(k) = P_-(k)H(k)^T[H(k)P_-(k)H(k)^T + R(k)]^{-1} \tag{2.38}$$

$$\overrightarrow{\hat{x}}_+(k) = \overrightarrow{\hat{x}}_-(k) + K(k)[z(k) - H\overrightarrow{\hat{x}}_-(k)], \tag{2.39}$$

$$P_+(k) = [I - K(k)H(k)]P_-(k). \tag{2.40}$$

2.3.1 Matlab implementation

This discrete-time FFE model is implemented in Matlab. In Figure 2.2, the measured signal z is a 1GHz sinusoidal signal embedded in Gaussian noise, and the estimated signals x_1 and x_2 are in phase and quadrature with z, respectively. Figure 2.3 shows the dynamic performance of the frequency estimate x_3, which starts from 0 and converges to a steady state value of 1GHz within 5 cycles. The error covariance matrix P is shown in Figure 2.42.5. P_{11}, P_{22} and P_{33} are shown in Figure 2.4, with initial value of 1 and steady state value close to 0. As P is a non-negative symmetric matrix, only P_{12}, P_{13} and P_{23} are shown in Figure 2.5, with steady state value of 0.

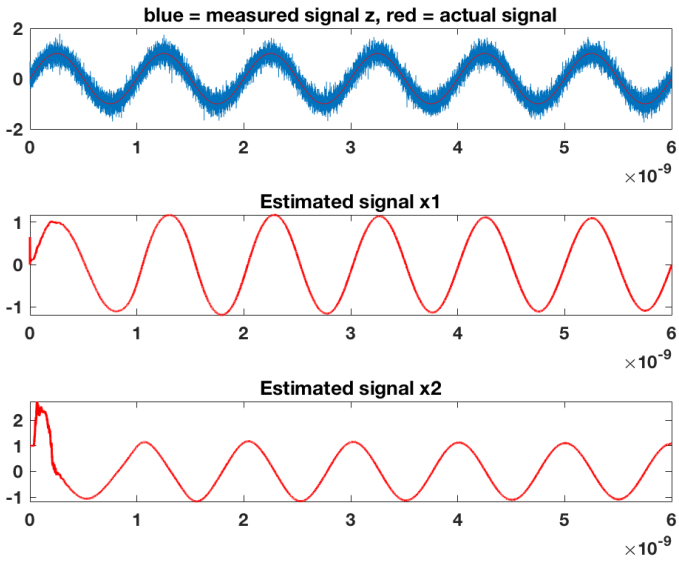

Figure 2.2: Measured and estimated signals in the discrete time FFE. The measured signal z is a 1GHz sinusoidal signal embedded in Gaussian noise, and the estimated signals x_1 and x_2 are in phase and quadrature with z, respectively.

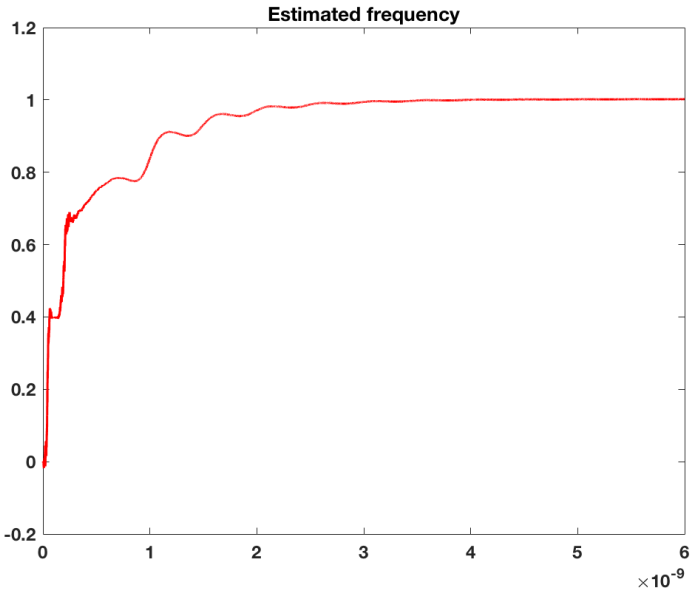

Figure 2.3: Estimated frequency in the discrete time FFE. The frequency estimate x_3 starts from 0 and converges to a steady state value of 1GHz within 5 cycles.

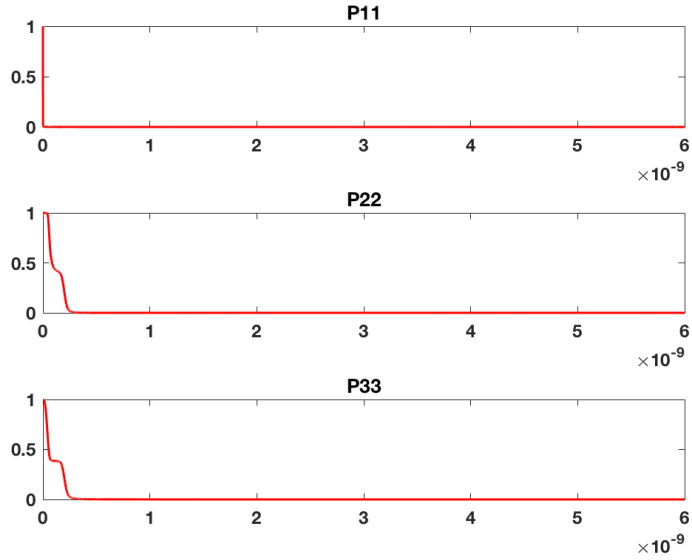

Figure 2.4: Portion performance of error covariance matrix P. P_{11}, P_{22} and P_{33} with initial value of 1 reach steady state value close to 0.

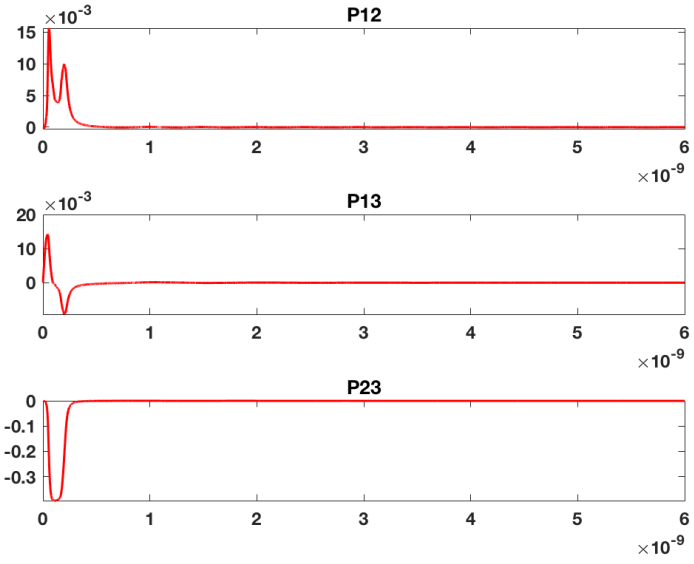

Figure 2.5: Portion performance of error covariance matrix P. P_{12}, P_{13} and P_{23} reach steady state value of 0.

2.3.2 Choices of Q and R

When the signal is buried in Gaussian noise, the random noise will lead to small differences in every simulation, which makes it difficult to compare the influences of different Q and R. Therefore, in this section, we assume the input is a pure sinusoidal signal of constant amplitude, frequency and phase.

The Riccati equation shows that the minimum value of the solution of the Riccati equation is given by Q, as

$$P_{-}(k) = \Phi(k-1)P_{+}(k-1)F(k-1)^{T} + Q(k). \tag{2.41}$$

Therefore, the value of the Kalman gain matrix K is related to the choice of Q. K defines the rate at which we change $\hat{x}$ based on the measurement. A smaller value of Q leads to more confidence in the estimated model, thus, the filter pays less attention to new data with smaller K. In Figure 2.6, different values of Q

lead to different damping factors.

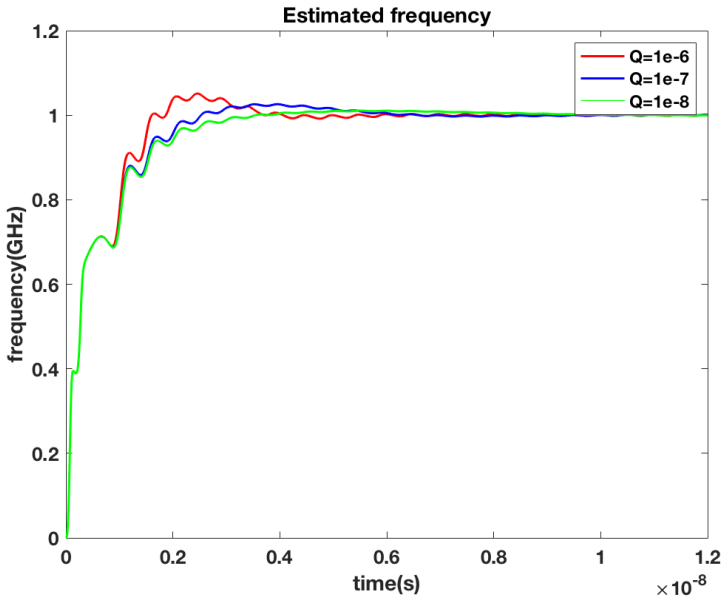

Figure 2.6: Dynamic comparison of different Q in discrete-time FFE. Different values of Q lead to different damping factors.

In the FFE, as x_1 and x_2 are noiseless transformations of frequency x_3, we only need to determine the estimation error covariance for x_3. When the signal frequency x_3 is constant or varies very slowly, the estimate model is reliable and very small Q is needed. However, during the acquisition, x_3 changes aggressively. Thus, if the chosen Q is too small, the filter may not be accurate enough. Figure 2.7 shows the steady state value of $Q = 1e - 8$ is less accurate than that of $Q = 1e-6$ and $Q = 1e-7$. As there is no measurement noise in this case, this conclusion works with different values of R. For the EKF, the solution of the Riccati equation is the first-order approximation to the true error covariance. Thus, the error covariance is underestimated according to the true error covariance. This condition needs to be taken into consideration as well.

The choice of R for the FFE is less important than that of Q, which means the accuracy of tracking is less sensitive to the value of R. The value of R influences

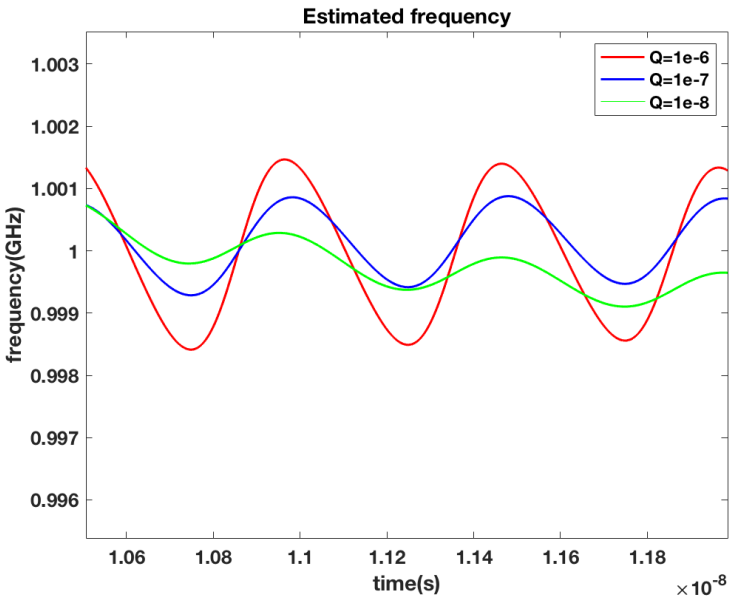

Figure 2.7: Steady state of different Q in discrete-time FFE. The steady state value of $Q = 1e - 8$ is less accurate than that of $Q = 1e - 6$ and $Q = 1e - 7$.

the acquisition time of the model. A smaller value of R means the measurement noise is smaller and thus, the measurement is more reliable. The influence of R is compared for pure sinusoidal input in Figure 2.82.9 for $Q = 0$ and $Q = 1e - 6$, separately. In both cases, the filter reaches the steady state faster with smaller R.

The steady state results in Figure 2.10 show that a proper value of Q leads to accurate steady state value for different values of R. Otherwise, as in Figure 2.11, there is a bias between the steady state value and expected value.

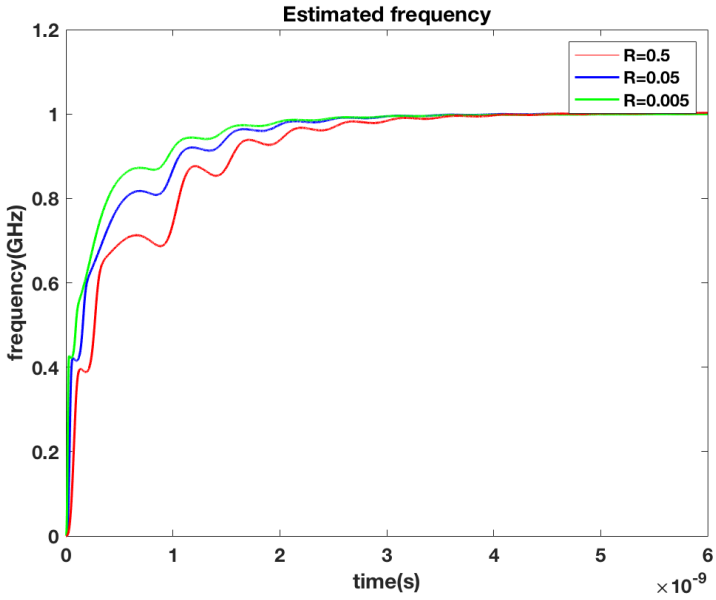

Figure 2.8: Dynamic comparison of different R when $Q = 0$. The filter reaches the steady state faster with smaller R

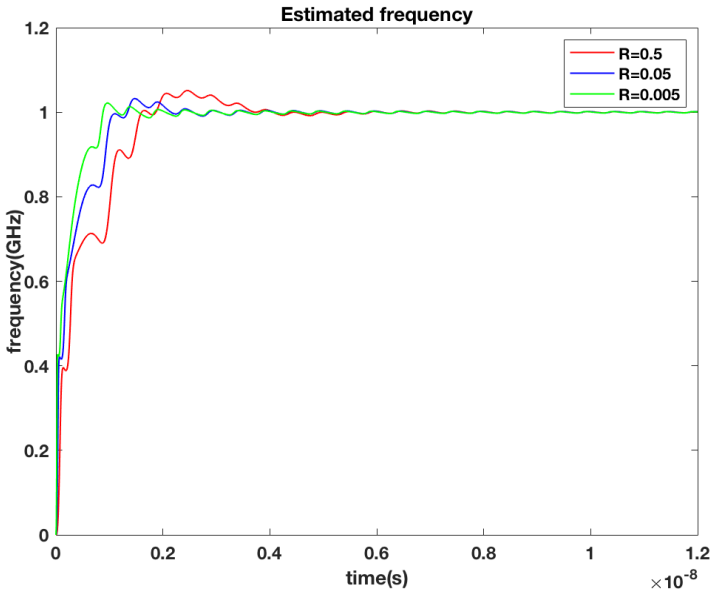

Figure 2.9: Dynamic comparison of different R when $Q = 1e-6$. The filter also reaches steady state faster with smaller R.

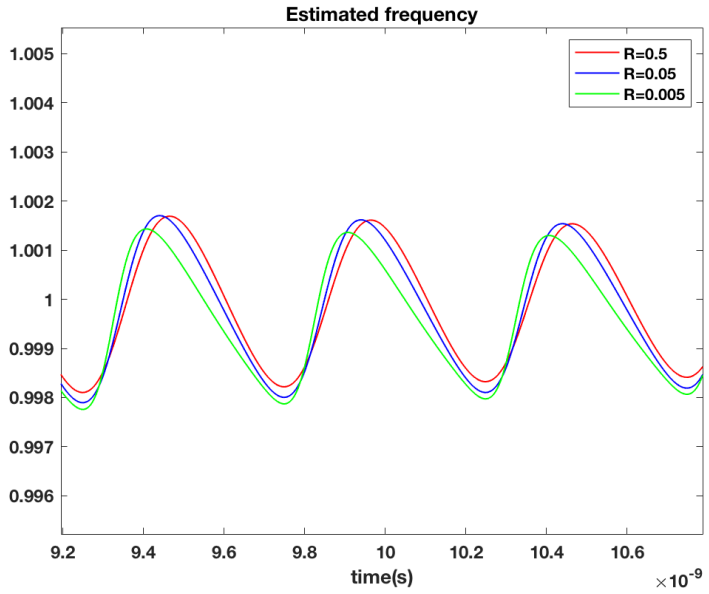

Figure 2.10: Steady state of different R when $Q = 1e - 6$. A proper value of Q leads to accurate steady state value for different values of R.

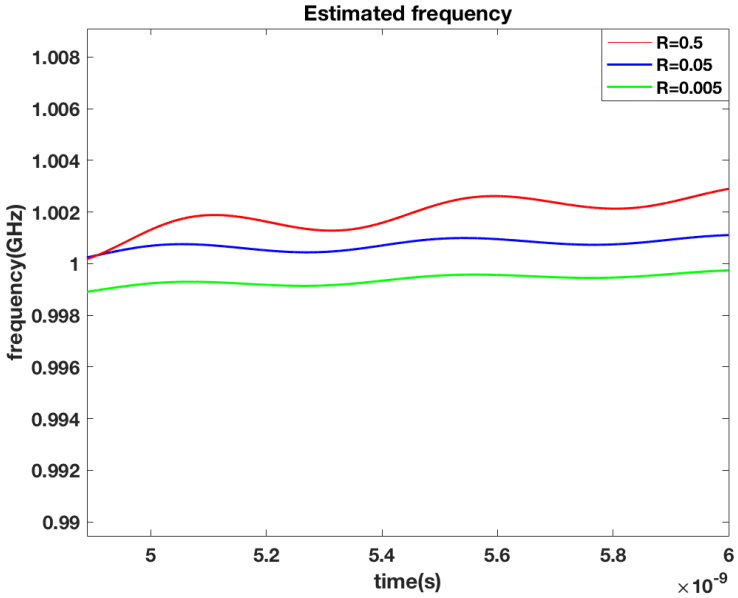

Figure 2.11: Steady state of different R when $Q = 0$. There is a bias between the steady state value and expected value.

2.4 Kalman-Bucy filter

The Kalman-Bucy filter is the continuous-time version of Kalman filter [21][22]. Assuming we have an input state space $\vec{x}$, and if it is an $n \times 1$ vector, the signal

can be represented in the form

$$\frac{d\overrightarrow{x}}{dt} = A\overrightarrow{x} + B\overrightarrow{u} + \overrightarrow{w}, \tag{2.42}$$

$$\overrightarrow{y} = C\overrightarrow{x} + \overrightarrow{v}, \tag{2.43}$$

where A is an $n \times n$ matrix, w is the process noise which follows a normal distribution $N(0, Q)$ and v is the measurement noise which follows a normal distribution $N(0, R)$.

Taking the limit as $T \to 0$ over the KF models, we can get the estimate of $\overrightarrow{x}$, denoted as $\overrightarrow{\hat{x}}$,

$$\frac{d\overrightarrow{\hat{x}}}{dt} = A\overrightarrow{\hat{x}} + B\overrightarrow{u} + K(t)(\overrightarrow{y} - C\overrightarrow{\hat{x}}), \tag{2.44}$$

and the best K is given by PC^TR^{-1} [23], where P is defined as,

$$\frac{dP}{dt} = AP + PA^T + Q - PC^TR^{-1}CP, \tag{2.45}$$

Eq. (2.44) is called analysis equation and Eq. (2.45) is called a differential Riccati equation [19]. $P(t)$ is the covariance of $(x(t) - \hat{x}(t))$, which is a positive symmetric $n \times n$ matrix. $P(t) = P^T(t)$.

2.5 Extended Kalman-Bucy filter

The Kalman-Bucy filter only deals with a linear system. To accommodate nonlinearity, the extended Kalman-Bucy filter is derived based on the nonlinear function $\overrightarrow{f}$. The modified model is,

$$\frac{d\overrightarrow{x}}{dt} = \overrightarrow{f}(\overrightarrow{x}) + B\overrightarrow{u} + \overrightarrow{w}, \tag{2.46}$$

$$\overrightarrow{y} = C\overrightarrow{x} + \overrightarrow{v}, \tag{2.47}$$

where

$$\overrightarrow{f}(\overrightarrow{x}) = \begin{pmatrix} f_1(\overrightarrow{x}) = f_1(x_1, \cdots, x_n) \\ \vdots \\ f_n(\overrightarrow{x}) \end{pmatrix}, \tag{2.48}$$

Then

$$A(t) = \left.\frac{\partial \overrightarrow{f}}{\partial \overrightarrow{x}}\right|_{\overrightarrow{x}=\overrightarrow{\hat{x}}(t)}, \tag{2.49}$$

Thus, the estimated model is

$$\frac{d\overrightarrow{\hat{x}}}{dt} = \overrightarrow{f(\hat{x})} + B\overrightarrow{u} + K(t)(\overrightarrow{y} - C\overrightarrow{\hat{x}}), \tag{2.50}$$

$$\frac{dP}{dt} = AP + PA^T + Q - PC^T R^{-1} CP, \tag{2.51}$$

where the best K is given by $PC^T R^{-1}$.

2.6 Fast frequency estimator model

Now let's consider a sinusoidal signal $x_1(t) = a\sin(\omega t + \phi)$ and its quadrature signal $x_2(t) = a\cos(\omega t + \phi)$, where a is the amplitude, ω is the radian frequency and ϕ is the phase. Thus there is $dx_1/dt = \omega x_2$ and $dx_2/dt = -\omega x_1$. Now let's define frequency $\omega = \omega_0 + kx_3$, where ω_0 is the initial fixed radian frequency, x_3 is a variable voltage and k is the frequency/voltage gain. Thus, there is $d\omega/dt = 0 = d\omega_0/dt + kdx_3/dt$, which leads to $dx_3/dt = 0$ when ω_0 is assumed to be constant. Hence, we can define

$$\overrightarrow{f}(x) = \frac{d}{dt}\begin{pmatrix} x_1 \\ x_2 \\ x_3 \end{pmatrix} = \begin{pmatrix} \omega x_2 \\ -\omega x_1 \\ 0 \end{pmatrix}, \tag{2.52}$$

$$B = 0, \tag{2.53}$$

$$C = [1\ 0\ 0], \tag{2.54}$$

$$\frac{d\overrightarrow{\hat{x}}}{dt} = \overrightarrow{f(\hat{x})} + B\overrightarrow{u} + K(t)(\overrightarrow{y} - C\overrightarrow{\hat{x}}), \tag{2.55}$$

The best K is PC^TR^{-1}, where P is defined as,

$$\frac{dP}{dt} = AP + PA^T + Q - PC^TR^{-1}CP, \tag{2.56}$$

As indicated in the Extended Kalman Filter,

$$A = \frac{\partial \overrightarrow{f}}{\partial \overrightarrow{x}} = \begin{pmatrix} 0 & \omega_0 + kx_3 & kx_2 \\ -(\omega_0 + kx_3) & 0 & -kx_1 \\ 0 & 0 & 0 \end{pmatrix}, \tag{2.57}$$

Thus, we derive

$$AP = \begin{pmatrix} (\omega_0 + k\hat{x}_3)P_{12} + k\hat{x}_2P_{13} & (\omega_0 + k\hat{x}_3)P_{22} + k\hat{x}_2P_{23} & (\omega_0 + k\hat{x}_3)P_{23} + k\hat{x}_2P_{33} \\ -(\omega_0 + k\hat{x}_3)P_{11} - k\hat{x}_1P_{13} & -(\omega_0 + k\hat{x}_3)P_{12} - k\hat{x}_1P_{23} & -(\omega_0 + k\hat{x}_3)P_{13} - k\hat{x}_1P_{33} \\ 0 & 0 & 0 \end{pmatrix}, \tag{2.58}$$

$$PA^T = \begin{pmatrix} (\omega_0 + k\hat{x}_3)P_{12} + k\hat{x}_2P_{13} & -(\omega_0 + k\hat{x}_3)P_{11} - k\hat{x}_1P_{13} & 0 \\ (\omega_0 + k\hat{x}_3)P_{22} + k\hat{x}_2P_{23} & -(\omega_0 + k\hat{x}_3)P_{12} - k\hat{x}_1P_{23} & 0 \\ (\omega_0 + k\hat{x}_3)P_{23} + k\hat{x}_2P_{33} & -(\omega_0 + k\hat{x}_3)P_{13} - k\hat{x}_1P_{33} & 0 \end{pmatrix}, \tag{2.59}$$

$$PC^T R^{-1} CP = \frac{1}{r}\begin{pmatrix} P_{11}^2 & P_{11}P_{12} & P_{11}P_{13} \\ P_{11}P_{12} & P_{12}^2 & P_{12}P_{13} \\ P_{11}P_{13} & P_{12}P_{13} & P_{13}^2 \end{pmatrix}. \tag{2.60}$$

Therefore, we can summarize 9 equations for the FFE,

$$\begin{aligned}
\frac{d\hat{x}_1}{dt} &= (\omega_0 + k\hat{x}_3)\hat{x}_2 + \frac{P_{11}}{r}(y - \hat{x}_1), && (2.61)\\
\frac{d\hat{x}_2}{dt} &= -(\omega_0 + k\hat{x}_3)\hat{x}_1 + \frac{P_{12}}{r}(y - \hat{x}_1), && (2.62)\\
\frac{d\hat{x}_3}{dt} &= \frac{P_{13}}{r}(y - \hat{x}_1), && (2.63)\\
\frac{dP_{13}}{dt} &= (\omega_0 + k\hat{x}_3)P_{23} + k\hat{x}_2 P_{33} - \frac{P_{11}P_{13}}{r}, && (2.64)\\
\frac{dP_{23}}{dt} &= -(\omega_0 + k\hat{x}_3)P_{13} - k\hat{x}_1 P_{33} - \frac{P_{12}P_{13}}{r}, && (2.65)\\
\frac{dP_{33}}{dt} &= -\frac{P_{13}^2}{r}, && (2.66)\\
\frac{dP_{11}}{dt} &= 2(\omega_0 + k\hat{x}_3)P_{12} + 2k\hat{x}_2 P_{13} - \frac{P_{11}^2}{r}, && (2.67)\\
\frac{dP_{12}}{dt} &= -(\omega_0 + k\hat{x}_3)(P_{11} - P_{22}) + k(\hat{x}_2 P_{23} - \hat{x}_1 P_{13}) - \frac{P_{11}P_{12}}{r}, && (2.68)\\
\frac{dP_{22}}{dt} &= -2(\omega_0 + k\hat{x}_3)P_{12} - 2k\hat{x}_1 P_{23} - \frac{P_{12}^2}{r}. && (2.69)
\end{aligned}$$

2.7 Summary

In this chapter, both linear and nonlinear Kalman filters are introduced in discrete time and continuous time. The discrete-time FFE is designed and verified in Matlab. Furthermore, the choices of optimal noise covariances Q and R are discussed and compared in simulation. Finally, based on extended Kalman-Bucy filter, the model of the continuous-time FFE is designed and 9 equations are derived.

Chapter 3

Phase-Locked Loop

The phase-locked loop (PLL) is a feedback control system whose output phase is related with the input phase [12]. In this chapter, we discuss different types of analog PLL. Then, the steady-state transfer function of FFE is derived and compared with that of the PLL.

3.1 Analog phase-locked loop

3.1.1 Simple PLL

Figure 3.1 is the block diagram of a simple PLL, which includes phase detector (PD), loop filter and voltage controlled oscillator (VCO) [24]. The PD compares the phase difference of the reference signal and VCO output, and then generates an output voltage. The relationship between the output voltage and input phase difference is defined as the gain of the PD and denoted by $K_{PD}(V/rad)$. In practice, the PD gain is nonlinear and non-monotonic. The loop filter, usually a low-pass filter, is used to suppress the large sidebands. The simplest loop filter is an R and C low-pass filter. The VCO is an oscillator whose frequency is decided

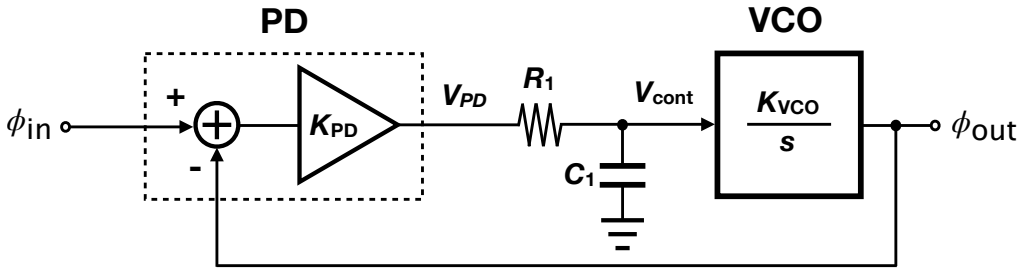

Figure 3.1: Simple PLL block diagram.

by the loop filter output voltage. The loop filter output voltage is also called the control voltage of the VCO. The ratio of the frequency and the control voltage is defined as the gain of the VCO and denoted by $K_{VCO}(rad/s/V)$. The relationship is expressed as

$$\omega_{out} = \omega_0 + K_{VCO}V_{cont}, \tag{3.1}$$

where ω_{out} is the VCO frequency, V_{cont} is the control voltage from the loop filter, and ω_0 is the VCO free running frequency when the control voltage is 0.

To further model VCO, we can write the VCO output as

$$V_{out}(t) = V_0 \cos\left(\omega_0 t + K_{VCO}\int V_{cont}dt\right). \tag{3.2}$$

Thus, the VCO can be modeled as a block with the control voltage as input and excess phase as output

$$\phi_{out} = K_{VCO}\int V_{cont}dt. \tag{3.3}$$

Hence, in s-domain we have

$$\frac{\phi_{out}}{V_{cont}}(s) = \frac{K_{VCO}}{s}. \tag{3.4}$$

The low-pass loop filter is expressed as

$$G_{LPF}(s) = \frac{1}{1 + s/\omega_{LPF}}, \tag{3.5}$$

where $\omega_{LPF} = 1/(R_1 C_1)$.

Thus, the open-loop transfer function is

$$G(s) = K_{PD} G_{LPF}(s) \frac{K_{VCO}}{s}. \tag{3.6}$$

Then, the closed-loop transfer function is

$$H(s) = \frac{\Phi_{out}}{\Phi_{in}}(s) = \frac{K_{PD} K_{VCO}}{R_1 C_1 s^2 + s + K_{PD} K_{VCO}}. \tag{3.7}$$

It is a second-order transfer function, which can be written as

$$H(s) = \frac{\omega_n^2}{s^2 + 2\zeta\omega_n s + \omega_n^2}, \tag{3.8}$$

where

$$\zeta = \frac{1}{2}\sqrt{\frac{\omega_{LPF}}{K_{PD} K_{VCO}}} \tag{3.9}$$

$$\omega_n = \sqrt{K_{PD} K_{VCO} \omega_{LPF}}. \tag{3.10}$$

The corresponding error response of the closed-loop PLL is

$$E(s) = 1 - H(s) = \frac{s^2 + 2\zeta\omega_n s}{s^2 + 2\zeta\omega_n s + \omega_n^2}. \tag{3.11}$$

As there is one pole at the origin in the open-loop transfer function, this PLL is also called a type-1 PLL. The amplitude responses of system and error transfer

function are shown in Figure 3.2 and 3.3 for different values of damping factor ζ. The system transfer function $H(s)$ performs as a low-pass filter, whereas the error transfer function $E(s)$ performs as a high-pass filter. Figure 3.2 shows that natural frequency ω_n is a good indication of bandwidth of the second-order type-1 PLL. The bandwidth means PLL can track a time varying input phase modulation within the loop bandwidth. The error response shows that input phase modulation outside the bandwidth can cause total phase error and can't be tracked. The loop $3dB$ bandwidth can be calculated as

$$\omega_{3dB} = \omega_n \left(1 - 2\zeta^2 + \sqrt{(1-2\zeta^2)^2 + 1}\right)^{1/2}. \tag{3.12}$$

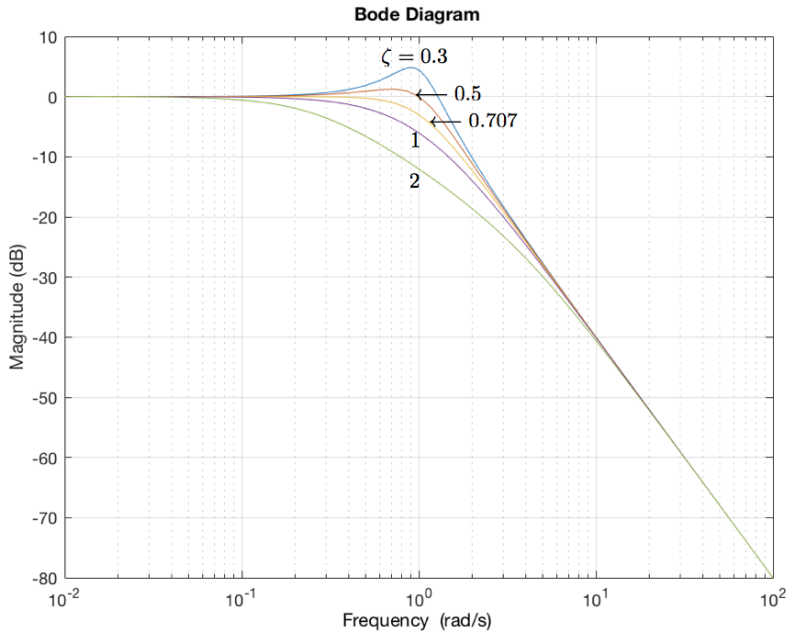

Figure 3.2: Second order type-1 PLL system amplitude response $|H(s)|$ for different values of damping factor ζ.

Natural frequency ω_n and ζ are two important parameters that describe the

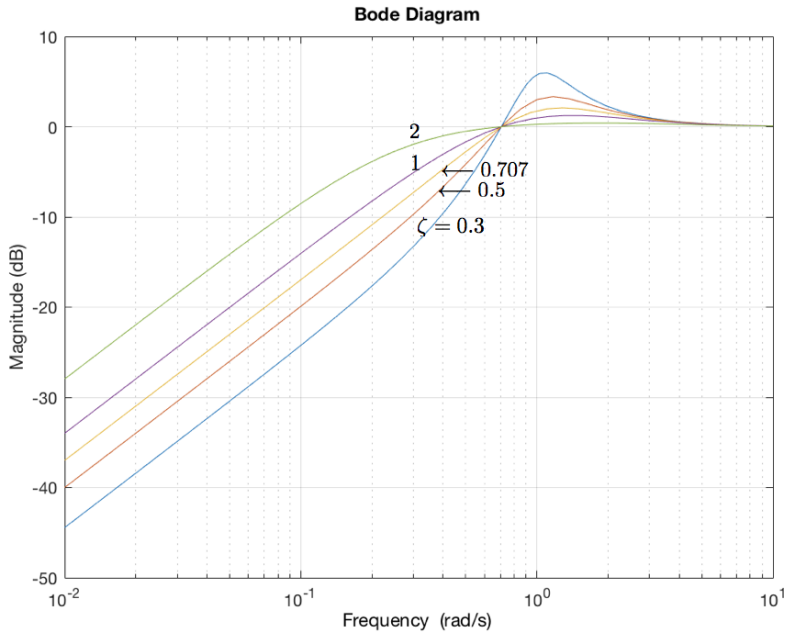

Figure 3.3: Second order type-1 PLL error amplitude response $|E(s)|$ for different values of damping factor ζ.

properties of second-order loops. The value of ζ is typically chosen as $\sqrt{2}/2$ [13]. When $\zeta < 1$, there is a complex conjugate pair of poles; when $\zeta = 1$, two poles are real and coincident; when $\zeta > 1$, there are two separate real poles. We can denote loop gain $K = K_{PD}K_{VCO}$, and there is

$$\omega_n = \sqrt{\omega_{LPF}K}, \tag{3.13}$$

$$\zeta = \frac{1}{2}\sqrt{\frac{\omega_{LPF}}{K}}. \tag{3.14}$$

There are several drawbacks of the simple PLL [25]. First, the loop stability ζ is tightly related by the corner frequency ω_{LPF} of the loop filter. A small value of ω_{LPF} is needed to suppress the ripple on the VCO control voltage, while it may lead to a less stable loop. Second, for an input frequency step change, there is finite static phase error, which is undesirable. We can derive the phase error in

this case from

$$\begin{aligned}\Phi(s) &= \Phi_{in}(s) - \Phi_{out}(s) && (3.15)\\ &= \Phi_{in}(s)\left[1 - \frac{\Phi_{out}}{\Phi_{in}}(s)\right] && (3.16)\\ &= \Phi_{in}(s)\left[1 - H(s)\right] && (3.17)\end{aligned}$$

For an input frequency step change of $\Delta\omega$, there is

$$\Phi_{in}(s) = \frac{\Delta\omega}{s^2}, \tag{3.18}$$

Hence, the steady-state phase error is

$$\begin{aligned}\Phi_{ss}(s) &= \lim_{s\to 0} s\Phi_{in}(s)\left[1 - H(s)\right] && (3.19)\\ &= \lim_{s\to 0} s\frac{\Delta\omega}{s^2}\left(1 - \frac{K_{PD}K_{VCO}}{R_1C_1s^2 + s + K_{PD}K_{VCO}}\right) && (3.20)\\ &= \lim_{s\to 0} \frac{\Delta\omega(R_1C_1s + 1)}{R_1C_1s^2 + s + K_{PD}K_{VCO}} && (3.21)\\ &= \frac{\Delta\omega}{K_{PD}K_{VCO}}. && (3.22)\end{aligned}$$

Larger K_{PD} and K_{VCO} leads to smaller phase error. However, a smaller damping factor is not good for stability and settling time. The open-loop transfer function can be expressed in terms of ω_n and ζ,

$$G(s) = \frac{\omega_n^2}{s^2 + 2\zeta\omega_n s}. \tag{3.23}$$

A Bode plot of the open loop transfer function can be used to evaluate stability. The gain crossover frequency ω_{gc} is defined as $|G(j\omega_{gc})| = 0dB$. From the Bode plot in Figure 3.4, we can get the phase margin, which is defined as $Arg[G(j\omega_{gc})] + \pi$. The phase margin gets larger as ζ increases and approaches 90^o when $\zeta > 2$.

The least phase margin of 45^o can be met when $\zeta \geqslant 0.5$.

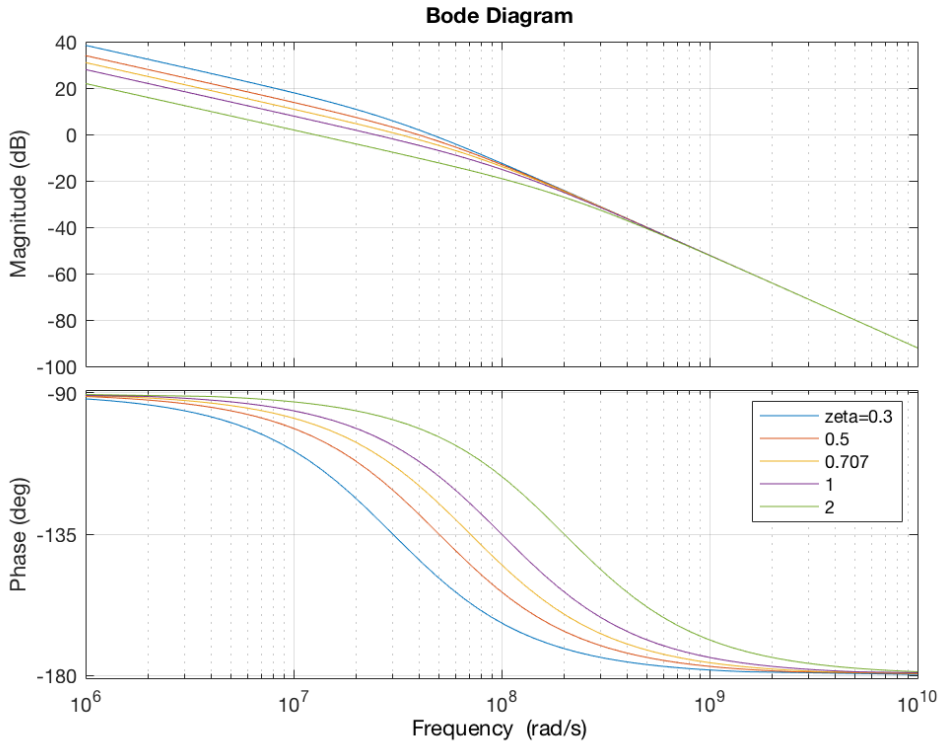

Figure 3.4: Type-1 PLL Bode plot. The phase margin gets larger as ζ increases and approaches 90^o when $\zeta > 2$.

3.1.2 Type-2 PLL

Figure 3.5 is the block diagram of a charge-pump PLL, which includes a phase frequency detector (PFD), a charge pump(CP), a loop filter and a voltage controlled oscillator (VCO) [26]. In the beginning, the PFD acts as a frequency detector. When the VCO frequency is close enough to the input frequency, the PFD operates as a phase detector to make the loop into phase lock. Determined by PFD output, the charge pump sources or sinks current into a capacitor. The PFD, CP and capacitor work together as an integrator of the input phase differ-

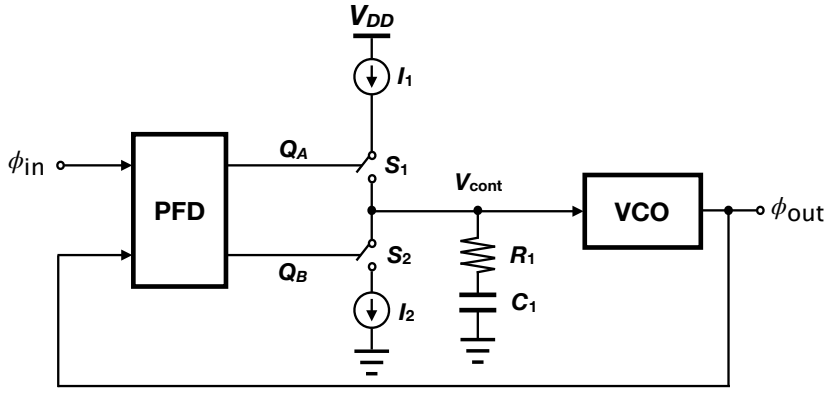

Figure 3.5: Type-2 PLL block diagram.

ence. As the model of the VCO is also an integrator, there are two integrators in a loop, which makes the loop unstable. Thus, a resistor in series with the capacitor acts as a loss to the integrator to make the system stable. A charge-pump PLL is also called type-2 PLL. The relationship between phase difference and the control voltage of the VCO is approximately

$$V_{cont} \simeq \frac{\phi_{in} - \phi_{out}}{2\pi} \left[\frac{I_{CP}}{C_1} tu(t) + I_{CP} R_1 u(t) \right], \tag{3.24}$$

Differentiating with respect to time, and taking a Laplace transform, we can get

$$\frac{V_{cont}}{\phi_{in} - \phi_{out}} = \frac{I_{CP}}{2\pi} \left(\frac{1}{C_1 s} + R_1 \right). \tag{3.25}$$

Then, the closed-loop transfer function of the PLL in Figure 3.5 is

$$H(s) = \frac{\frac{I_{CP} K_{VCO}}{2\pi C_1}(R_1 C_1 s + 1)}{s^2 + \frac{I_{CP}}{2\pi} K_{VCO} R_1 s + \frac{I_{CP}}{2\pi C_1} K_{VCO}}. \tag{3.26}$$

This is a second-order transfer function,

$$H(s) = \frac{2\zeta\omega_n s + \omega_n^2}{s^2 + 2\zeta\omega_n s + \omega_n^2}, \tag{3.27}$$

where

$$\zeta = \frac{R_1}{2}\sqrt{\frac{I_{CP}C_1K_{VCO}}{2\pi}}, \tag{3.28}$$

$$\omega_n = \sqrt{\frac{I_{CP}K_{VCO}}{2\pi C_1}}. \tag{3.29}$$

The corresponding error response is

$$E(s) = 1 - H(s) = \frac{s^2}{s^2 + 2\zeta\omega_n s + \omega_n^2}. \tag{3.30}$$

As opposed to a type-1 PLL, there is no need to trade off stability against ripple suppression. Increasing C_1 means a smaller cut-off frequency, which can lower the control voltage ripple. Correspondingly, larger ζ is achieved for better loop stability. The amplitude responses of the system and error transfer functions are shown in Figure 3.6 and 3.7 for different values of damping factor ζ. The system transfer function $H(s)$ performs as a low-pass filter, whereas the error transfer function $E(s)$ performs as a high-pass filter.

For a type-2 PLL, the bandwidth differs for different ζ. Thus, the natural frequency ω_n is no longer a good indication of bandwidth. However, ω_n is a good indication of the corner frequency of error high-pass filter. The loop $3dB$ bandwidth can be calculated as

$$\omega_{3dB} = \omega_n\left(1 + 2\zeta^2 + \sqrt{(2\zeta^2+1)^2+1}\right)^{1/2}. \tag{3.31}$$

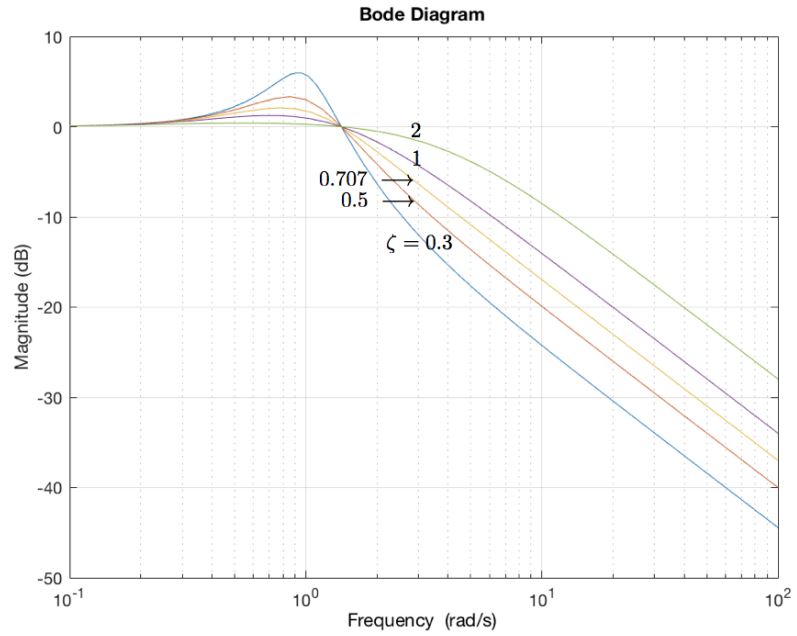

Figure 3.6: Second order type-2 PLL system amplitude response $|H(s)|$.

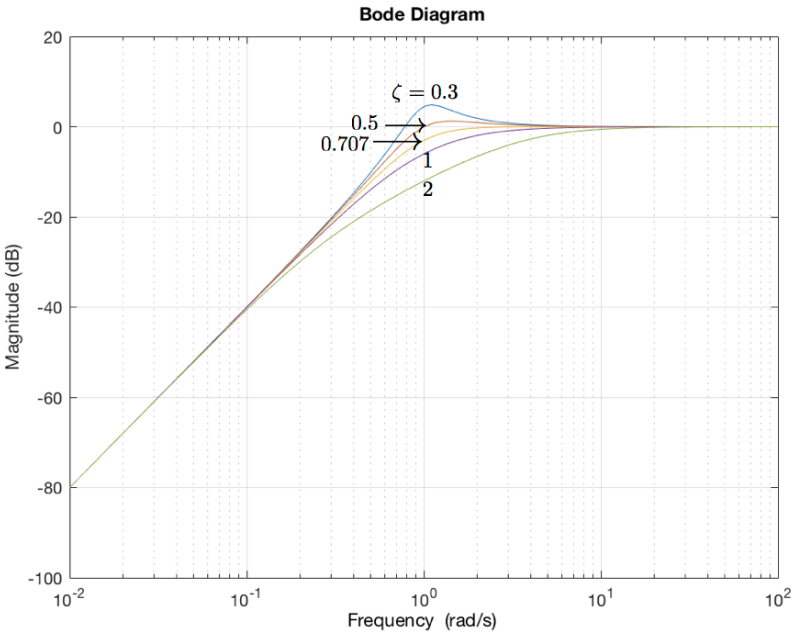

Figure 3.7: Second order type-2 PLL error amplitude response $|E(s)|$.

In PLL design, bandwidth is usually set as one-tenth of the input frequency to suppress the out-of-band phase noise. Figure 3.8 shows the step response of a second-order type-2 PLL. The settling time depends on the natural frequency and damping factor,

$$T_s = -\frac{\ln(tolerance\ fraction \times \sqrt{1-\zeta^2})}{\zeta\omega_n} \tag{3.32}$$

When input frequency is $1GHz$, if we choose $\omega_n = 2MHz$ and $\zeta = 0.707$, then the time taken to settle within 1 percentage is

$$T_s = -\frac{\ln(0.01 \times \sqrt{1-0.707^2})}{0.707 \times 2 \times 10^6} \tag{3.33}$$

$$= 3.5\mu s. \tag{3.34}$$

In this case, the settling time is about 3500 signal cycles.

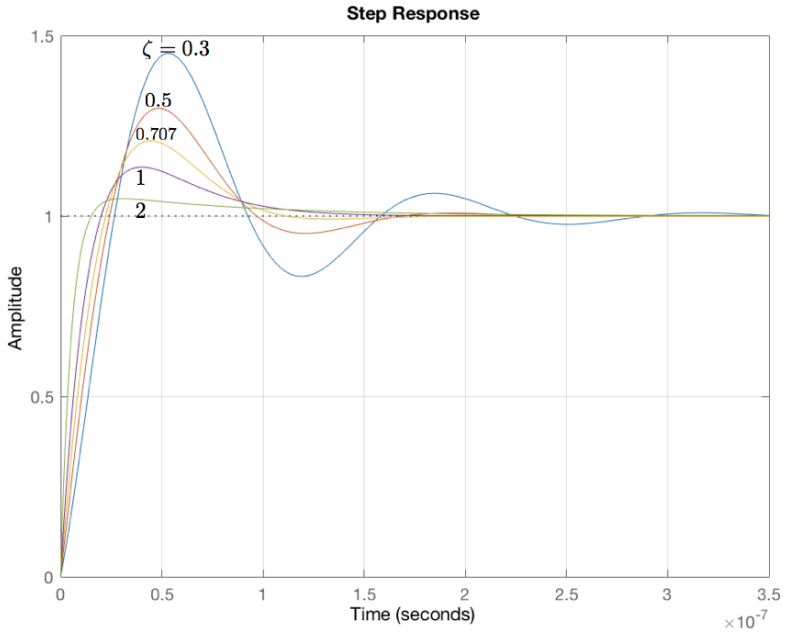

Figure 3.8: Step response for a second order type-2 PLL.

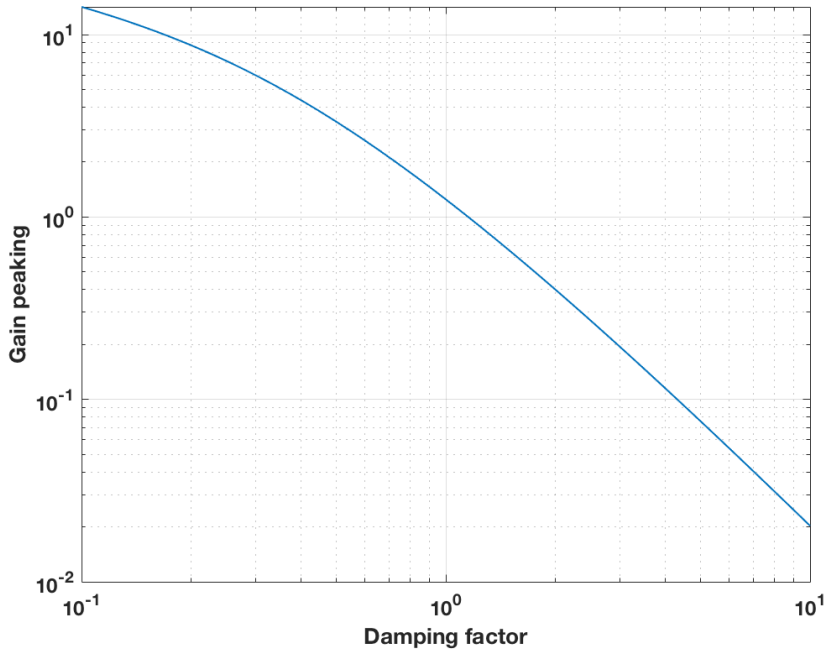

Figure 3.9: Gain peaking in $|H(s)|$ for a second order type-2 PLL.

As in Figure 3.2, gain peaking exists when ζ is smaller than 0.707 for second order type-1 PLL. In Figure 3.6, larger gain peaking is observed in type-2 PLL. The gain peaking of a second-order type-2 PLL can be expressed as

$$gainpeaking = 10log\frac{8\zeta^4}{8\zeta^4 - 4\zeta^2 - 1 + \sqrt{8\zeta^2 + 1}}. \tag{3.35}$$

Figure 3.9 shows that small damping leads to large peaking, and peaking still exists with large damping and never disappears.

The open loop transfer function can be expressed in terms of ω_n and ζ,

$$G(s) = \frac{2\zeta\omega_n s + \omega_n^2}{s^2}. \tag{3.36}$$

Figure 3.10 shows the open-loop Bode plot of a type-2 PLL. The phase margin performance is the same as type-1 PLL, which is listed in Table 3.1.

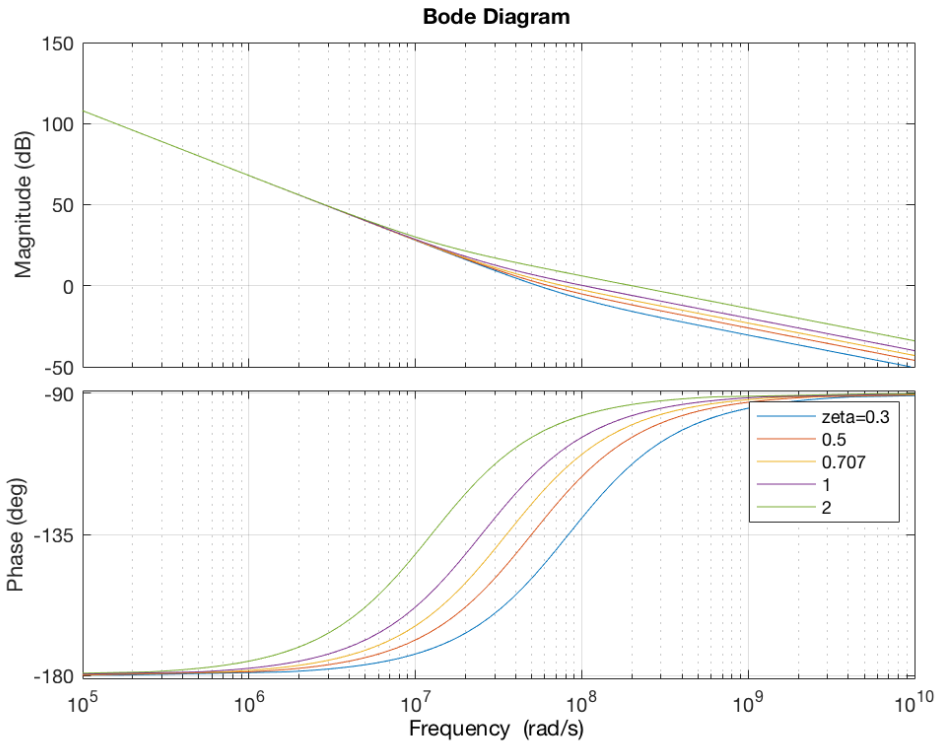

Figure 3.10: Type-2 PLL bode plot.

Table 3.1: Phase margin of second order PLL.

Damping factor	Phase margin(^{o})
0.3	33.3
0.5	51.8
0.707	65.6
1	76.4
2	86.4

3.2 FFE phase transfer function

In chapter 2, we have derived the model for FFE. From the observation on steady-state P signals, we can get the phase relation among them. For $x_1 = \sin(\omega t)$ and $x_2 = \cos(\omega t)$, there are $P_{13} = \cos(\omega t)$, $P_{23} = -\sin(\omega t)$, $P_{11} = P_{33} = 1 + \cos(2\omega t)$, $P_{22} = 1 - \cos(2\omega t)$, and $P_{12} = -\sin(2\omega t)$. These phase relations can

be also derived from FFE equations. From Eq. (2.61) we can derive the phase of $P_{11}x_1$, which should follow the phase of x_2. Then, there is

$$\phi_{p11} - \phi_{x1} = \phi_{x2}, \tag{3.37}$$

$$\phi_{p11} = \phi_{x1} + \phi_{x2}. \tag{3.38}$$

Similarly, Eq. (2.62) shows

$$\phi_{p12} - \phi_{x1} = \phi_{x1} + \pi, \tag{3.39}$$

$$\phi_{p12} = 2\phi_{x1} + \pi. \tag{3.40}$$

From Eq. (2.64), there is

$$\phi_{p11} - \phi_{p13} = \phi_{p23} + \pi, \tag{3.41}$$

$$\phi_{p11} = \phi_{p13} + \phi_{p23} + \pi. \tag{3.42}$$

Therefore,

$$\phi_{p13} = \phi_{x1} + \frac{\pi}{2}, \tag{3.43}$$

$$\phi_{p23} = \phi_{x2} + \frac{\pi}{2}. \tag{3.44}$$

Assuming the initial phase of x_1 is ϕ_0, we can derive the steady-state phases for all the signals in Table 3.2.

Table 3.2: Phases of FFE signals in steady state.

Signal	x_1	x_2	P_{13}	P_{23}	P_{11}	P_{12}
Phase	0	$\pi/2$	$\pi/2$	π	$\pi/2$	π

To derive the phase transfer function as for the PLL, we start with the first

and third equations for x_1 and x_3. In steady state, we assume the input signal $y = a\sin(\omega t + \phi_{in})$ and output signal $x_1 = a\sin(\omega t + \phi_{out})$, where ϕ_{in} and ϕ_{out} are very small phase excesses, and $\phi_{in} \neq \phi_{out}$. Also, we can approximately define $P_{11} = a_{11}(1 + \cos 2\omega t)$ and $P_{13} = a_{13}\cos\omega t$. Thus, when ϕ_{in} and ϕ_{out} are small, we can make an approximation that,

$$\begin{aligned} y - x_1 &= a\sin(\omega t + \phi_{in}) - a\sin(\omega t + \phi_{out}) && (3.45)\\ &= a\sin\omega t\cos\phi_{in} + a\cos\omega t\sin\phi_{in} - a\sin\omega t\cos\phi_{out} - a\cos\omega t\sin\phi_{out} && (3.46)\\ &\simeq a\cos\omega t(\phi_{in} - \phi_{out}). && (3.47) \end{aligned}$$

From Eq. (2.63), we obtain

$$\begin{aligned} \frac{dx_3}{dt} &= \frac{P_{13}}{r}(y - x_1) && (3.48)\\ &= \frac{a_{13}a}{r}\cos\omega t\cos\omega t(\phi_{in} - \phi_{out}) && (3.49)\\ &= \frac{a_{13}a}{2r}(\cos 2\omega t + 1)(\phi_{in} - \phi_{out}), && (3.50) \end{aligned}$$

Ignoring the high-frequency term,

$$\frac{dx_3}{dt} = \frac{a_{13}a}{2r}(\phi_{in} - \phi_{out}), \tag{3.51}$$

Taking the Laplace transform, we have

$$\frac{x_3}{\phi_{in} - \phi_{out}} = \frac{K_{x3}}{s} \tag{3.52}$$

where

$$K_{x3} = \frac{a_{13}a}{2r} \tag{3.53}$$

Eq. (2.61) for x_1 can be viewed as an oscillator with injection. If the injection

signal is excluded, it follows the model of the VCO

$$\frac{\phi_{ex}}{x_3}(s) = \frac{K_{VCO}}{s}. \tag{3.54}$$

Therefore, the model for the equation x_3 is a negative feedback loop with the open-loop transfer function

$$G_3(s) = \frac{K_{x_3} K_{VCO}}{s^2} \tag{3.55}$$

The injection signal of Eq. (2.61) can be approximately as

$$\begin{aligned} P_{11}(y - x_1) &= a_{11}(1 + \cos 2\omega t) a \cos \omega t(\phi_{in} - \phi_{out}) && (3.56)\\ &= \frac{3a_{11}a}{2} \cos \omega t(\phi_{in} - \phi_{out}) - \frac{a_{11}a}{2} \cos 3\omega t(\phi_{in} - \phi_{out}) && (3.57)\\ &\simeq \frac{3a_{11}a}{2} \cos \omega t(\phi_{in} - \phi_{out}) && (3.58) \end{aligned}$$

To further analyze the equation for x_1, we use the complex polar form to denote $x_1 = -ja \exp(j\theta)$, $x_2 = a \exp(j\theta)$ and $P_{11}(y - x_1) = \frac{3a_{11}a}{2}(\phi_{in} - \phi_{out}) \exp(j\theta)$. Thus, there is

$$\frac{d}{dt}\left(-jae^{j\theta}\right) = \frac{3a_{11}a}{2r}(\phi_{in} - \phi_{out})e^{j\theta} + \omega a e^{j\theta} \tag{3.59}$$

Assuming the amplitude a changes slowly in steady state, that is, $da/dt \simeq 0$, then

$$\begin{aligned} \frac{d\theta}{dt} &= \frac{3a_{11}}{2r}(\phi_{in} - \phi_{out}) + \omega && (3.60)\\ \theta &= \omega t + \phi_{out} && (3.61)\\ \frac{d\phi_{out}}{dt} &= \frac{3a_{11}}{2r}(\phi_{in} - \phi_{out}) && (3.62) \end{aligned}$$

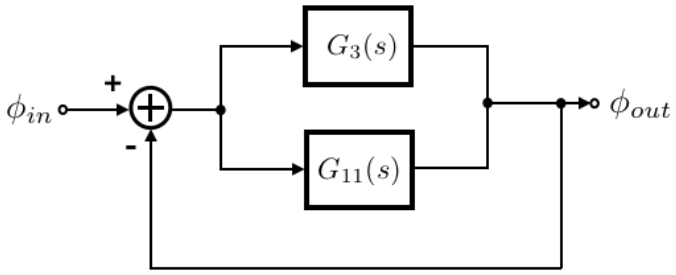

Figure 3.11: Model of FFE transfer function.

Taking the Laplace transform, we have

$$\phi_{out} = \frac{K_{11}}{s}(\phi_{in} - \phi_{out}) \tag{3.63}$$

where

$$K_{11} = \frac{3a_{11}}{2r} \tag{3.64}$$

Therefore, the model for the injection in equation x_1 is a negative feedback loop with the open-loop transfer function

$$G_{11}(s) = \frac{K_{11}}{s} \tag{3.65}$$

Now there are two paths for the excess phase ϕ_{ex}, one is through the control voltage x_3, and the other is through the injection current into the oscillator. Then, we can get the model for both paths in Figure 3.11. Thus, we can derive the closed-loop phase transfer function:

$$H(s) = \frac{G_3(s) + G_{11}(s)}{1 + G_3(s) + G_{11}(s)} \tag{3.66}$$

$$= \frac{sK_{11} + K_{x3}K_{VCO}}{s^2 + sK_{11} + K_{x3}K_{VCO}} \tag{3.67}$$

As a second-order transfer function, there is

$$\omega_n = \sqrt{K_{x3}K_{VCO}} \tag{3.68}$$

$$= \sqrt{\frac{a_{13}aK_{VCO}}{2r}}, \tag{3.69}$$

$$\zeta = \frac{K_{11}}{2\sqrt{K_{x3}K_{VCO}}} \tag{3.70}$$

$$= \frac{3a_{11}}{2\sqrt{2ra_{13}aK_{VCO}}}. \tag{3.71}$$

Charge-pump PLL uses a resistor in series with the capacitor in the loop filter to make the system stable. Several approaches were also studied to provide a zero in PLLs. A voltage-controlled delay line [27] and a discrete-time delay cell [28] are employed in the synthesizers. From the analysis on FFE transfer function, we can view the function of the injection signals as providing the zero to stabilize the system.

Besides those already known advantages of a second-order type-2 PLL, fast settling speed is one of the biggest advantages of the FFE. As we know, the settling time of a second-order system is inverse proportional to the bandwidth. Multi modes are employed in [29] to achieve Adaptive bandwidth. A fractional PLL is studied to achieve faster acquisition together with wide bandwidth in [30].

In the FFE, the natural frequency is not a constant, as it is decided by a_{13}, which is the time-varying amplitude of P_{13}. In the very beginning, the covariance P is large, thus, very fast acquisition is achieved. In general, the loop bandwidth is designed to not exceed 1/10 of the signal frequency. Assuming that we set the steady state bandwidth of both PLL and FFE to be 1/10 of the signal frequency, the bandwidth of FFE during the acquisition can be much larger to achieve fast acquisition. The acquisition is also called capture, and pull-in [31]. In steady state, all the P signals are close to 0 and a small value of P leads to a low natural

frequency to meet the bandwidth requirement.

The exact acquisition range is given by the solution of a second-order nonlinear differential equation. Thus, approximation is made in terms of loop gain [32]. Hence, the changeable loop dynamics leads to a large acquisition range. After acquisition, the output signal can still track the input frequency deviation within a certain range, which is called hold-in range. The hold-in range is always larger than the acquisition range with an incoming signal [33]. In real circuits, there are more restrictions, like the frequency range of the main oscillator and its ability of injection locking.

3.3 Summary

In this chapter, we first introduce type-1 and type-2 PLL and their transfer function. Also, the bode diagrams of PLL with different damping factors are simulated and compared. Finally, we approximately investigate the transfer function of FFE in steady state, which is a second-order type-2 system. The bandwidth of FFE is decided by the amplitude of P_{13}, which is a variable during acquisition. Hence, the architecture of FFE breaks the tradeoff between loop bandwidth and acquisition time with changeable loop dynamics.

Chapter 4

Circuit Implementation and Design Concerns

In this chapter, we investigate various ways to implement the FFE. First, the most straightforward approach is using G_mC structures. Second, a model based on LC structures is introduced and analyzed. Finally, we discuss several design concerns of the FFE we have discovered, namely: (1) requirement for integrator corner frequency; (2) main oscillator loss requirement; (3) frequency detuning tolerance; (4) K matrix block loss and frequency detuning tolerance; (5) K matrix block loss and phase delay tolerance.

4.1 G_mC implementation model

The structure of the FFE is diagrammatically depicted in Figure 4.1. From an external point of view, the FFE is a device with the measured signal y as input and a generating signal x_1 and the estimated control voltage x_3 as outputs. The internal structure consists of three main blocks: the main oscillator block performing the update of the state equations, with the K and P matrix blocks

providing the Riccati equation. The equations for the FFE are first-order differ-

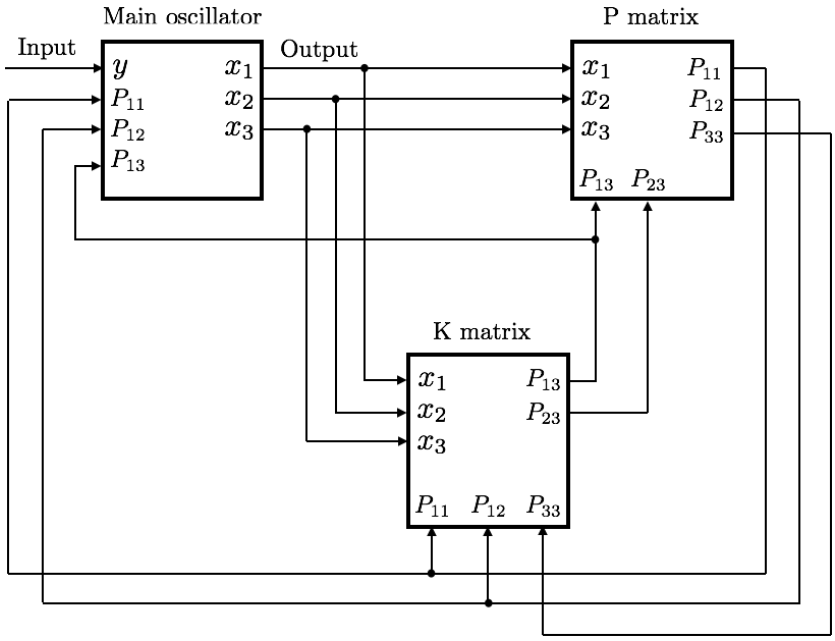

Figure 4.1: FFE diagram.

ential equations, and the most direct implementation is based on capacitors. The derivative form of the capacitor current-voltage relation is

$$\frac{dV(t)}{dt} = \frac{1}{C} I(t), \tag{4.1}$$

Using this, Eq. (2.61), (2.62) and (2.63) can be rewritten as

$$\frac{d\hat{x}_1}{dt} = \frac{G_m}{C}\hat{x}_2 + \frac{I_1}{C}, \tag{4.2}$$

$$\frac{d\hat{x}_2}{dt} = -\frac{G_m}{C}\hat{x}_1 + \frac{I_2}{C}, \tag{4.3}$$

$$\frac{d\hat{x}_3}{dt} = \frac{I_3}{C}, \tag{4.4}$$

where $G_m = \omega C$, $I_1 = P_{11}(y - \hat{x}_1)C/r$, $I_2 = P_{12}(y - \hat{x}_1)C/r$ and $I_3 = P_{13}(y - \hat{x}_1)C/r$.

Thus, we obtain the corresponding circuit model as Figure 4.2, which is called

the main oscillator block. It can be seen that $x_1 \& x_2$ comprise a 2-stage G_mC ring oscillator with natural frequency ω, and x_3 is generated by an integrator.

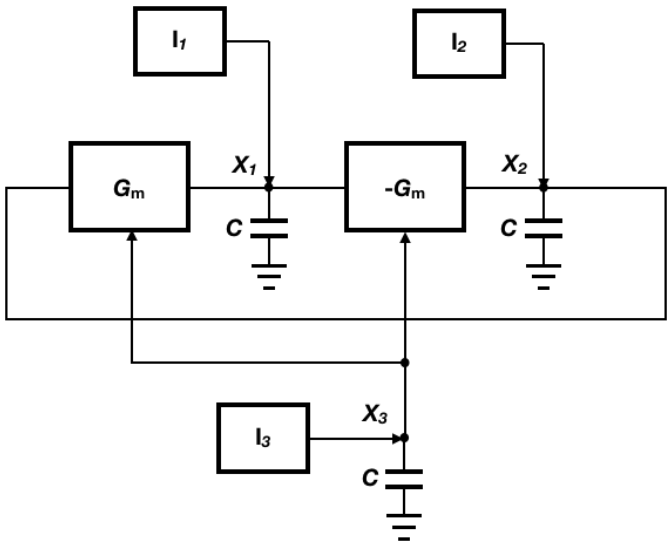

Figure 4.2: G_mC model for FFE main oscillator.

Similarly, Eq. (2.64), (2.65) and (2.66) can be rewritten as

$$\frac{dP_{13}}{dt} = \frac{G_m}{C}P_{23} + \frac{I_{13}}{C}, \tag{4.5}$$

$$\frac{dP_{23}}{dt} = -\frac{G_m}{C}P_{13} + \frac{I_{23}}{C}, \tag{4.6}$$

$$\frac{dP_{33}}{dt} = \frac{I_{33}}{C}, \tag{4.7}$$

where $G_m = \omega C$, $I_{13} = (k\hat{x}_2 P_{33}C - P_{11}P_{13}C)/r$, $I_{23} = (-k\hat{x}_1 P_{33}C - P_{12}P_{13}C)/r$ and $I_{33} = -P_{13}^2 C/r$.

The circuit model for P_{13} and P_{23} is called the K matrix block, and its block diagram is shown in Figure 4.3. $P_{13} \& P_{23}$ can be implemented as a 2-stage G_mC ring oscillator with natural frequency ω, and P_{33} is generated by an integrator.

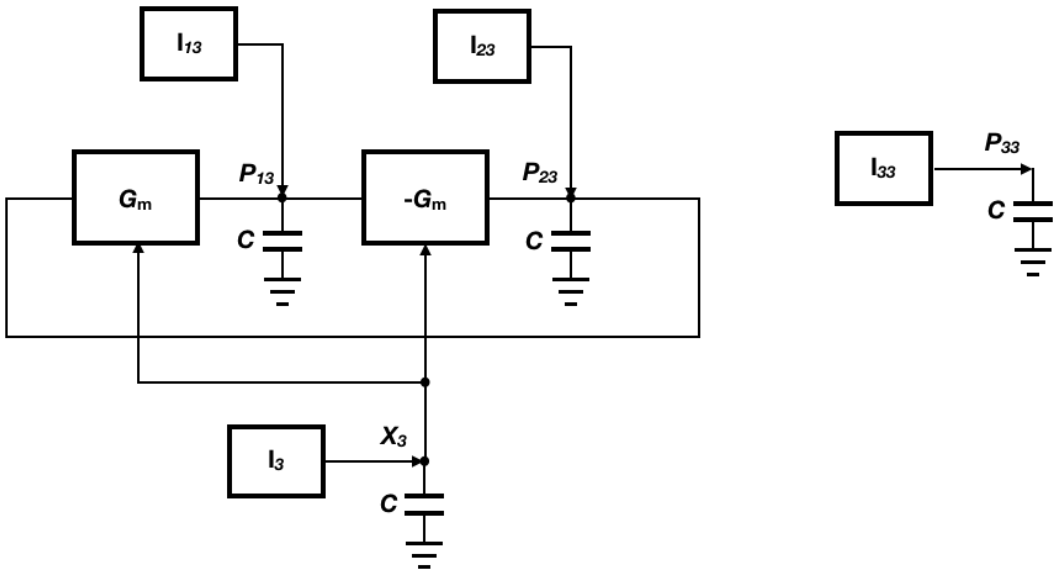

Figure 4.3: G_mC model for FFE K matrix, portion of the covariance matrix.

Eq. (2.67), (2.68) and (2.69) can be rewritten as

$$\frac{dP_{11}}{dt} = \frac{2G_m}{C}P_{12} + \frac{I_{11}}{C}, \tag{4.8}$$

$$2\frac{dP_{12}}{dt} = -\frac{2G_m}{C}(P_{11} - P_{22}) + \frac{I_{12}}{C}, \tag{4.9}$$

$$\frac{dP_{22}}{dt} = -\frac{2G_m}{C}P_{12} + \frac{I_{22}}{C}, \tag{4.10}$$

where $G_m = \omega C$, $2G_m = 2\omega C$,$I_{11} = (2k\hat{x}_2P_{13}C - P_{11}^2C)/r$, $I_{12} = [k(\hat{x}_2P_{23} - \hat{x}_1P_{13})C - P_{11}P_{12}C]/r$ and $I_{22} = (-2k\hat{x}_1P_{23}C - P_{12}^2C)/r$.

The circuit model for P_{11}, P_{12} and P_{22} is called the P matrix block and shown in Figure 4.4. $(P_{11} - P_{22})$ and $2P_{12}$ can also be generated by a 2-stage ring oscillator with natural frequency 2ω.

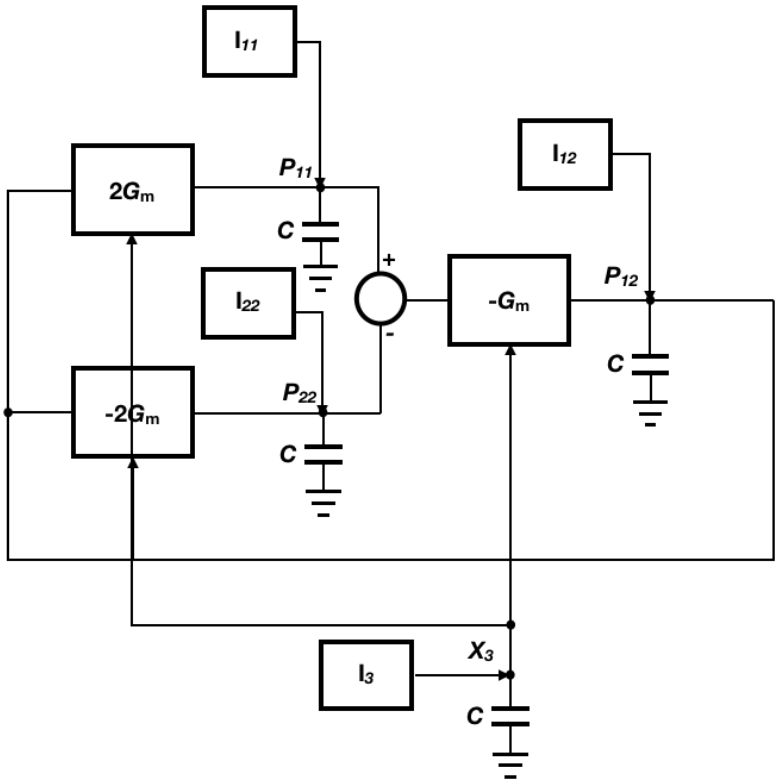

Figure 4.4: G_mC model for FFE P matrix, portion of the covariance matrix.

We set the initial frequency of the main oscillator $\omega_0 = G_m/C$ to $1GHz$ and tuning gain k to $400MHz/V$ for simulation. For the input signal $y = a\sin(\omega_{in}t)$, when $a = 1V$ and $\omega_{in} = 1GHz$, the G_mC model generates the signals x_1, x_2, x_3 and their covariance P signals as shown in Figure 4.5 - 4.8. These are generated by ideal behavioural models using Cadence SpectreRF.

In Figure 4.5 the estimated signals x_1 and x_2 are in phase and quadrature with input signal y, respectively. Figure 4.6 shows the dynamic performance of the frequency control voltage estimate x_3, which starts from 0V and quickly converges to the steady-state value of 0V corresponding to 1GHz.

As P is a non-negative symmetric matrix, only P_{12}, P_{13}, P_{23}, P_{11}, P_{22} and P_{33} are simulated. P_{13} and P_{23} shown in Figure 4.7 oscillate at the same frequency of the main oscillator, ω, and converge to the steady-state value of 0V. P_{33} shown

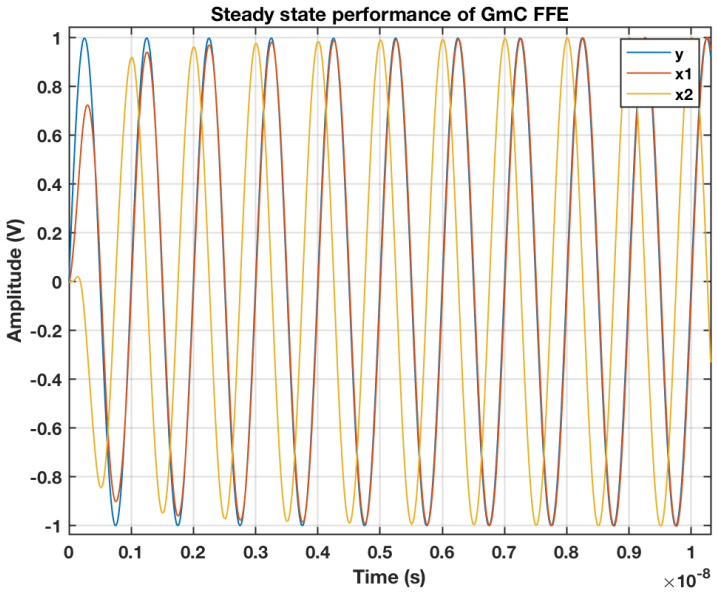

Figure 4.5: G_mC circuit performance showing the output x_1 and its quadrature x_2 following input y during acquisition.

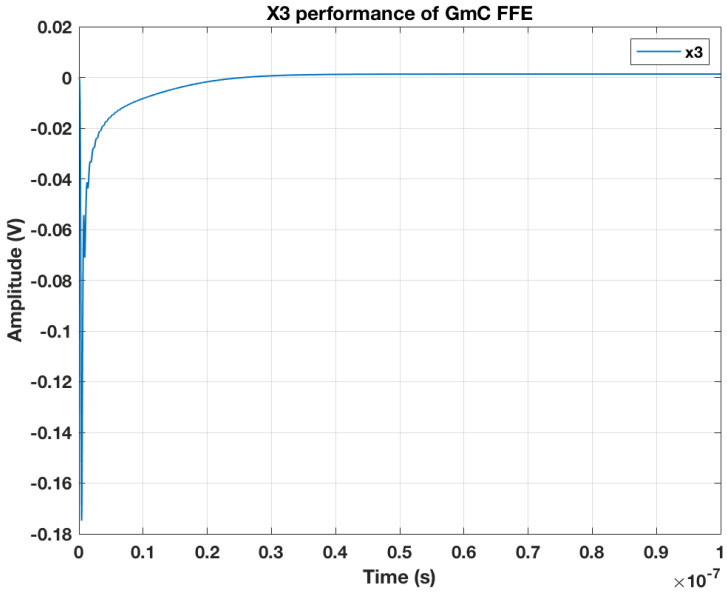

Figure 4.6: Frequency estimate x_3 performance of the G_mC circuit showing x_3 converging to its steady state value during acquisition. The acquisition time to 1 percentage of steady-state value is around 10ns, which equals to 10 cycles of the signal showing rapid acquisition.

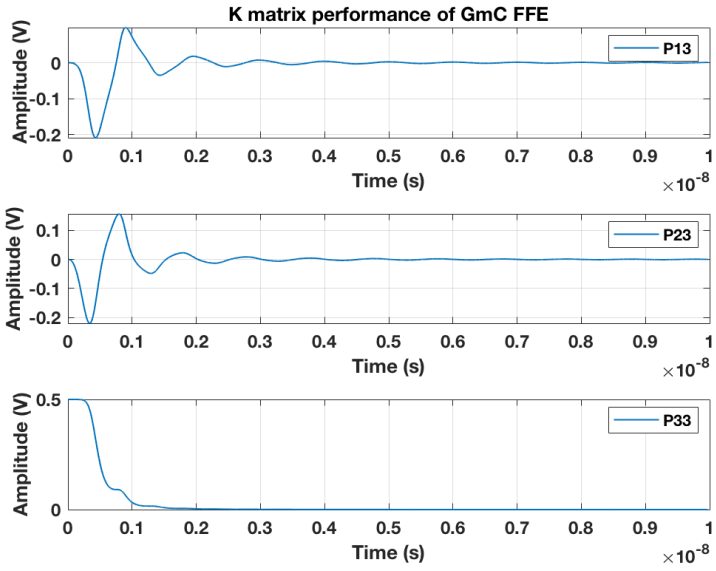

Figure 4.7: K matrix performance of G_mC circuit with P_{13} setting the gain which drives the output frequency estimate x_3 to match the input and going to zero when the output and input match.

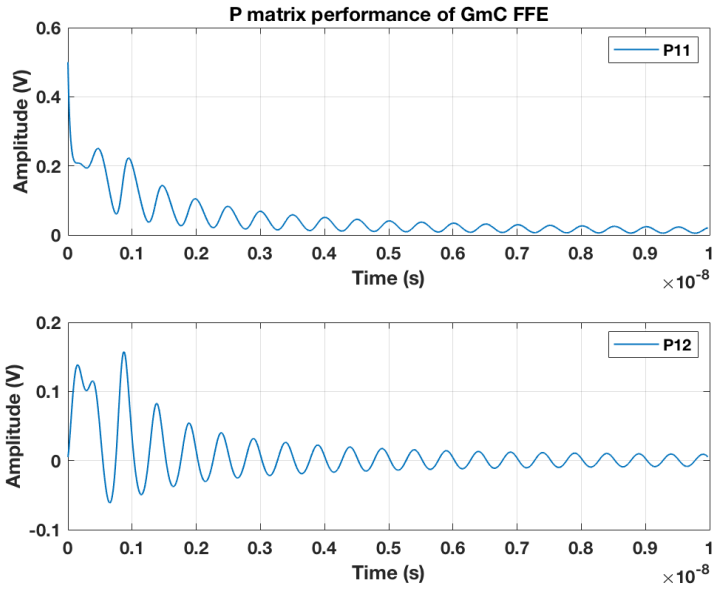

Figure 4.8: P matrix performance of G_mC circuit. These terms control the gain of the error signal $(y - x_1)$ used to match input and output, and will also approach zero for a lossless main oscillator and occur at twice its frequency.

in Figure 4.7 is the variance of x_3 with initial guess set to 0.5V, and converges to 0V when x_3 reaches the steady state. P_{11} and P_{12} shown in Figure 4.8 oscillate at twice the frequency of the main oscillator, 2ω, and converge to the steady-state value close to 0V.

Figure 4.9 and Figure 4.10 show the performance when the input frequency is $0.95GHz$ and $1.05GHz$, respectively. In both cases, the frequency estimate x_3 quickly converges to the corresponding steady-state value within 10 cycles. The working frequency range for the FFE, ideally, is determined by the initial values chosen for P_{11}, P_{22} and P_{33}. Large initial value leads to large acquisition range. In real circuits, there are more restrictions, like the tuning range of the main oscillator.

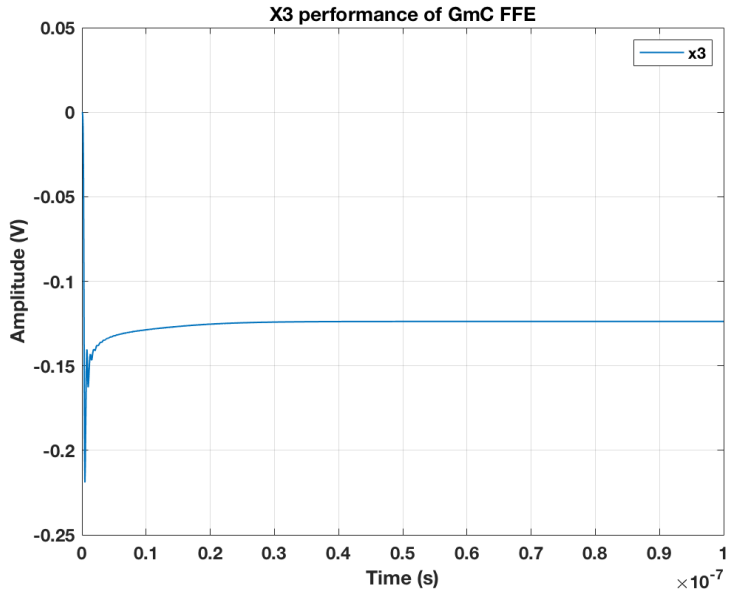

Figure 4.9: X_3 performance of G_mC circuit with 0.95GHz input. The frequency estimate x_3 reaches a steady state of -0.125V with 1GHz natural frequency within around 10 cycles.

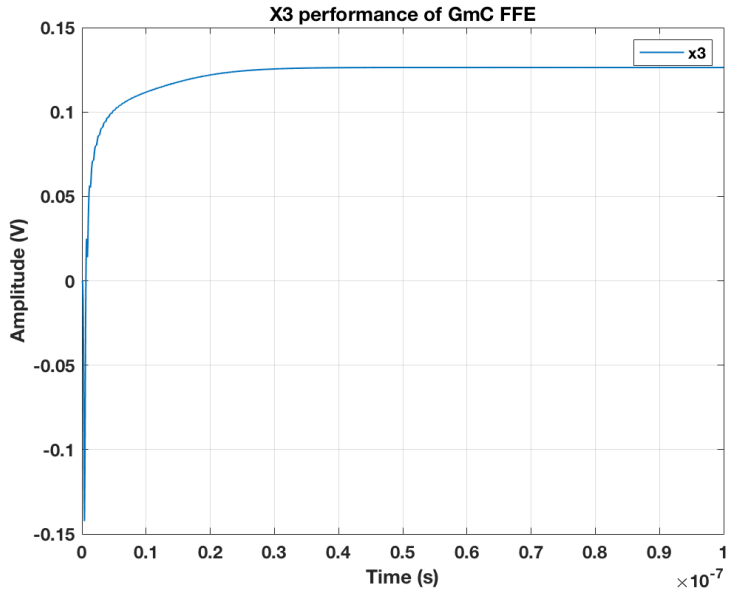

Figure 4.10: X_3 performance of G_mC circuit with 1.05GHz input. The frequency estimate x_3 reaches a steady state of 0.125V with 1GHz natural frequency within around 10 cycles.

4.2 LC implementation model

Besides G_mC oscillators, LC oscillators are often used due to the good phase noise performance. Thus, an alternate way to implement FFE is using inductors and capacitors. Similar to the capacitor, the derivative form of the inductor current-voltage relation is

$$\frac{dI(t)}{dt} = \frac{1}{L}V(t). \tag{4.11}$$

Thus, for the circuit in Figure 4.11, the FFE equations correspond to an inductor with series voltage injection and a capacitor with parallel current injection. The state-space circuit description of this oscillator is:

$$\frac{dV}{dt} = \frac{1}{C}(I + I_c), \tag{4.12}$$

$$\frac{dI}{dt} = -\frac{1}{L}(V - V_c), \tag{4.13}$$

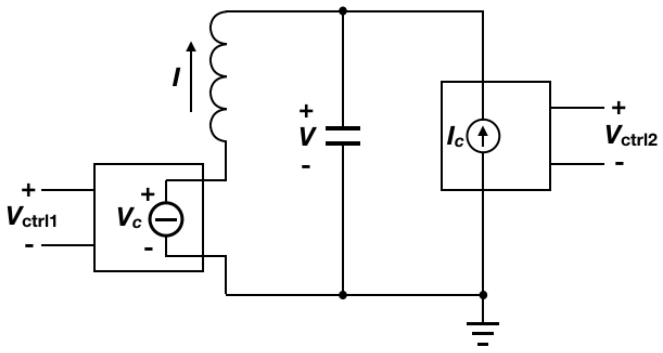

Figure 4.11: LC model for the FFE main oscillator using ideal LC components.

To match the LC model with the FFE equations, the above equations can be rewritten as

$$\sqrt{C}\frac{dV}{dt} = \frac{1}{\sqrt{LC}}\sqrt{L}(I + I_c), \tag{4.14}$$

$$\sqrt{L}\frac{dI}{dt} = -\frac{1}{\sqrt{LC}}\sqrt{C}(V - V_c), \tag{4.15}$$

Thus, from the Eq. (2.61) and (2.62) for x_1 and x_2, we can identify:

$$\hat{x}_1 = \sqrt{C}V, \tag{4.16}$$

$$\hat{x}_2 = \sqrt{L}I, \tag{4.17}$$

$$I_c = \frac{P_{11}\sqrt{C}}{r}(y - \hat{x}_1), \tag{4.18}$$

$$V_c = \frac{P_{12}\sqrt{L}}{r}(y - \hat{x}_1), \tag{4.19}$$

$$\omega = \frac{1}{\sqrt{LC}}. \tag{4.20}$$

For simulation we now somewhat arbitrarily choose the initial frequency of the main oscillator, $\omega = 1/\sqrt{LC}$, to $100MHz$ and the tuning gain k to $40MHz/V$. For an input signal $y = a\sin(\omega_{in}t)$, with $a = 0.6V$ and $\omega_{in} = 100MHz$, the LC model generates the signals x_1, x_2, x_3 and their covariance P signals are again simulated using Cadence SpectreRF and the results are shown in Figure 4.12 -

4.15.

In Figure 4.12 the estimated signals x_1 and x_2 are in phase and quadrature with input signal y, respectively. Figure 4.13 shows the dynamic performance of the frequency control voltage estimate x_3, which starts from 0V and quickly converges to the steady-state value of 0V corresponding to 100MHz.

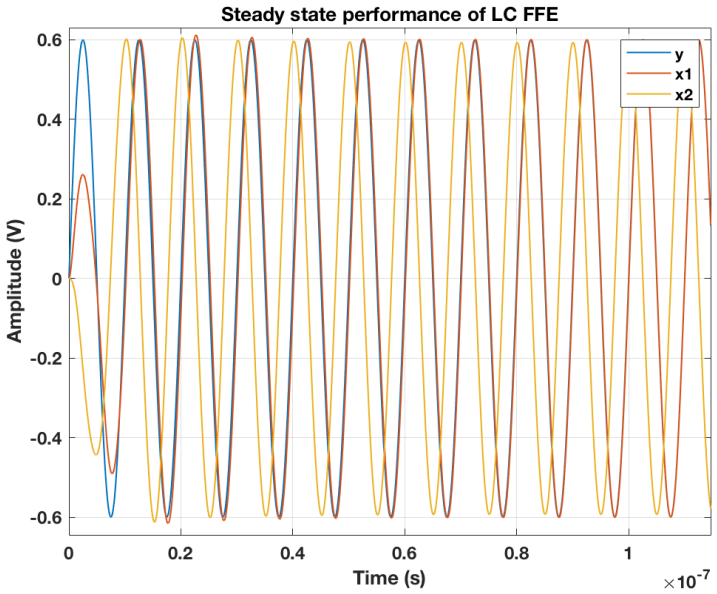

Figure 4.12: LC circuit acquisition performance using ideal LC oscillators in all the circuit blocks.

P_{13} and P_{23} shown in Figure 4.14 oscillate at the same frequency of the main oscillator, ω, and converge to the steady-state value of 0V. P_{33} shown in Figure 4.14 is the variance of x_3 with initial value of 0.5V, and converges to 0V in the steady state. P_{11} and P_{12} shown in Figure 4.15 oscillate at twice the frequency of the main oscillator, 2ω, and converge to the steady-state value close to 0V.

Figure 4.16 and 4.17 show the acquisition performance when the input frequency is $95MHz$ and $105MHz$, respectively. In both cases, the frequency estimate x_3 quickly converges to the corresponding steady-state value within 10 cycles.

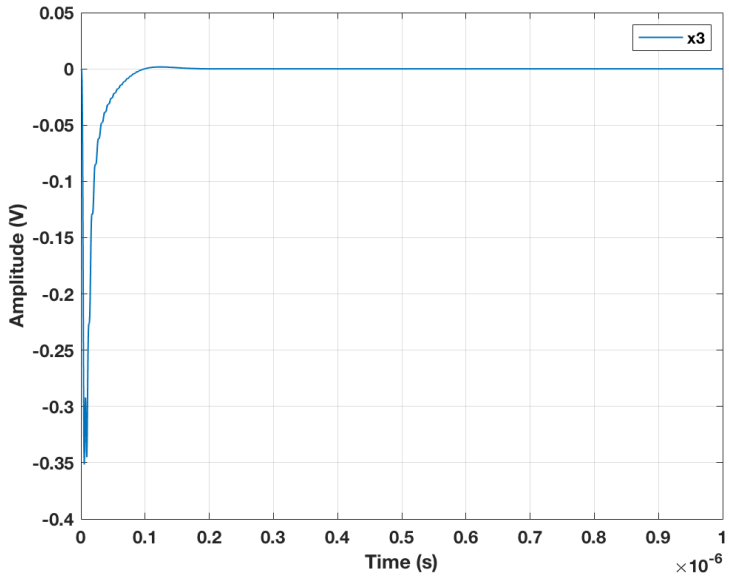

Figure 4.13: X_3 performance of ideal LC implementation showing convergence of the frequency estimate x_3 to the steady state.

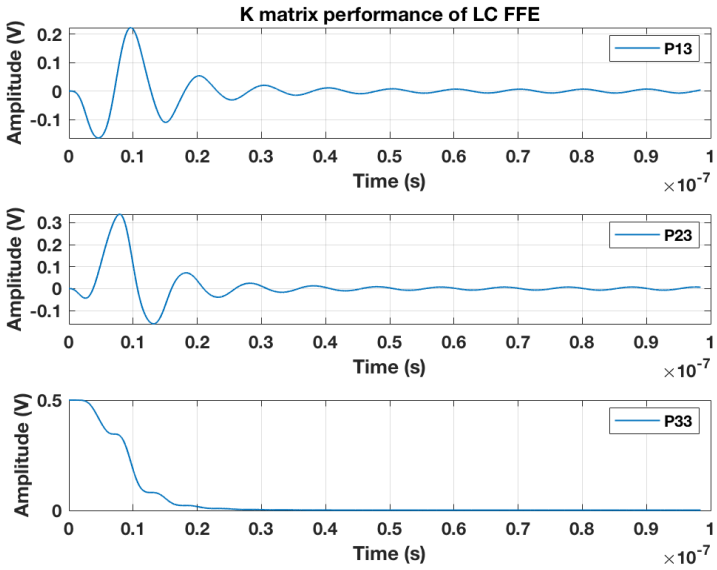

Figure 4.14: K matrix performance of ideal LC implementation, which is similar to that obtained by G_mC implementation.

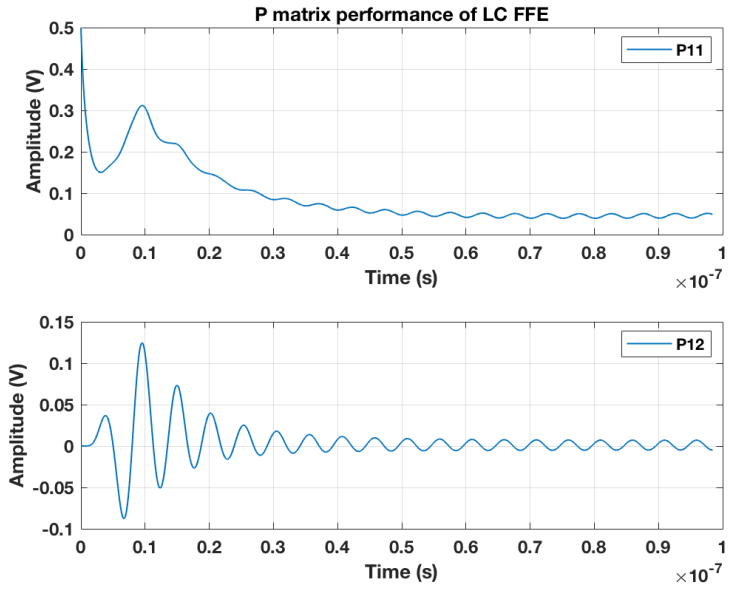

Figure 4.15: P matrix performance of ideal LC implementation, and again similar to that using G_mC circuits.

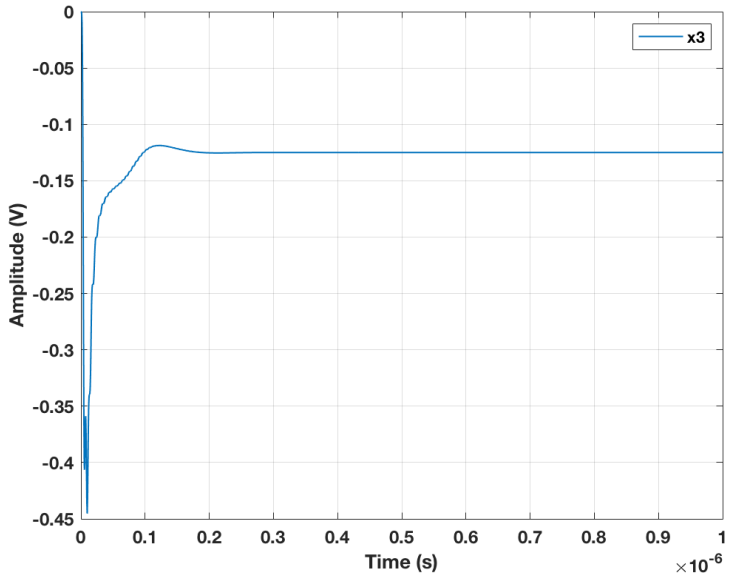

Figure 4.16: X3 performance of LC circuit with 95MHz input. The frequency estimate x_3 reaches a steady state of -0.125V with 100MHz natural frequency within around 10 cycles.

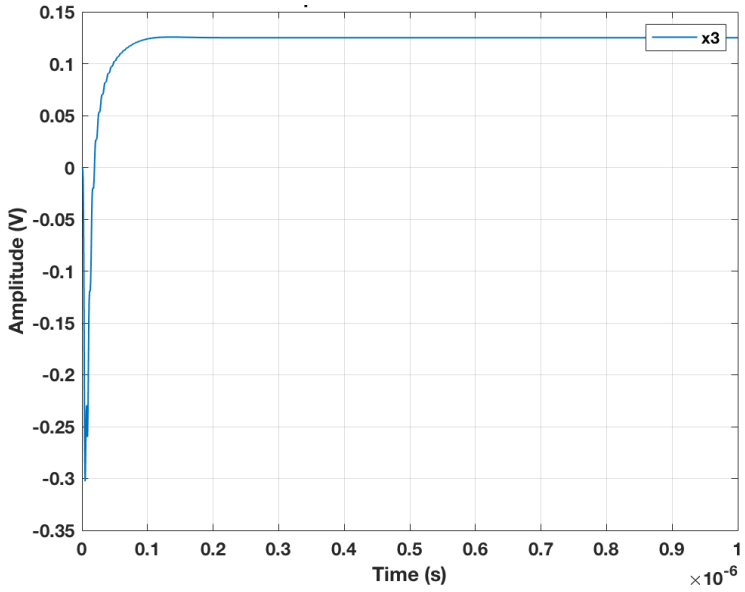

Figure 4.17: X3 performance of LC circuit with 105MHz input. The frequency estimate x_3 reaches a steady state of 0.125V with 100MHz natural frequency within around 10 cycles.

4.3 Design concerns

The nine equations show that the FFE is a complicated feedback system. For better analysis, it is important to divide them into blocks. We have found that $x_1\&x_2$, $P_{13}\&P_{23}$ and $(P_{11}-P_{22})\&2P_{12}$ can be treated as three similar blocks with natural frequency ω, ω and 2ω, separately. Also, x_3 and P_{33} can be implemented as two integrators.

4.3.1 Integrator corner frequency requirement

For both G_mC and LC models, the implementation of x_3 and P_{33} is based on a pure G_mC integrator. Eq. (2.63) and (2.66) represents ideal integrators without loss. The requirement for the practical integrator is studied based on the model in Figure 4.18. The corner frequency in Figure 4.18 is defined as $f_c = 1/2\pi RC$. For an ideal integrator, f_c is at DC. To analyze the influence of corner frequency,

two cases with different signal frequencies are studied in Table 4.1. For both input signal frequencies of $11kHz$ and $1.1GHz$ in case 1 and 3, 10^{-4} times smaller corner frequency is required to maintain FFE stable operation. Thus, the FFE has a quite stringent requirement for the integrator. This is also verified with a different Capacitor value in case 2.

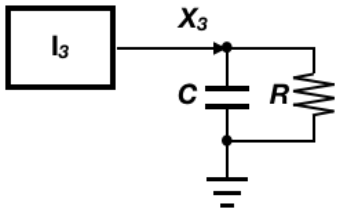

Figure 4.18: G_mC Integrator with loss, finite DC gain, and higher corner frequency relative to an ideal integrator.

Table 4.1: Requirement for integrator corner frequency is 10^{-4} times smaller than the signal frequency.

	Signal frequency(Hz)	R(Ω)	C(F)	Corner frequency(Hz)
Case 1	11k	1M	100n	1.59
Case 2	11k	100k	1u	1.59
Case 3	1.1G	1M	1p	159k

4.3.2 Main oscillator loss requirement

The ideal G_mC and LC models studied so far include no loss, but loss is unavoidable in real circuits. We now use the model in Figure 4.19 to analyze the requirement for the main oscillator block loss. When the signal frequency is $1GHz$ and $C = 1pF$, at least $R = 3.2 * 10^6$ is needed to maintain the amplitude of x_1 and x_2. Smaller R leads to an obvious decrease in the amplitude of the oscillator. Then, we can get the required minimum Q factor is $\omega RC = 2\pi * 10^9 * 3.2 * 10^6 * 10^{-12} = 2 * 10^4$, which is much higher than standard passive device Q

value. Thus, to maintain x_1 and x_2 in steady state, negative resistance is needed to compensate for the loss in the main oscillator block.

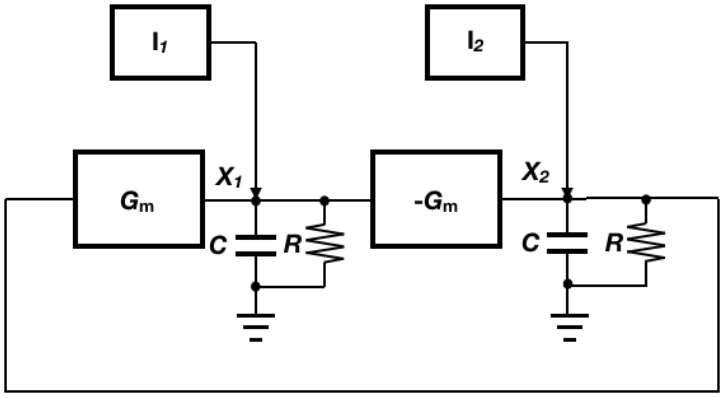

Figure 4.19: Main oscillator with loss R.

4.3.3 Frequency detuning tolerance

Ideally, the frequency of the main oscillator and K matrix blocks should be exactly the same, ω. In real circuits, there will be mismatch between each block, which causes frequency detuning. For G_mC circuits, the frequency of the main oscillator and K matrix block is decided by:

$$\omega = \omega_0 + K_v x_3 = (G_{m0} + K_0 x_3)/C, \tag{4.21}$$

For a $1GHz$ natural frequency and $400MHz/V$ tuning gain, we set $G_{m0} = 31.4m$, $K_0 = 12.56m$ and $C = 5pF$. G_{m0} determines the natural frequency and K_0 determines the tuning gain. Thus, the free running frequency is

$$f = G_{m0}/C/(2 * \pi) = 31.4m/5p/(2 * \pi) = 1GHz. \tag{4.22}$$

We can tune G_{m0} and K_0 of the K matrix block separately to determine the effect of frequency detuning between the main oscillator and K matrix block. To

better understand the influence of frequency detuning, several cases are studied for different input frequency.

For a 1.1GHz input signal, the maximum tolerated positive frequency detuning in the K matrix block caused by G_{m0} is

$$31.4m * (1.004 - 1)/5p/(2 * \pi) = 4MHz. \tag{4.23}$$

As the steady-state value of x_3 is 0.25V, the maximum tolerated positive frequency detuning in the K matrix block caused by K_v is calculated by

$$12.56m * (1.04 - 1) * 0.25/5p/(2 * \pi) = 40MHz. \tag{4.24}$$

For a 0.9GHz input signal, the maximum tolerated positive frequency detuning in the K matrix block caused by G_{m0} is

$$31.4m * (1.002 - 1)/5p/(2 * \pi) = 2MHz. \tag{4.25}$$

As the steady-state value of x_3 is -0.25V, the maximum tolerated positive frequency detuning in the K matrix block caused by K_v is calculated by

$$12.56m * (1/1.02 - 1) * (-0.25)/5p/(2 * \pi) = 20MHz. \tag{4.26}$$

Both cases show the detuning of G_{m0} in the K matrix block has more influence than that of K_0 on the FFE performance. Therefore, the requirement for the free-running frequency match between blocks is more stringent.

Next, compensation between G_{m0} and K_0 is studied for different input frequencies.

In case 1, the input signal frequency is 1.1GHz. When $G_{m0} = 31.4m*1.005$, the

FFE fails to function. Then we adjust K_0 in the opposite direction to compensate for the detuning frequency. then the FFE acquires the input signal for K_0 ranging from $12.56m/1.21$ to $12.56m/1.009$.

In case 2, the signal frequency is 0.9GHz. When $G_{m0} = 31.4m * 1.003$, the FFE again becomes unstable. Then we adjust K_0 in the opposite direction to compensate for the detuning frequency. FFE can work again for K_0 ranging from $12.56m * 1.003$ to $12.56m * 1.11$.

Both cases show that frequency detuning caused by G_{m0} can be compensated by tuning K_0 in the opposite direction, which means the frequency detuning by G_{m0} and K_0 should be considered as a whole.

Ideally, the P matrix block should be exactly twice the frequency of the main oscillator and K matrix blocks. Table 4.2 shows the maximum tolerated frequency detuning for the P matrix block. Compared with K matrix block, the P matrix block is much less sensitive to frequency detuning.

Table 4.2: P matrix frequency detuning tolerance range.

$f(Hz)$	$G_{m0}(S)$	$K_0(S/V)$	$V(V)$	$C(F)$
2.2G	62.8m/1.095∼ 62/8m*1.033	25.12m	0.25	5p
	62.8m	25.12m/100∼ 25.12m*1.38		
2G	62.8m/1.061∼ 62.8m*1.085	25.12m	4.8m	5p
	62.8m	25.12m/100∼ 25.12m*30.3		
1.8G	62.8m/1.013∼ 62.8m*1.163	25.12m	-0.25	5p
	62.8m	25.12m/100∼ 25.12m*1.17		

4.3.4 K matrix loss and frequency detuning tolerance

We have seen that the main oscillator block poles must lie close to the imaginary axis. Conversely, loss in the K matrix block can help improve the frequency detuning tolerance. Figure 4.20 shows the K matrix model with resistive loss. Maximum tolerated natural frequency ω_0 detuning for different values of the K

matrix loss is summarized in Figure 4.21 and 4.22. Both positive and negative frequency detuning show that larger loss leads to better detuning tolerance. Thus, the biasing of the K matrix circuit should be set below the criterion of oscillation.

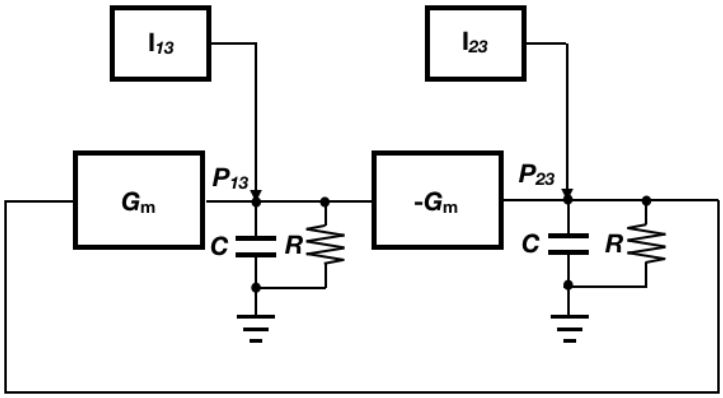

Figure 4.20: K matrix with loss R in the G_mC model.

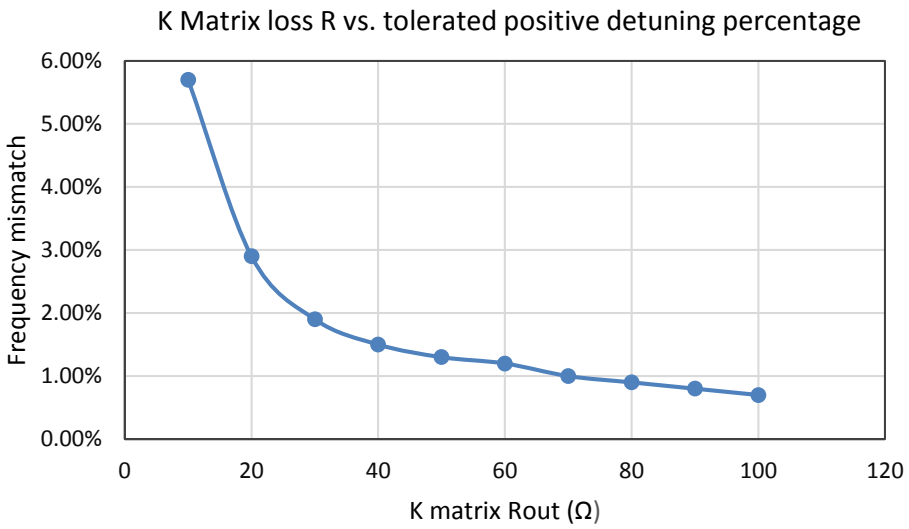

Figure 4.21: K matrix loss vs. maximum tolerated positive detuning frequency. This shows increasing tolerance to detuning as the loss increases.

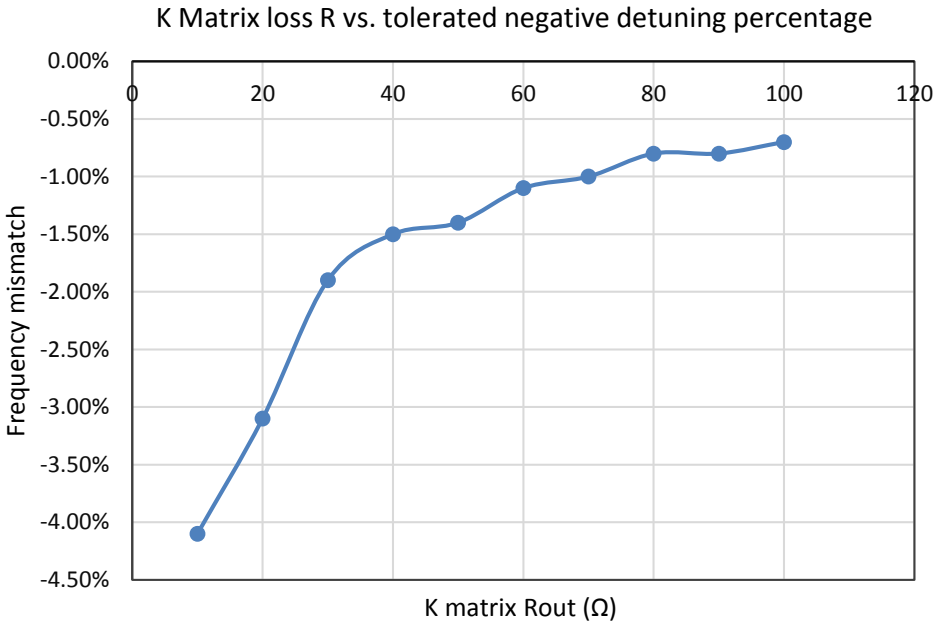

Figure 4.22: K matrix loss vs. maximum tolerated negative detuning frequency. This also shows increasing tolerance to detuning as the loss increases.

4.3.5 K matrix loss and phase delay tolerance

Besides the frequency detuning, the phase delay caused by different buffer sizes among each block is also an implementation concern. In simulation, we have observed that the FFE is much more sensitive to the phase delay in P_{11} and P_{12} signals injected into the K matrix block. The maximum tolerated phase delay in P_{11} and P_{12} for different loss R in the K matrix block is simulated in Figure 4.23. Similar to the frequency detuning tolerance, the maximum phase delay tolerance can be improved by the loss in the K matrix block.

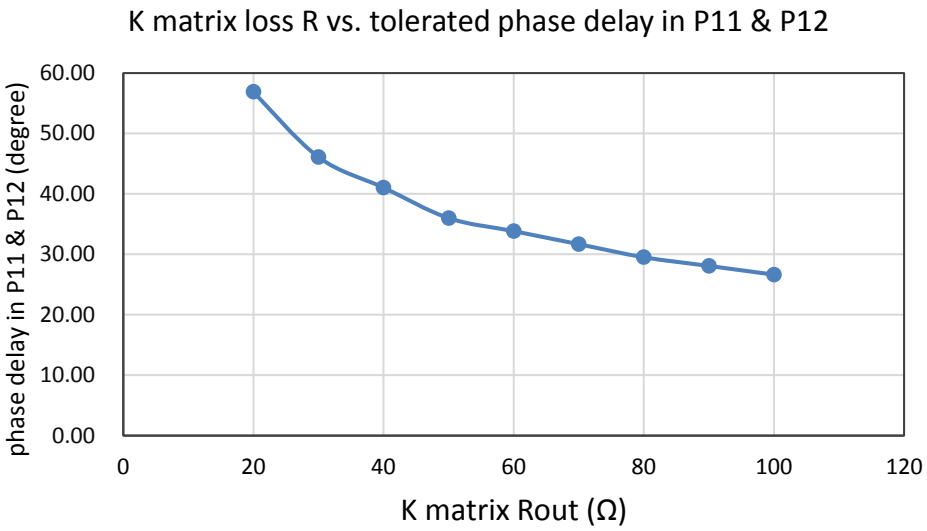

Figure 4.23: K matrix loss vs. maximum tolerated phase delay in P_{11} and P_{12}. This shows increasing tolerance to delay as the loss increases.

4.4 Summary

In this section, we discuss two types of FFE models and several design concerns in FFE implementation. First, we propose a G_mC structure and simulate the performance using the ideal behavioral model in Cadence spectreRF showing the rapid signal acquisition possible using the FFE. We then proposed and analyzed an LC structure and its performance is simulated. Based on the ideal circuit model, several design issues are investigated. First, a very low corner frequency for the x_3 integrator and a loss compensated main oscillator are required for the FFE to aquire the input signal. Then the frequency detuning tolerance between the blocks of main oscillator, K matrix and P matrix are simulated based on the G_mC structure. Finally, loss in the K matrix block is found to improve the tolerance of frequency detuning and phase delay between blocks.

Chapter 5

Main Oscillator Block Implementation Methods

Because the FFE is based on quadrature signals, we discuss the implementation of the main oscillator and its design concerns in this chapter. As for the PLL, the oscillator is the core of the FFE, which can influence at the transistor level its major performance metrics, like phase noise. There are multiple methods to implement oscillators with quadrature outputs. Before that, we need to mention an important point. Under most situations, symmetrical oscillators are necessary to obtain better rejection of supply and substrate noise. Thus, when we choose the topology for main oscillators, symmetry needs to be considered together with quadrature. In many applications, LC oscillators are chosen over ring oscillators to achieve better phase noise performance [34]. Thus, this chapter will focus on a discussion of LC oscillators implementations.

5.1 Injection locking in oscillators

In chapter 4, two ideal behavioral models are discussed for the FFE. For the implementation of the main oscillator, the LC structure has better phase noise performance, while the current injection in the G_mC structure is more straightforward to realize. Thus, an LC oscillator with injection current is studied to combine the advantages of the two proposed models.

5.1.1 Dynamics of oscillator with injection

Adler's equation [35] was developed in 1946 to analyze injection locking of oscillators, it focused on a weak injection at a nearby frequency. Figure 5.1 shows a cross-coupled LC oscillator with injection current. To understand the dynamic performance of injection, we use the polar form to denote the oscillation voltage as $a(t)\exp^{j\theta(t)}$, the oscillation current without injection is represented as $i(t)\exp^{j\theta(t)}$ and the injection current as $i_{inj}(t)\exp^{j\theta_{inj}(t)}$. Then, the LC oscillator can be modeled as Figure 5.2.

Using Kirchhoff's circuit laws, we can derive that:

$$\frac{a}{R}e^{j\theta} + C\frac{d}{dt}\left(ae^{j\theta}\right) + \frac{1}{L}\int ae^{j\theta}\,d\tau = ie^{j\theta} + i_{inj}e^{j\theta_{inj}}. \tag{5.1}$$

This integro-differential equation can be simplified as:

$$\frac{a}{R} + C\frac{da}{dt} + jca\frac{d\theta}{dt} + \frac{1}{L}e^{-j\theta}\int ae^{j\theta}\,d\tau = i + i_{inj}e^{j(\theta_{inj}-\theta)}. \tag{5.2}$$

For the integral term $Integ(t) = e^{-j\theta}\int ae^{j\theta}\,d\tau$, there is:

$$\frac{dInteg}{dt} = -je^{-j\theta}\frac{d\theta}{dt}\int ae^{j\theta}\,d\tau + e^{-j\theta}ae^{j\theta}, \tag{5.3}$$

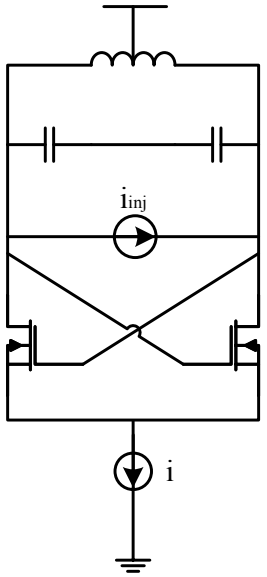

Figure 5.1: A cross-coupled LC oscillator with injection current.

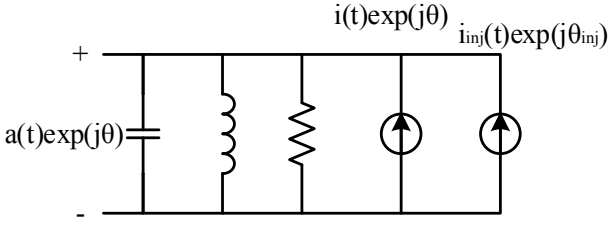

Figure 5.2: Model of LC oscillator with injection current. Polar form is used to denote the oscillation voltage as $a(t)\exp^{j\theta(t)}$, the oscillation current without injection as $i(t)\exp^{j\theta(t)}$ and the injection current as $i_{inj}(t)\exp^{j\theta_{inj}(t)}$.

which follows the first order differential equation:

$$\frac{dInteg}{dt} + j\frac{d\theta}{dt}Integ = a, \tag{5.4}$$

This equation is similar to an RC low-pass filter equation, and the solution is:

$$Integ = \frac{a}{j\frac{d\theta}{dt}}\left(1 - e^{-j\frac{d\theta}{dt}t}\right), \tag{5.5}$$

Here $j(d\theta/dt)$ is equivalent to the cutoff frequency in a low-pass filter. If the injection frequency ω_{inj} is close to free running frequency $\omega_0 = 1/\sqrt{LC}$, $d\theta/dt$ is approximately ω_0. Input $a(t)$ is the oscillation amplitude, which is also approximately constant. Thus, the output $Integ(t) \simeq a/j\frac{d\theta}{dt}$. Using a Taylor series approximation and $d\theta/dt \simeq \omega_0$, we derive

$$\begin{aligned} Integ(t) &= \frac{a}{j\omega_0\left[1+\left(\frac{1}{\omega_0}\frac{d\theta}{dt}-1\right)\right]} && (5.6)\\ &\simeq \frac{a}{j\omega_0}\left[1-\left(\frac{1}{\omega_0}\frac{d\theta}{dt}-1\right)\right] && (5.7)\\ &= -j\frac{a}{\omega_0^2}\left(2\omega_0-\frac{d\theta}{dt}\right). && (5.8) \end{aligned}$$

Eq. (5.2) can be further separated into real and imaginary parts:

$$\frac{a}{R}+C\frac{da}{dt} = i + i_{inj}\cos(\theta_{inj}-\theta), \tag{5.9}$$

$$ca\frac{d\theta}{dt}+\frac{a}{L\omega_0^2}\frac{d\theta}{dt} = \frac{2a}{L\omega_0}+i_{inj}\sin(\theta_{inj}-\theta). \tag{5.10}$$

Because $a(t)$ changes slowly, we can approximate

$$a \simeq R\left[i+i_{inj}\cos(\theta_{inj}-\theta)\right], \tag{5.11}$$

$$\frac{d\theta}{dt} = \omega_0+\frac{\omega_0}{2Q}\frac{i_{inj}\sin(\theta_{inj}-\theta)}{i+i_{inj}\cos(\theta_{inj}-\theta)}. \tag{5.12}$$

Thus, we have derived the polar-form model for an LC oscillator with injection.

5.1.2 Dynamics of the FFE main oscillator block

Here we will use the same method to analyze the amplitude and phase performance in the case of the FFE. In Eq. (2.61), we denote x_1 as $ae^{j\theta}$, and view

$P_{11}(y - x_1)/r$ as the injection signal $i_{inj}e^{j\theta_{inj}}$. Thus, x_2 is $ae^{j(\theta+\pi/2)}$ and after substitution,

$$\frac{d}{dt}\left(ae^{j\theta}\right) = (\omega_0 + kx_3)ae^{j\left(\theta+\frac{\pi}{2}\right)} + i_{inj}e^{j\theta_{inj}}, \tag{5.13}$$

$$\frac{da}{dt}e^{j\theta} + jae^{j\theta}\frac{d\theta}{dt} = j(\omega_0 + kx_3)ae^{j\theta} + i_{inj}e^{j\theta_{inj}}, \tag{5.14}$$

$$\frac{da}{dt} + ja\frac{d\theta}{dt} = j(\omega_0 + kx_3)a + i_{inj}e^{j(\theta_{inj}-\theta)}, \tag{5.15}$$

Thus, the amplitude and phase can be expressed as:

$$\frac{da}{dt} = i_{inj}\cos(\theta_{inj} - \theta), \tag{5.16}$$

$$\frac{d\theta}{dt} = (\omega_0 + kx_3) + \frac{1}{a}i_{inj}\sin(\theta_{inj} - \theta), \tag{5.17}$$

which can be rewritten as:

$$a = a_0 - i_{inj}\sin(\theta_{inj} - \theta), \tag{5.18}$$

$$\frac{d\theta}{dt} = (\omega_0 + kx_3) + \frac{i_{inj}\sin(\theta_{inj} - \theta)}{a_0 - i_{inj}\sin(\theta_{inj} - \theta)}. \tag{5.19}$$

We can notice these expressions are very similar to the general expressions for an LC oscillator with injection Eq. (5.11)(5.12), with only differences in the constant coefficients. Therefore, an LC oscillator with injection will be a possible solution for the main oscillator in the FFE.

5.1.3 Injection locking range

To discuss the requirement for injection locking, the polar-form geometry of injection is sketched in Figure 5.3, based on the model in Figure 5.2. The angle between the injection current, i_{inj}, and the oscillator current, i, is denoted as α. The total current after injection, i_{total}, is composed of i and i_{inj}. The angle ϕ between i_{total} and the tank voltage a must be equal to angle of the tank impedance at the injection locking frequency, ω_{inj} when the oscillator is injection locked. The geometry in Figure 5.3 shows that a solution exists if

$$i_{inj} \geq i \sin \phi. \tag{5.20}$$

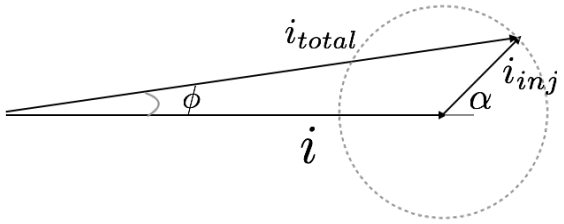

Figure 5.3: Geometrical interpretation of injection locking. The total current after injection, i_{total}, is composed of i and i_{inj}.

For an LC parallel tank in Figure 5.4, its impedance is:

$$Z(j\omega) = \frac{1}{\frac{1}{R} + j\omega C + \frac{1}{j\omega L}}, \tag{5.21}$$

Then the phase is:

$$\phi(j\omega) = -\tan^{-1} \frac{\omega C - \frac{1}{\omega L}}{\frac{1}{R}}, \tag{5.22}$$

At the injection frequency $\omega_{inj} = \omega_0 + \Delta\omega$,

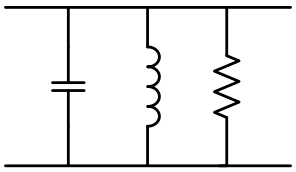

Figure 5.4: RLC in parallel.

$$\begin{aligned}
\tan\phi(j\omega_{inj}) &= R\left(\frac{1}{\omega_{inj}L} - \omega_{inj}C\right) && (5.23)\\
&= \frac{R}{(\omega_0+\Delta\omega)L} - (\omega_0 RC + \Delta\omega RC) && (5.24)\\
&= \frac{R}{\omega_0\left(1+\frac{\Delta\omega}{\omega_0}\right)L} - (\omega_0 RC + \Delta\omega RC) && (5.25)\\
&\simeq \frac{R}{\omega_0 L}\left(1-\frac{\Delta\omega}{\omega_0}\right) - (\omega_0 RC + \Delta\omega RC) && (5.26)\\
&= Q - \frac{Q}{\omega_0}\Delta\omega - Q - \frac{Q}{\omega_0}\Delta\omega && (5.27)\\
&= -2\frac{Q}{\omega_0}\Delta\omega && (5.28)
\end{aligned}$$

Thus, the oscillator locks to the injection when

$$\frac{i_{inj}}{i} \geq \frac{|\Delta\omega|}{\sqrt{\Delta\omega^2 + \left(\frac{\omega_0}{2Q}\right)^2}}. \tag{5.29}$$

The locking is remained over the frequency range $|2\Delta\omega|$ given by

$$|2\Delta\omega| = \frac{\omega_0}{Q}\frac{1}{\sqrt{\left(\frac{i}{i_{inj}}\right)^2 - 1}}. \tag{5.30}$$

5.2 Quadrature oscillators

Next we will investigate different types of quadrature oscillators for possible implementation. The study of multi-phase oscillators begins from the early 20th

century [36, 37]. Adding a divide-by-2 to a $2\omega_1$ signal is one way to generate a quadrature signal at the frequency ω_1. However, it's not a popular solution for high frequency applications, because generation of signals at $2\omega_1$ may not be realistic due to the limitations of technology. Both ring and LC oscillators can generate quadrature outputs. One major difference between them is that a ring oscillator only has one mode. This is because a ring oscillator is a single oscillator with multiple outputs, while a LC quadrature oscillator is comprosed of two oscillators injection locked to each other, and this leads to multiple modes [38].

5.2.1 Dynamics in a quadrature oscillator

In 2007, the Generalized Adler's equation [38] was introduced to reveal the dynamics of quadrature LC oscillators. Figure 5.5 shows a classic quadrature LC oscillator. The two identical oscillators are pulled to a common frequency when the first injects into the second in phase, and the second into the first out-of-phase [39].

The linear model of the oscillator is shown in Figure 5.6 [40]. G_m represents the transconductance of the negative resistance pair, G_{mc} is the transconductance of the coupling pair, and R is the loss of the LC tank.

The free running frequency of each oscillator is still $\omega_0 = 1\sqrt{LC}$ and the two locked oscillators reach a new frequency called ω_{qosc}. As we did previously with the oscillator with injection, we denote the first and second oscillator output voltage as $a_1 e^{j\theta_1}$ and $a_2 e^{j\theta_2}$. According to one method of injection, the injection current into each other is $i_{C1} = -i_C e^{j\theta_2}$ and $i_{C2} = i_C e^{j\theta_1}$. Applying Eq. (5.11) and (5.12)

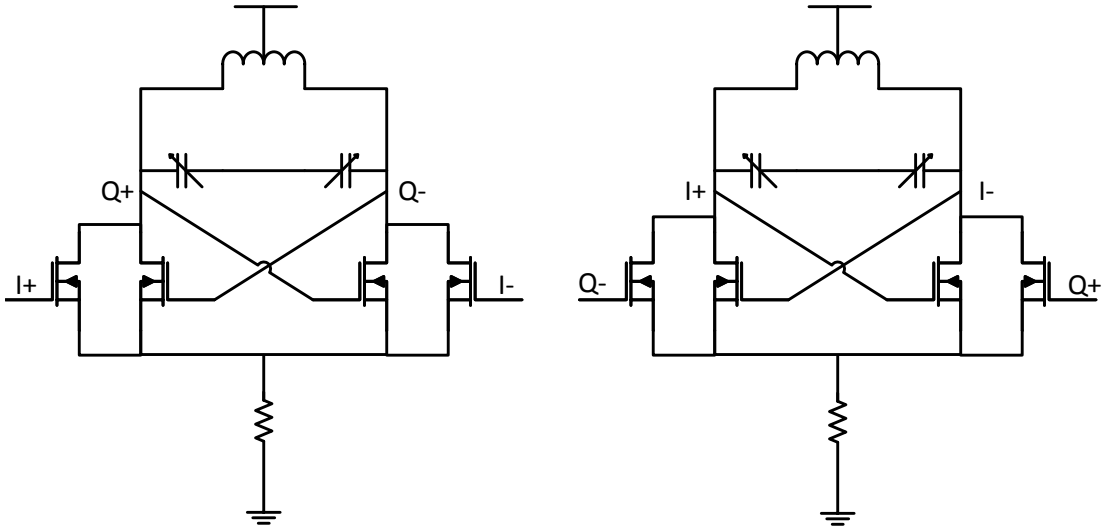

Figure 5.5: Quadrature LC cross-coupled oscillator.

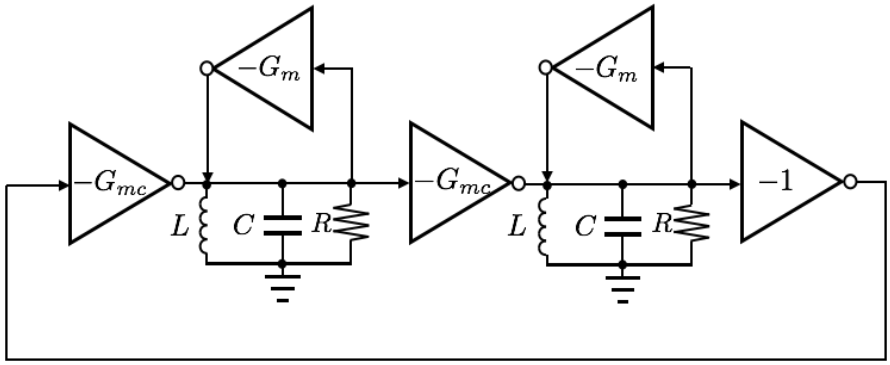

Figure 5.6: Quadrature LC cross-coupled oscillator model. G_m represents the transconductance of the negative resistance pair, G_{mc} is the transconductance of the coupling pair, and R is the loss of the LC tank.

we obtain the amplitude and phase for the quadrature oscillators:

$$a_1 \simeq R\left[i - i_C \cos(\theta_2 - \theta_1)\right], \tag{5.31}$$

$$a_2 \simeq R\left[i + i_C \cos(\theta_1 - \theta_2)\right], \tag{5.32}$$

$$\frac{d\theta_1}{dt} = \omega_0 - \frac{\omega_0}{2Q}\frac{i_C \sin(\theta_2 - \theta_1)}{i - i_C \cos(\theta_2 - \theta_1)}, \tag{5.33}$$

$$\frac{d\theta_2}{dt} = \omega_0 + \frac{\omega_0}{2Q}\frac{i_C \sin(\theta_1 - \theta_2)}{i + i_C \cos(\theta_1 - \theta_2)}. \tag{5.34}$$

5.2.2 Multi modes in LC quadrature oscillator

As mentioned before, an LC quadrature oscillator has multiple modes, which means different phase sequences. Now let's figure out which are stable oscillation modes. In stable conditions, there is $\theta_1 = \omega_{qosc}t$ and correspondingly $\theta_2 = \omega_{qosc}t + \Phi$, which results in $d\theta_1/dt = d\theta_2/dt$. From Eq. (5.33)(5.34), this results in:

$$-\frac{i_C \sin\Phi}{i - i_C \cos\Phi} = \frac{i_C \sin(-\Phi)}{i + i_C \cos(-\Phi)}, \tag{5.35}$$

$$\cos\Phi = 0, \tag{5.36}$$

$$\Phi = \frac{\pi}{2}, -\frac{\pi}{2}. \tag{5.37}$$

These two opposite phase sequences lead to oscillations with the same amplitude, but different oscillation frequencies:

$$a_{m1} = a_{m2} = Ri \tag{5.38}$$

$$\omega_{m1} = \frac{d\theta_1}{dt} = \omega_0 - \frac{\omega_0}{2Q}\frac{i_C}{i}, \tag{5.39}$$

$$\omega_{m2} = \frac{d\theta_2}{dt} = \omega_0 + \frac{\omega_0}{2Q}\frac{i_C}{i}. \tag{5.40}$$

In the FFE, if the main oscillator output x_1 and x_2 can have two stable modes, the oscillation in the K and P matrix blocks may not have the same phase sequence. This phase ambiguity can not be tolerated. It is stated in [38] that inductor series resistance leads to asymmetry in the tank impedance characteristic. When a real oscillator starts up, the initial condition varies. If two modes can exist, the one with higher gain or amplitude can outpace the other and suppress it. For a single LC oscillator, we know that the oscillation frequency is the tank resonation frequency $\omega_0 = 1/\sqrt{LC}$ and the corresponding phase shift is 0 degrees. For two coupled oscillators, we have learned there is $\pi/2$ or $-\pi/2$ phase difference

between the coupled currents. As shown in Figure 5.7, if the coupling mosfet size is the same as the biasing mosfet size, the tank phase shift will be either $\pi/4$ or $-\pi/4$.

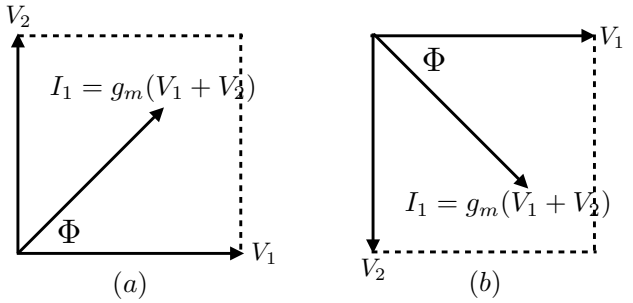

Figure 5.7: Tank phase shift of either $\pi/4$ or $-\pi/4$ when the coupling mosfet size is the same as the biasing mosfet size.

In most cases, the coupling mosfet is much smaller than the core mosfet, and the corresponding phase shift is smaller as shown in Figure 5.8.

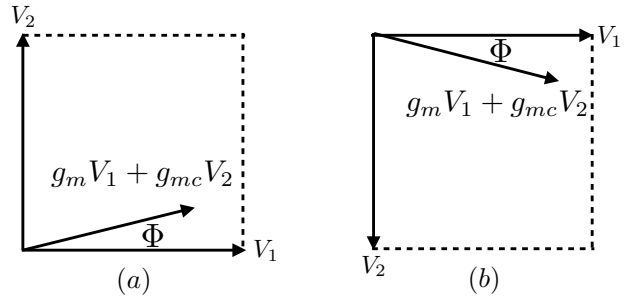

Figure 5.8: Tank phase shift when the coupling mosfet size is much smaller than the biasing mosfet size.

In Figure 5.9, for phases of $\pi/4$ and $-\pi/4$, we can find frequencies f_1 and f_2. If at f_1 or f_2, the tank impedance amplitude is larger, then the oscillator's feedback gain is larger. Thus, the corresponding phase sequence would be chosen.

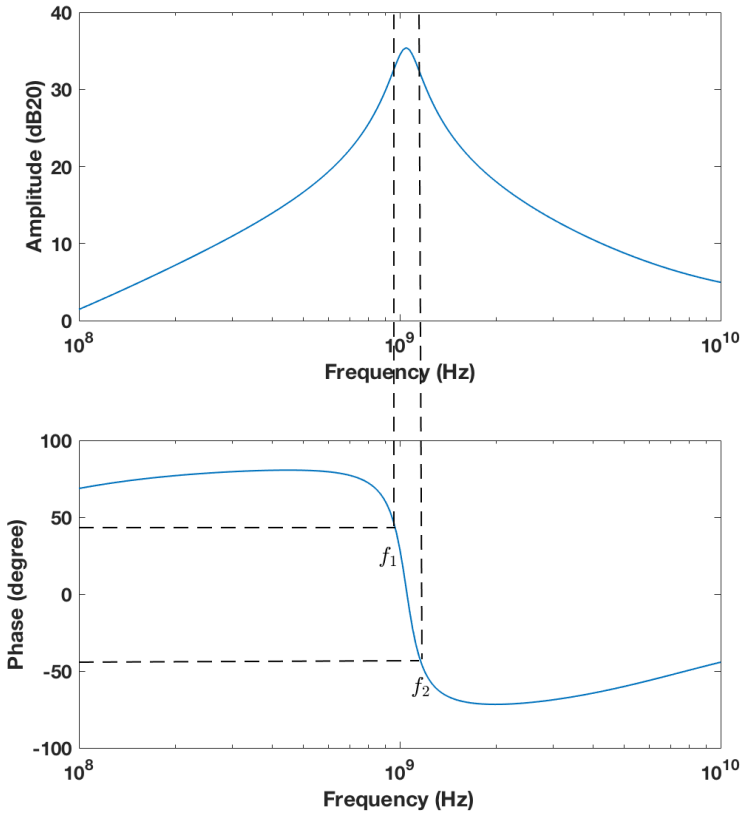

Figure 5.9: Simulated amplitude and phase of the LC tank. Frequencies f_1 and f_2 are corresponding to the phases of $\pi/4$ and $-\pi/4$. If at f_1 or f_2, the tank impedance amplitude is larger, then the oscillator's feedback gain is larger. Thus, the corresponding phase sequence would be chosen.

5.3 Proposed design

For the quadrature oscillator in the FFE, we propose the use of the LC cross-coupled oscillator shown in Figure 5.5, which can achieve good phase noise and is suitable for Gigahertz applications. Table 5.1 shows the phase noise of the differential and quadrature oscillator, separately.

Eq. (2.61) and (2.62) shows there is injection current into both quadrature outputs $x1$ and $x2$, and the injection is generated by subtraction and multiplication operations on other signals. Transconductance circuits are proposed to

Table 5.1: Phase noise of differential and quadrature oscillators

	PhaseNoise (dBc/Hz)	
Offset (Hz)	differential	quadrature
10k	-84.51	-74.64
100k	-112.8	-103.3
1M	-135.6	-131.8
10M	-157.5	-159

implement these operations. Connecting transconductance outputs together can easily implement summation or subtraction. Transconductance circuits can implement multiplication in a couple of ways [41]. The MOSFET is a transconductance device and its models in the triode and saturation regions are expressed as:

$$I_d = K(V_{gs} - V_{th} - \frac{V_{ds}}{2})V_{ds}, \qquad \text{for } V_{gs} > V_{th},\ V_{ds} < V_{gs} - V_{th}, \tag{5.41}$$

$$I_d = \frac{K}{2}(V_{gs} - V_{th})^2, \qquad \text{for } V_{gs} > V_{th},\ V_{ds} < V_{gs} - V_{th}, \tag{5.42}$$

where $K = \mu C_{ox} W/L$ is the transconductance parameter and V_{th} is the threshold voltage.

The terms $V_{gs}V_{ds}$, V_{ds}^2 and V_{gs}^2 can be used to implement multiplication. Figure 5.10 shows the realization of $V_{gs}V_{ds}$ by combining two transconductors in series. According to Eq. (5.3), when M_1, M_2 operate in deep triode region and M_3, M_4 operate in the saturation region, then $V_{gs1} = Y + y$ and $V_{ds1} = x$. Hence,

$$I_1 = K(Y + y - V_{th} - \frac{x}{2})x, \tag{5.43}$$

$$I_2 = K(Y - y - V_{th} - \frac{x}{2})x, \tag{5.44}$$

$$I_o = I_1 - I_2 = 2Kxy. \tag{5.45}$$

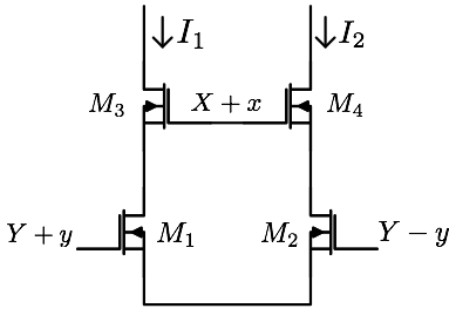

Figure 5.10: Multiplication using transconductor. When M_1, M_2 operate in deep triode and M_3, M_4 operate in saturation region, $V_{gs1} = Y + y$, $V_{ds1} = x$ and multiplication is achieved with $V_{gs1}V_{ds1}$ in I_1 and $V_{gs2}V_{ds2}$ in I_2.

To achieve better nonlinearity reduction, a fully differential configuration is proposed as shown in Figure 5.11.

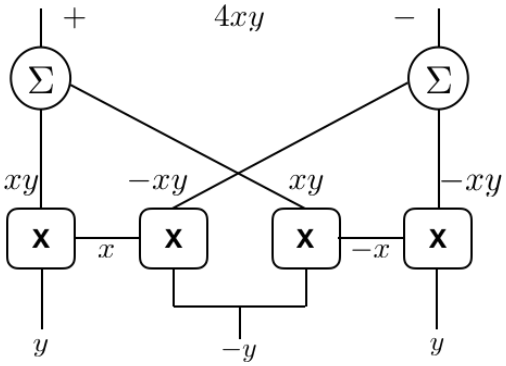

Figure 5.11: Four quadrant multiplication with better nonlinearity reduction.

Therefore, the multiplication is implemented by a multiplier shown in Figure 5.12. The constant coefficient in the FFE equation can be adjusted by the size of the output MOSFET. For this circuit the output current is:

$$I_o = I_1 + I_3 - (I_2 + I_4) = 4Kxy. \tag{5.46}$$

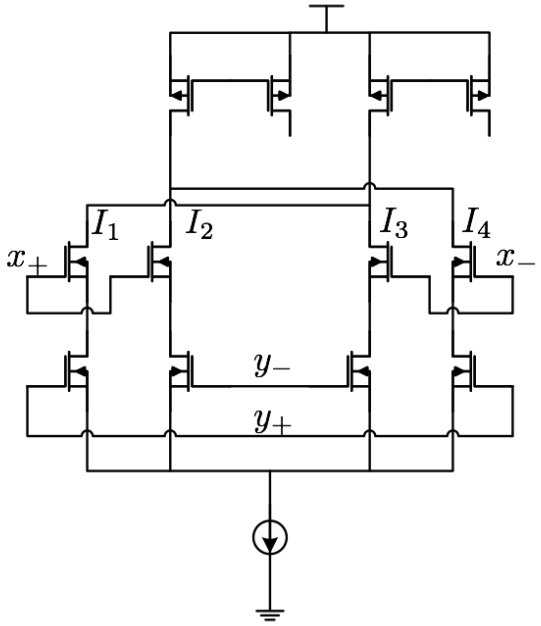

Figure 5.12: Multiplier for the main oscillator block.

Figure 5.13 - 5.15 show the performances of an ideal tank with input signal of $1GHz, 0.95GHz$ and $1.05GHz$ respectively. As the main oscillator output is not a pure sinusoidal signal, x_3 does not immediately become constant after the acquisition. The equation of x_3 indicates that a symmetrical difference between input y and main oscillator x_1 can be cancelled during integration. However, asymmetry in real x_1 would influence the steady state of x_3.

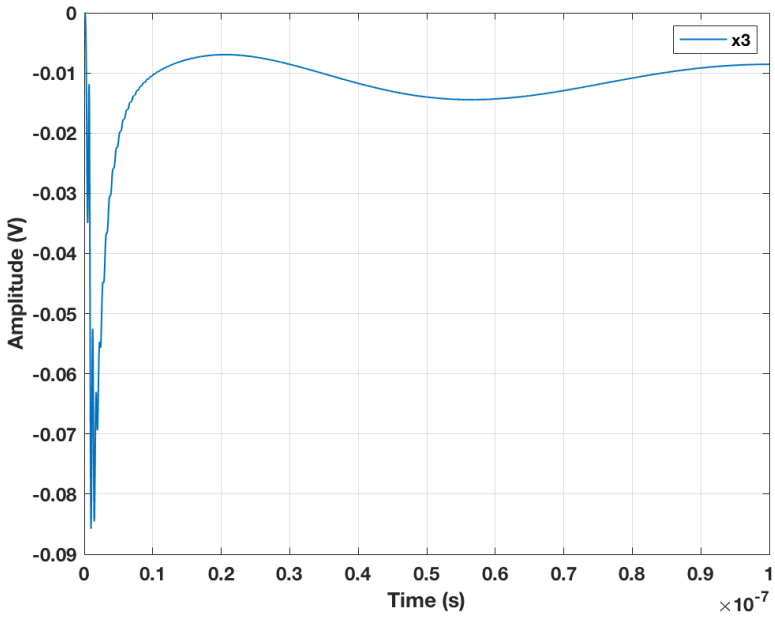

Figure 5.13: X_3 performance of the real main oscillator with 1GHz input. The frequency estimate x_3 quickly converges to 1 percent of the corresponding steady-state value within 10 cycles.

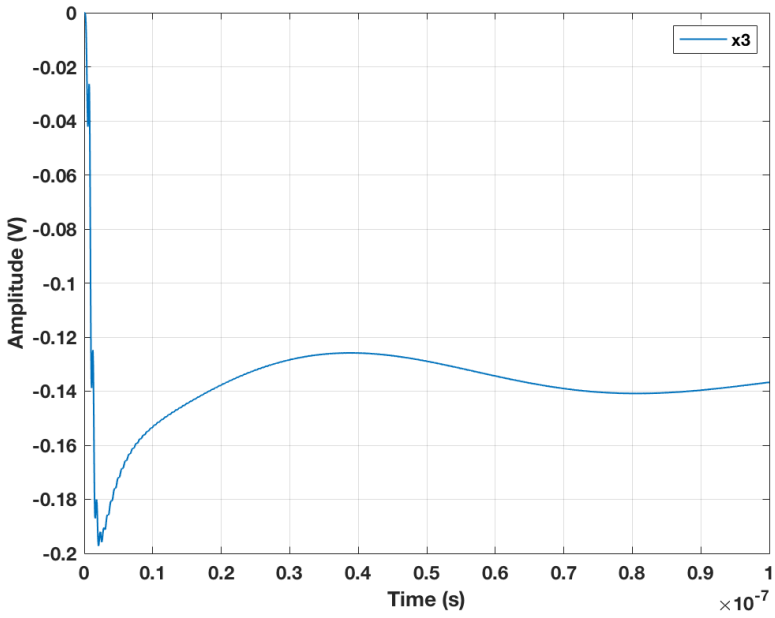

Figure 5.14: X_3 performance of the real main oscillator with 0.95GHz input.

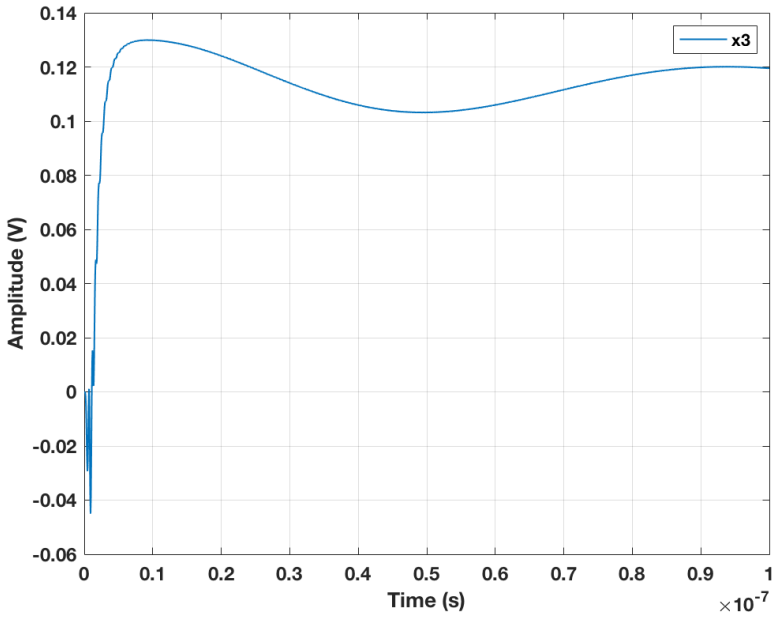

Figure 5.15: X_3 performance of the real main oscillator with 1.05GHz input.

5.4 Design constraints

In simulations, it was found that use of a real quadrature LC oscillator causes phase-sequence problems traced to its multiple modes discussed previously. Here we investigate other effects of the impedance characteristic of different LC tanks. Figure 5.16 and Figure 5.17 show the comparison of amplitude and phase for an ideal and a real LC tank. The ideal tank consists of an ideal inductor and varactor, with series resistance in the inductor. The real tank consists of PDK inductor and varactor, including additional limitations on the Q factor and nonlinearity. The comparison shows the more ideal tank has a larger Q factor and sharper amplitude and phase performance. For use in a certain quadrature oscillator, given the multi phase sequence issue, higher Q factor means that the two possible steady-state frequencies are closer. Simulations have shown that the whole FFE loop is more likely to reach a correct steady state with the ideal LC tank.

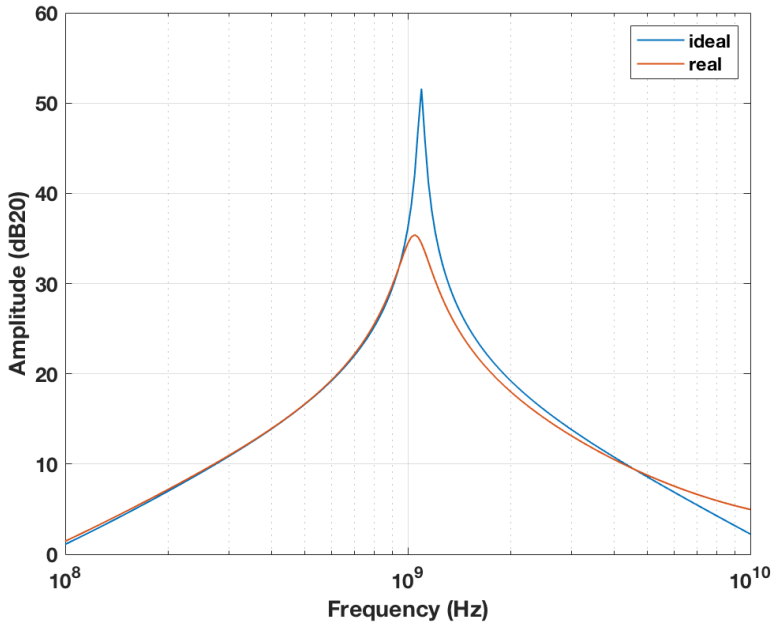

Figure 5.16: Comparison of ideal and real LC tank amplitude. The ideal tank consists of an ideal inductor and varactor, with series resistance in the inductor. The real tank consists of a PDK inductor and varactor.

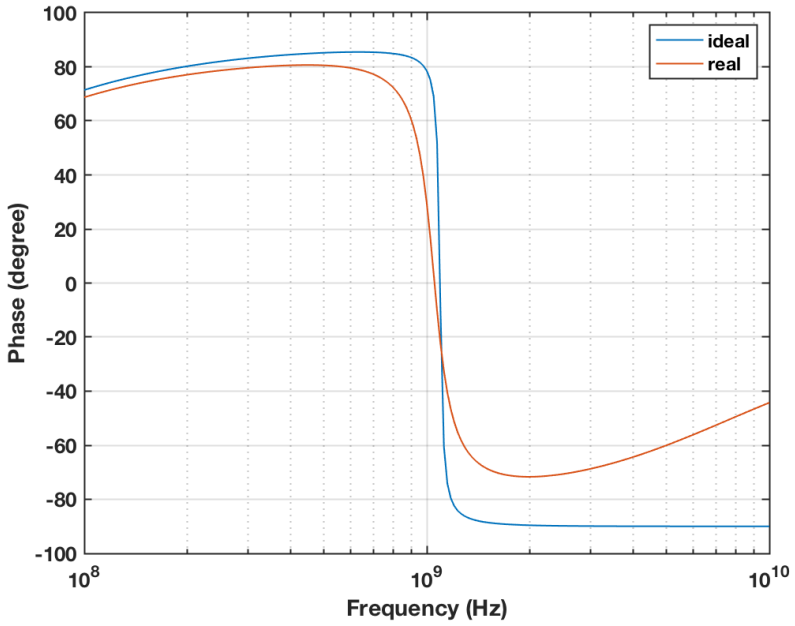

Figure 5.17: Comparison of ideal and real LC tank phase.

In simulations, we have observed two different phase sequences with the same input frequency $1GHz$. The initial frequency of the single oscillator is $0.99GHz$ and $1.046GHz$ as $x_3 = 0V$ and $x_3 = 0.6V$, separately. In Figure 5.18, the initial value of x_3 is set at $0V$ and a steady-state value of $38mV$ is achieved with x_2 leading x_1. In Figure 5.19, the initial value of x_3 is set as $0.6V$ and steady state value of $0.54V$ is achieved with x_1 leading x_2. Thus, the first case is corresponding to mode 2 with higher frequency after injection and the second case achieves the lower frequency after injection as mode 1.

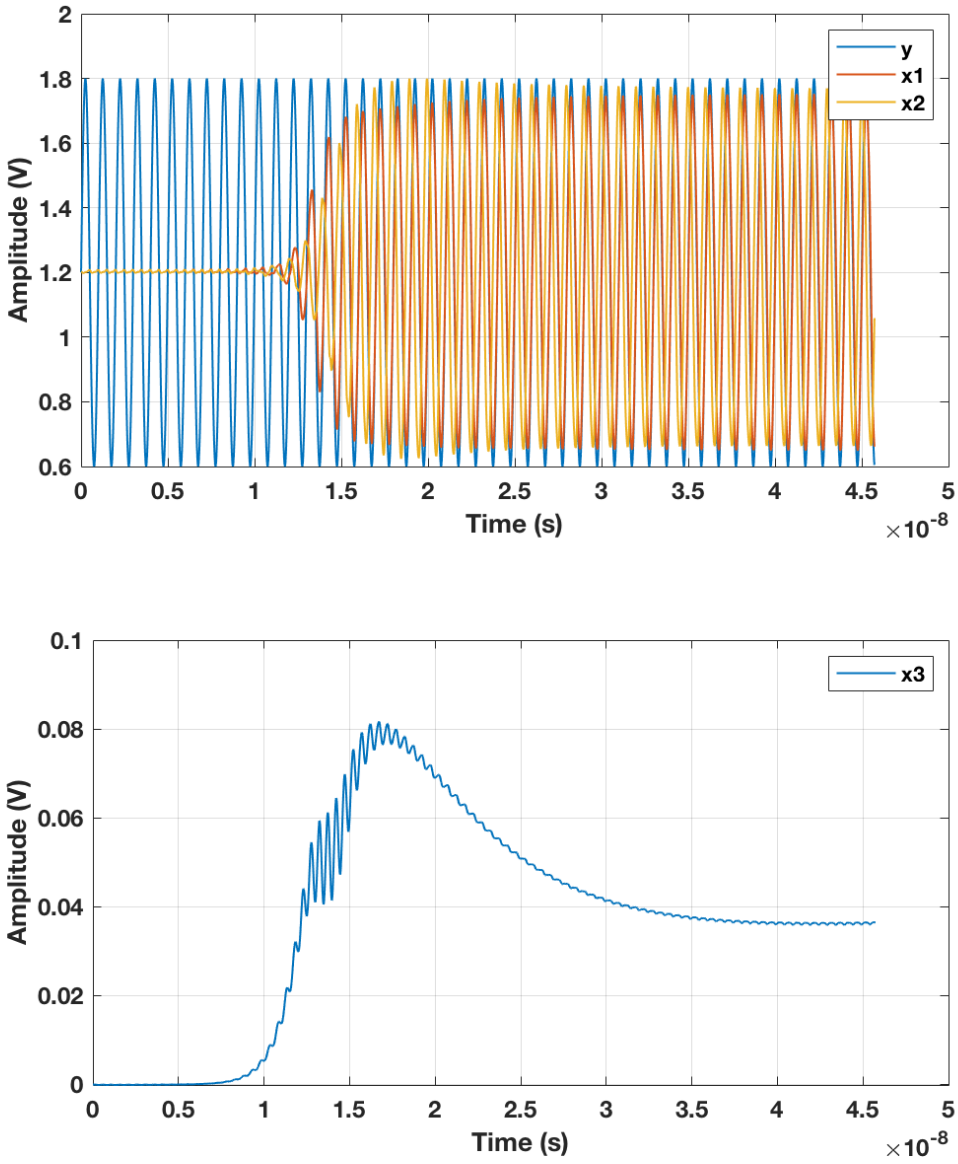

Figure 5.18: Performance of real tank with 1GHz input. The initial value of x_3 is set at $0V$ and a steady-state value of $38mV$ is achieved with x_2 leading x_1.

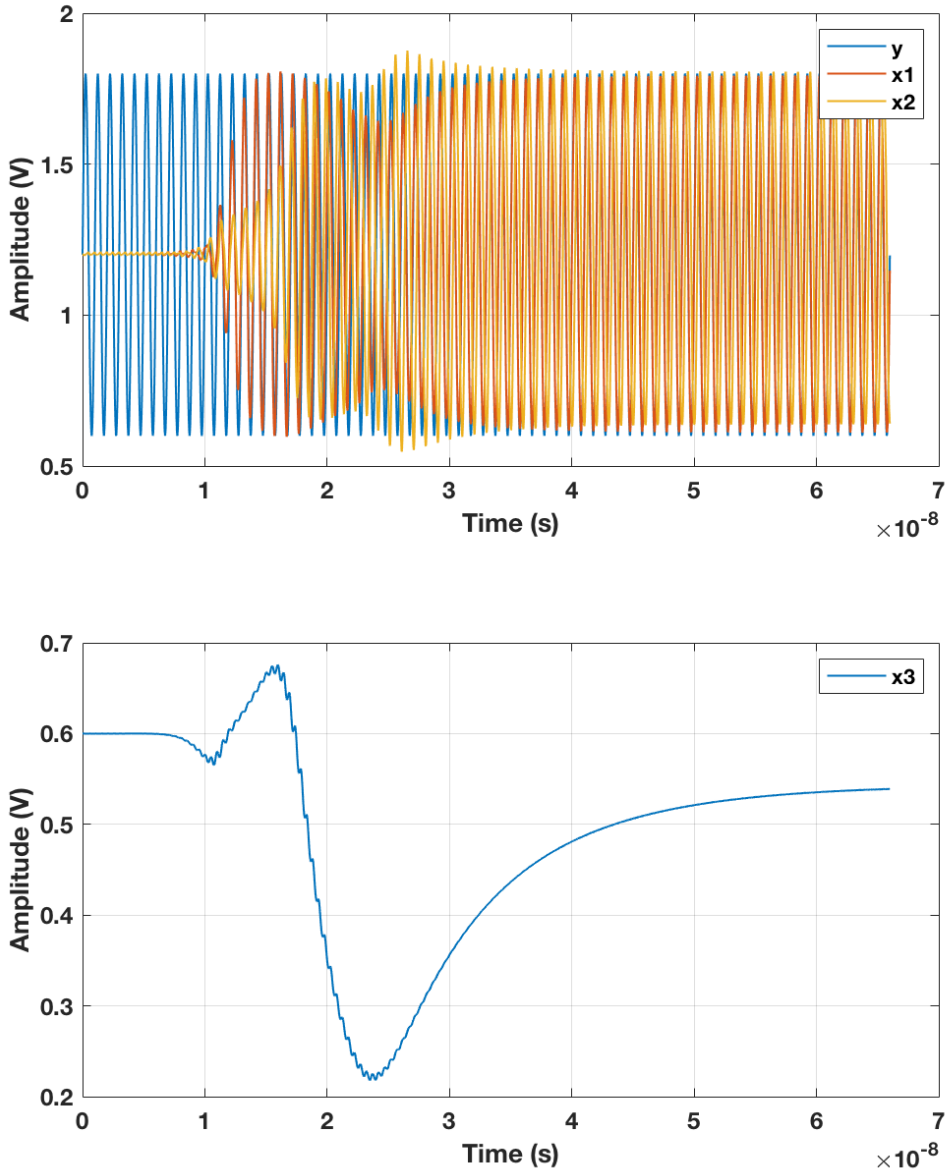

Figure 5.19: Another phase performance of real tank with 1GHz input. The initial value of x_3 is set as $0.6V$ and steady state value of $0.54V$ is achieved with x_1 leading x_2.

The varactor would convert the envelope fluctuations, amplitude modulation from the control voltage into frequency modulation noise[42]. The more nonlinear the C-V curve of varactor is, the more low-frequency noise is converted into phase noise [43]. Thus, a fixed capacitor is connected in series with the varactor to linearize the C-V curve at the expense of tuning range as in Figure 5.20. The control voltage x_3 contains a twice-frequency term, which may disturb the tank voltage and cause issues like ringing in the x_3 and wrong I/Q phase order. Thus, a biasing resistor R_{bias} is added to the varactor, which works as an isolation of the x_3 signal.

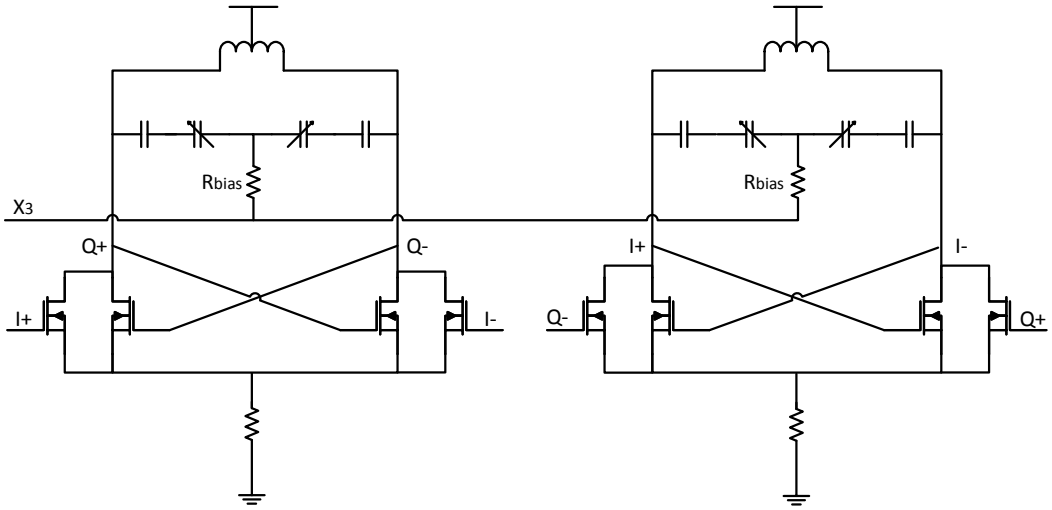

Figure 5.20: Proposed quadrature LC cross-coupled oscillator.

5.5 Summary

In this chapter, we start with different definitions of Q factor, which is a key factor in the study of the LC oscillator. We then investigate the LC oscillator with injection and its dynamic amplitude and phase equations are derived. The

LC quadrature oscillator is also investigated from the view of an oscillator with injection. The equations for the main oscillator block in the FFE show that it can be expressed as an oscillator with injections, which shares the same format as the amplitude and phase equations for the LC quadrature oscillator. Thus, a quadrature LC cross-coupled oscillator and transconductance multipliers are proposed to implement the main oscillator and its injection signals. The multi-phase sequence issue in the LC quadrature oscillator is discovered in the FFE simulation with a real oscillator tank.

Chapter 6

Implementation of the K and P Matrix Blocks

We have discussed the implementation of the main oscillator block in the previous chapters, and in this chapter, we explore the remaining K and P matrix blocks. A number of implementations are investigated, and a two-stage ring oscillator is chosen to implement the K matrix block, based on the G_mC structure discussed in chapter 4. There is feedback in both K and P matrix blocks, thus, simplification is considered and verified in both theory and simulation for these portions. The frequency, phase and amplitude curve trend are the major concerns for simplification. Finally, x_3 is implemented based on a charge pump.

6.1 Two-stage ring oscillator

Ring oscillators are widely used because they have a compact layout and can easily generate multiple phases. The basic structure of a ring oscillator is an N-stage array with negative feedback. To meet Barkhausen's criterion for oscillation, 1) the loop delay for the overall N stages should be 180 degrees; 2) the loop gain at

the oscillation frequency should be larger than 1 [44]. For the circuit in Figure 6.1, that is,

$$\phi_N(j\omega_0) = N\phi_d(j\omega_0) = \pi, \tag{6.1}$$

$$|A_N(j\omega_0)| = |A_d^N(j\omega_0)| = 1, \tag{6.2}$$

$$\omega_0 = \frac{1}{2N\tau_d}, \tag{6.3}$$

where N is the number of stages, τ_d is the time delay of each stage and A_d is the gain of each stage.

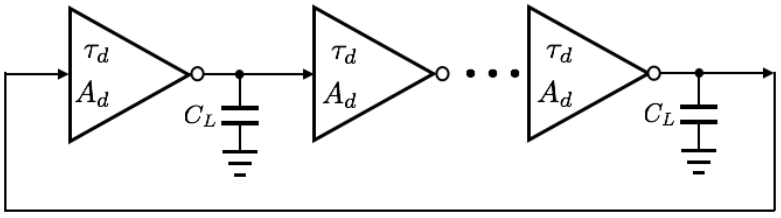

Figure 6.1: Ring oscillator model. τ_d is the time delay of each stage and A_d is the gain of each stage.

Inverters are often used as delay stages. Thus, the ring oscillator can be further modeled as in Figure 6.2 [45], where

$$A_d(j\omega) = \frac{-G_m R}{1 + j\omega RC_L}, \tag{6.4}$$

$$\phi_d(j\omega) = \tan^{-1}(\omega RC). \tag{6.5}$$

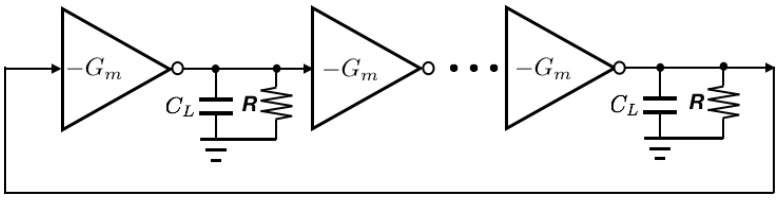

Figure 6.2: Ring oscillator model. G_m and R are used to represent inverters.

To generate quadrature outputs, a two-stage ring oscillator is considered. Eq. (6.4) shows 90 degrees is only attained when ωRC reaches infinity for one stage, which is not realistic. Thus, cross-coupled latches are used to provide additional phase delay as in Figure 6.3 [46]. This approach assumes there are two sources of phase shift, one is the RC time constant from each stage, and the other is the hysteresis from the cross-coupled latch [47].

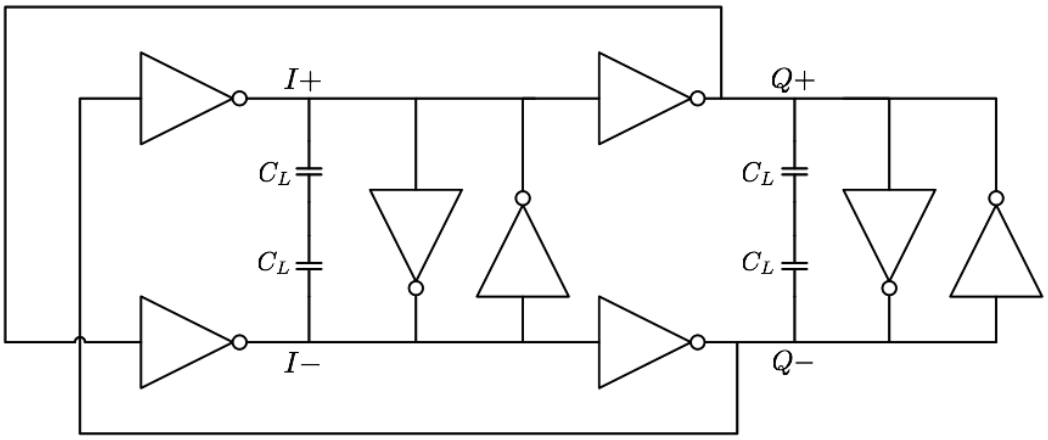

Figure 6.3: Differential two-stage ring oscillator with cross-coupled latches providing additional phase delay.

To figure out a proper latch ratio, we have simulated the phase delay for different latch ratios. For a $1GHz$ input signal, a single G_mC stage provides 73.9^o phase delay. Figure 6.4 shows another 27.4^o phase delay is provided by latch ratio of 1:1, which makes the total phase delay exceed the 90^o oscillation boundary. In Figure 6.5, a single buffer with a latch ratio of 0.6 is simulated, and a total 90.1^o phase delay is achieved. Thus, a latch ratio of 0.6 is close to the boundary of the oscillation criterion.

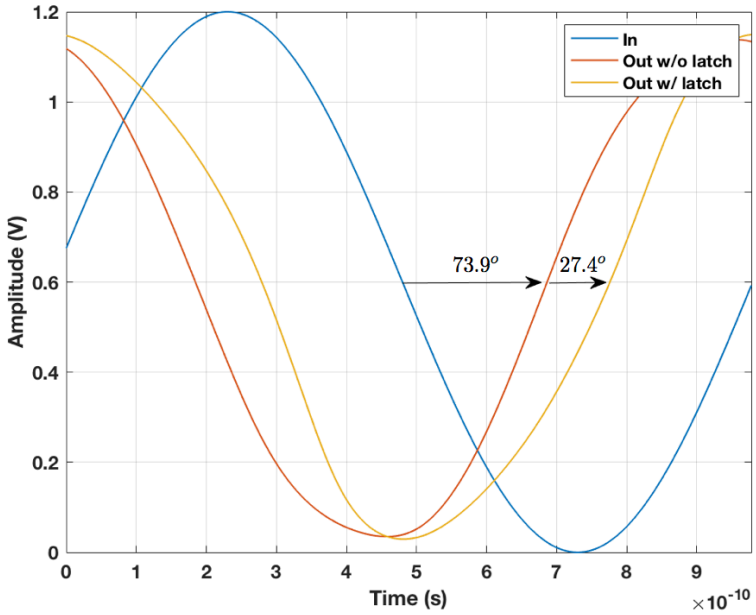

Figure 6.4: Phase delay when latch ratio is 1. Another 27.4^o phase delay provided by latches makes the total phase delay exceed the 90^o oscillation boundary.

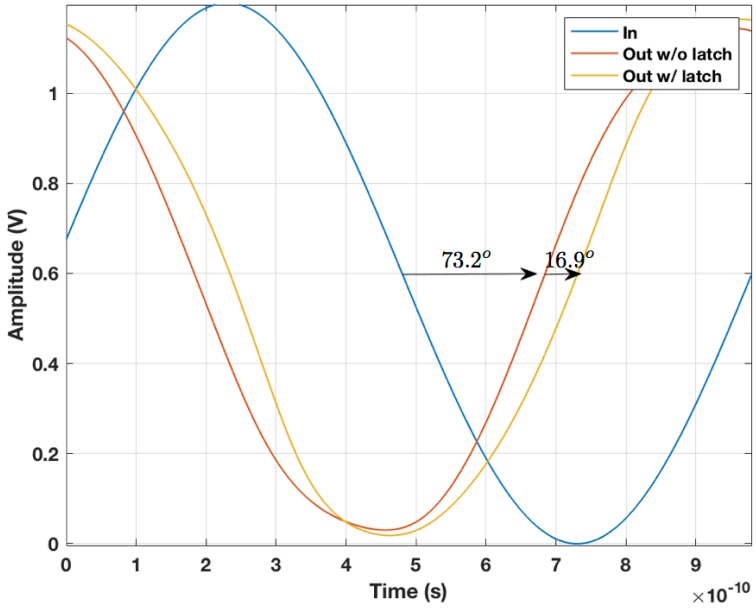

Figure 6.5: Phase delay when latch ratio is 0.6. 16.9^o phase delay provided by latches makes the total phase delay just meet the 90^o oscillation boundary.

6.2 Proposed K matrix block Implementation

In the proposed two-stage ring oscillator, Figure 6.3, the cross-coupled latch works as a negative feedback active cell G_{mc} between each stage. Thus, we obtain the model for a two-stage ring oscillator in Figure 6.6.

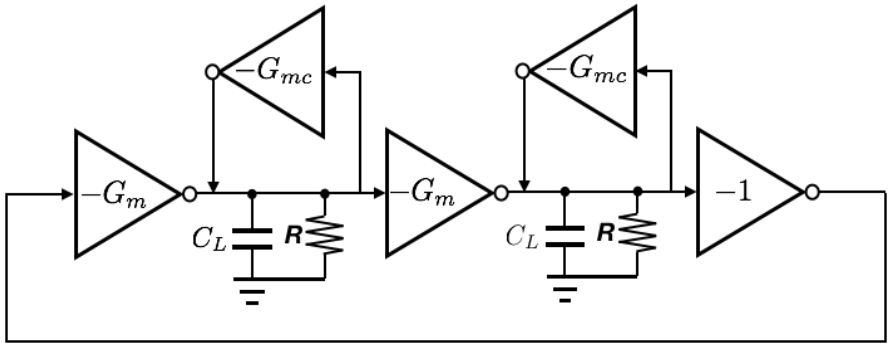

Figure 6.6: Two-stage ring oscillator model with latch feedback represented by G_{mc}.

Then, we can use a negative resistance $-R_n = -1/G_{mc}$ to represent the feedback as in Figure 6.7 [48].

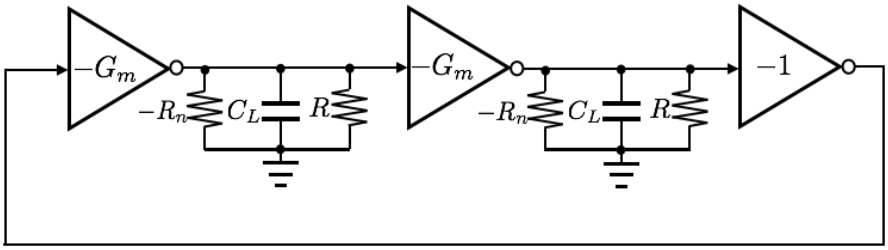

Figure 6.7: Two-stage ring oscillator model with negative resistance. Negative resistance $-R_n = -1/G_{mc}$ represents the feedback provided by latches.

Now Eq. (6.4) is

$$A_d(j\omega) = \frac{-G_m R_t}{1 + j\omega R_t C_L}, \tag{6.6}$$

where

$$R_t = \frac{-R_n R}{-R_n + R} = \frac{R}{1 - RG_{mc}}. \tag{6.7}$$

When the negative resistance R_n is large enough to compensate for the loss R, then the oscillation criterion is satisfied.

Inverters as shown in Figure 6.8 are used to implement the delay and latch stage. As we have discussed in chapter 4, the loss in the K matrix block helps the FFE tolerate frequency detuning and phase delay between blocks. Therefore, we choose the latch size ratio to be 0.5. Lower ratios may degrade the FOM of the oscillator [49].

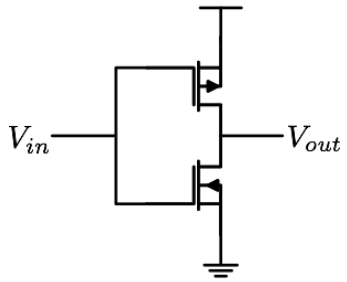

Figure 6.8: Inverter for ring oscillator.

Furthermore, to match the FFE model, injection currents are added into the two-stage ring oscillator as in Figure 6.9.

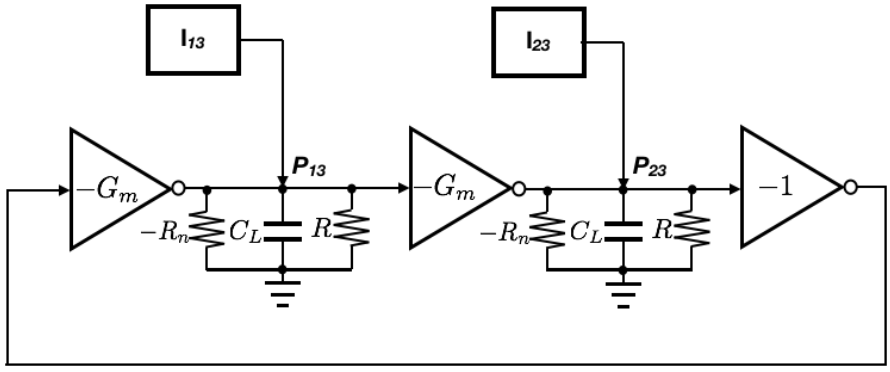

Figure 6.9: Model for the K matrix block.

6.3 Simplification of the P matrix block Implementation

In chapter 3, we have derived the phases of the P signals. We here summarize the frequency and phase of the injection signals into the P matrix block.

$$x_2 P_{13} \propto \cos\omega t \cos\omega t = \frac{1+\cos 2\omega t}{2}, \tag{6.8}$$

$$P_{11}^2 \propto (1+\cos 2\omega t)^2 = \frac{3+2\cos 2\omega t+\cos 4\omega t}{2}, \tag{6.9}$$

$$-x_1 P_{13} \propto -\sin\omega t \cos\omega t = -\frac{\sin 2\omega t}{2}, \tag{6.10}$$

$$x_2 P_{23} \propto \cos\omega t(-\sin\omega t) = -\frac{\sin 2\omega t}{2}, \tag{6.11}$$

$$P_{11} P_{12} \propto (1+\cos 2\omega t)(-\sin 2\omega t) = -\sin 2\omega t - \frac{\sin 4\omega t}{2}, \tag{6.12}$$

$$-x_1 P_{23} \propto -\sin\omega t(-\sin\omega t) = \frac{1-\cos 2\omega t}{2}. \tag{6.13}$$

Neglecting high-frequency terms, we see that the frequency and phase of x_2P_{13} and P_{11}^2 are the same as that of P_{11}. The frequency and phase of $-x_1P_{23}$ are the same as that of P_{22}. The frequency and phase of $-x_1P_{13}$, x_2P_{23} and $P_{11}P_{12}$ are the same as that of P_{12}. Hence, we investigate the use of x_2P_{13} and $-x_1P_{13}$ to take the place of the P_{11} and P_{12}, respectively. Getting rid of the oscillator operating 2ω in the P matrix can greatly simplify the FFE implementation.

Ideal G_mC behavioral model in Cadence SpectreRF is simulated to evaluate the substitution. The P matrix block is modified with the simplified implementation x_2P_{13} and $-x_1P_{13}$. Simulations show the FFE reaches the correct steady state with $1GHz$, $0.9GHz$ and $1.1GHz$ input signals. The dynamic performance of the control voltage x_3 is simulated and compared with that of the ideal P matrix block in Figure 6.10 - 6.12. With different steady-state values of $0V$, $1V$ and $-1V$, these three cases show three types of acquisition performance. The acqui-

sition time of x_3 is the same after simplification, and the damping factor can be adjusted by the output amplitude of x_2P_{13} and $-x_1P_{13}$.

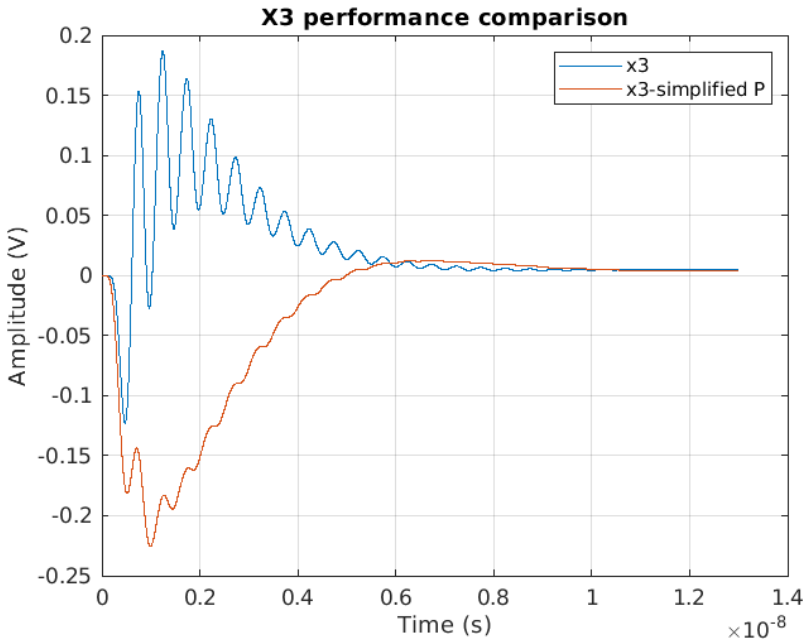

Figure 6.10: Comparison of x_3 performance when input is 1GHz. The acquisition time of x_3 is the same after simplification, and the damping factor can be adjusted by the output amplitude of x_2P_{13} and $-x_1P_{13}$.

Similarly, let's take a look at the frequency and phase of the injection signals into the K matrix block. There are

$$x_2P_{33} \propto \cos\omega t(1+\cos 2\omega t), \tag{6.14}$$

$$P_{11}P_{13} \propto (1+\cos 2\omega t)\cos\omega t, \tag{6.15}$$

$$x_1P_{33} \propto \sin\omega t(1+\cos 2\omega t), \tag{6.16}$$

$$-P_{12}P_{13} \propto -(-\sin 2\omega t)\cos\omega t = \sin\omega t(1+\cos 2\omega t). \tag{6.17}$$

Neglecting high-frequency terms, the frequency and phase of x_2P_{33} and $P_{11}P_{13}$ are the same. Also, x_1P_{33} and $-P_{12}P_{13}$ are the same. Thus, we can simplify the injection signals to x_2P_{33} and x_1P_{33} only.

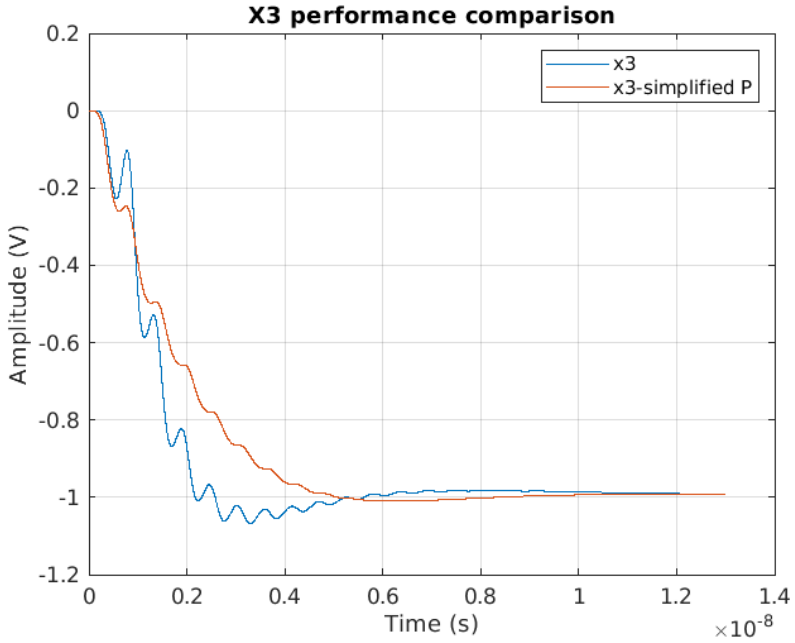

Figure 6.11: Comparison of x_3 performance when input is 0.9GHz. The acquisition time of x_3 is also the same after simplification.

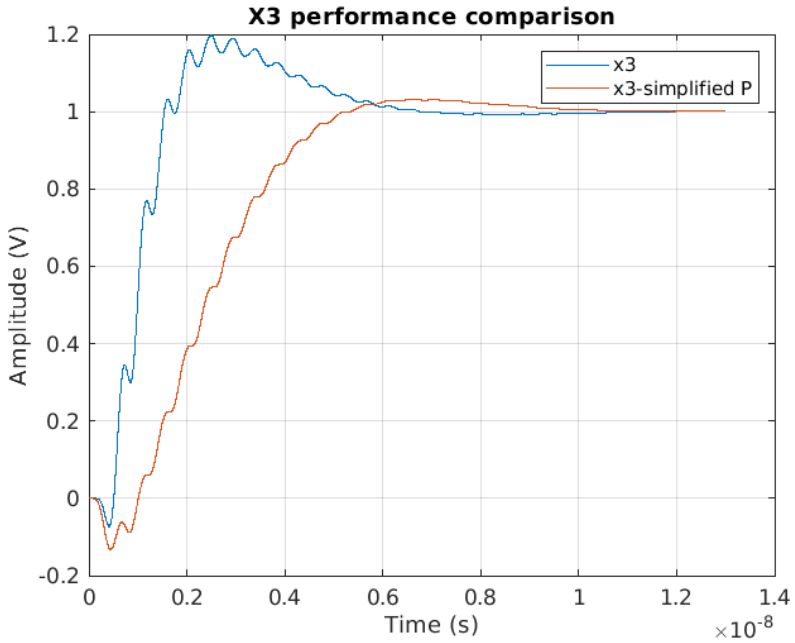

Figure 6.12: Comparison of x_3 performance when input is 1.1GHz. The acquisition time of x_3 is also the same after simplification.

6.4 Proposed P matrix block

A fully differential structure has better common-mode noise rejection and better distortion performance [50]. Figure 6.13 is the fully differential multiplier to implement P_{11} and P_{12}. The multiplier outputs x_2P_{13} and $-x_1P_{13}$ are simulated

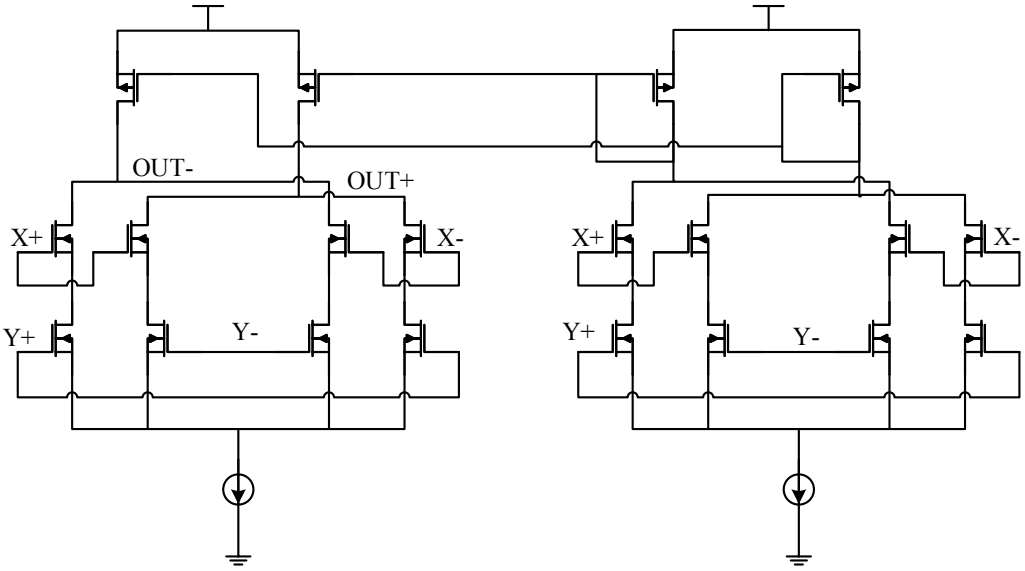

Figure 6.13: Multiplier for P matrix.

and compared with ideal P signals in Figure 6.14 and 6.15. As the simplified P_{11} and P_{12} are the same as P_{11} and P_{12} in both frequency and phase, the remaining issue is the amplitude performance during the acquisition. If the model fits the data well, the P matrix tends to a matrix of zero values. Thus, the changing trend of the amplitude needs to be compared. In Figure 6.14 and 6.15, both magnitudes of P_{11} and P_{12} decrease until close to zero when the FFE reaches steady state and the changing trend of x_2P_{13} and $-x_1P_{13}$ is the same as that of P_{11} and P_{12}, respectively.

Now we can simulate the FFE performance with the proposed main oscillator, K and P matrix blocks. In Figure 6.16, the main oscillator takes about 10 more

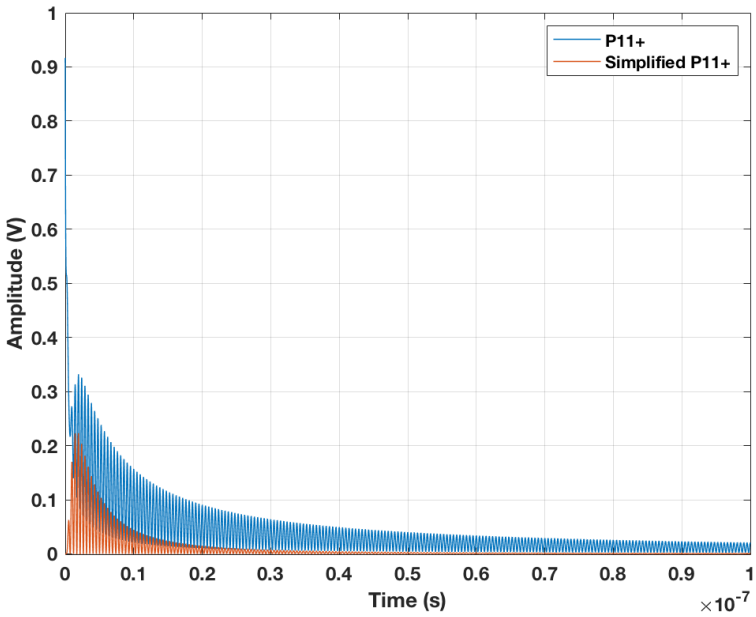

Figure 6.14: Comparison of ideal P_{11} and proposed substitution x_2P_{13}. The frequency, phase and trend of x_2P_{13} is the same as that of P_{11}.

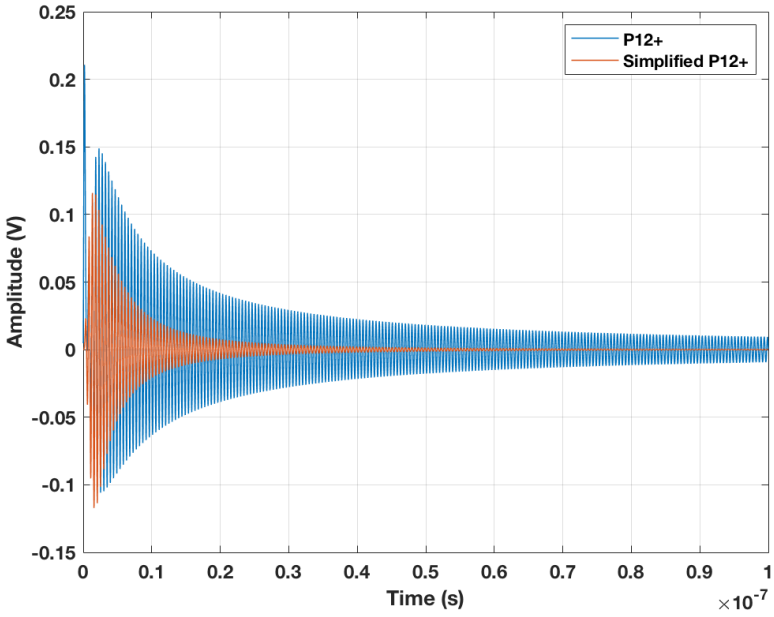

Figure 6.15: Comparison of ideal P_{12} and proposed substitution$-x_1P_{13}$. The frequency, phase and trend of $-x_1P_{13}$ is the same as that of P_{12}.

cycles to start up with real K and P matrix blocks compared with ideal K and P matrix blocks. Figure 6.17 and 6.20 show the acquisition of x_3 with input signal of $1.05GHz$ and $0.95GHz$, respectively. In both cases, the frequency estimate x_3 quickly converges to 1 percent of the corresponding steady-state value within 10 cycles. Compared with ideal implementation, the K matrix block signals P_{13} and P_{23} contain obvious high-order frequency terms as in Figure 6.18. In Figure 6.19, the decreasing rate of P matrix signals P_{11} and P_{12} is slower than that in Figure 4.8 due to the simplification. However, simulation shows that the acquisition time of FFE won't be much influenced, which is still around 10 cycles.

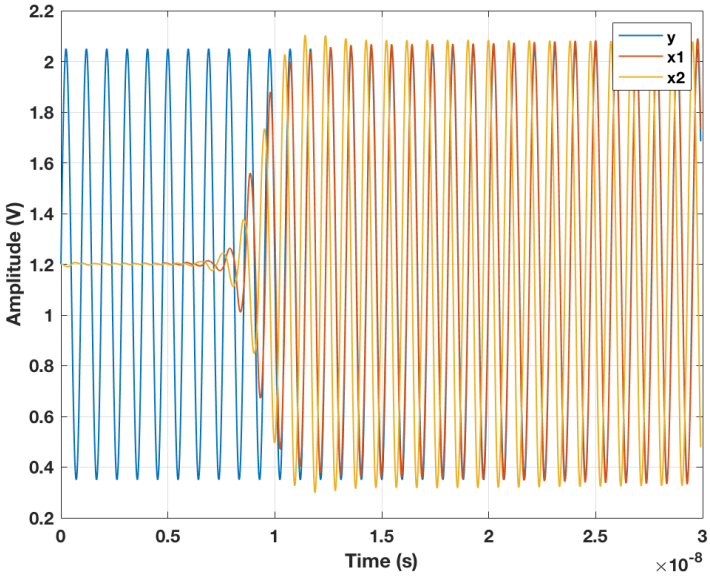

Figure 6.16: Performance of the real main oscillator, K and P matrix blocks with 1.05GHz input. The main oscillator takes about 10 more cycles to start up with real K and P matrix blocks compared with ideal circuits.

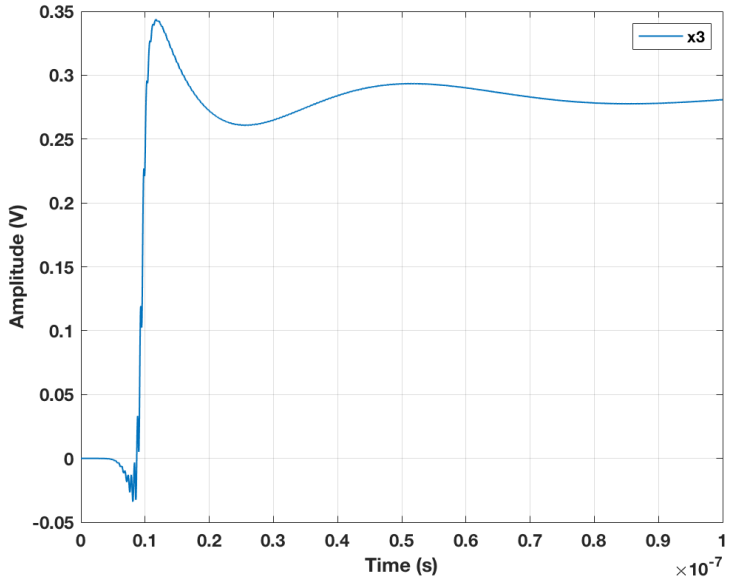

Figure 6.17: X3 performance of the real main oscillator, K and P matrix blocks with 1.05GHz input. The frequency estimate x_3 quickly converges to 1 percent of the corresponding steady-state value within 10 cycles.

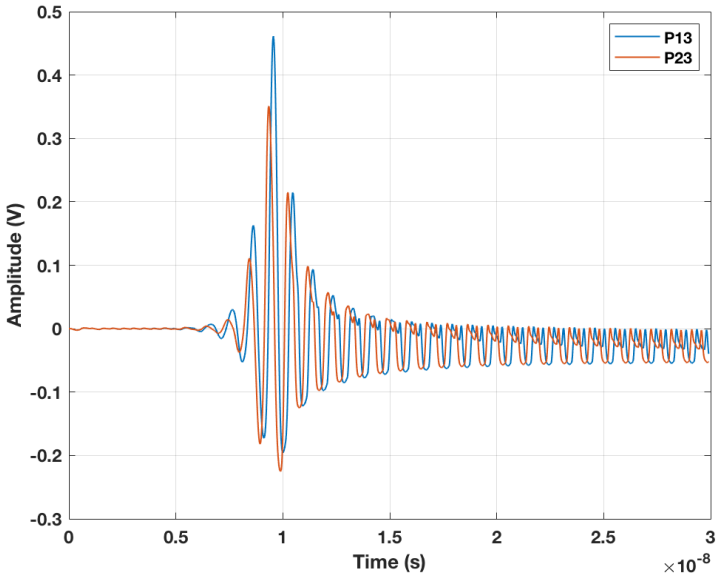

Figure 6.18: K matrix performance of the real main oscillator, K and P matrix blocks with 1.05GHz input. Compared with ideal implementation, P_{13} and P_{23} contain obvious high-order frequency terms.

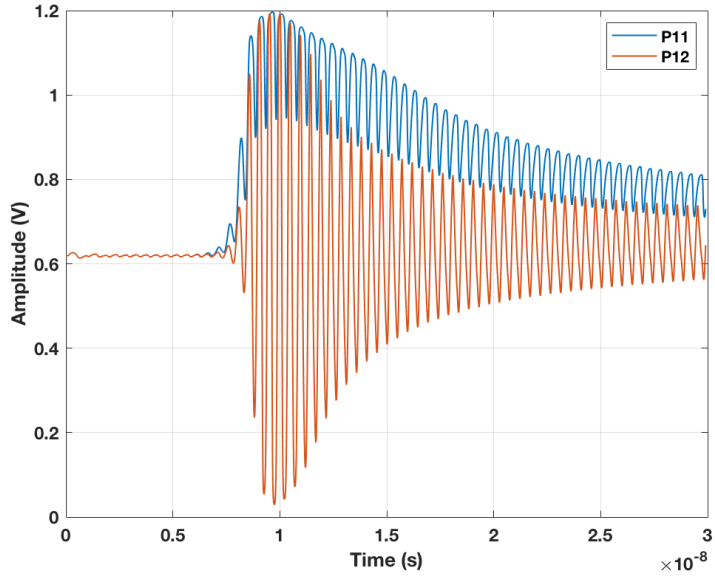

Figure 6.19: P matrix performance of the real main oscillator, K and P matrix blocks with 1.05GHz input. The decreasing rate of P matrix signals P_{11} and P_{12} is slower due to the simplification.

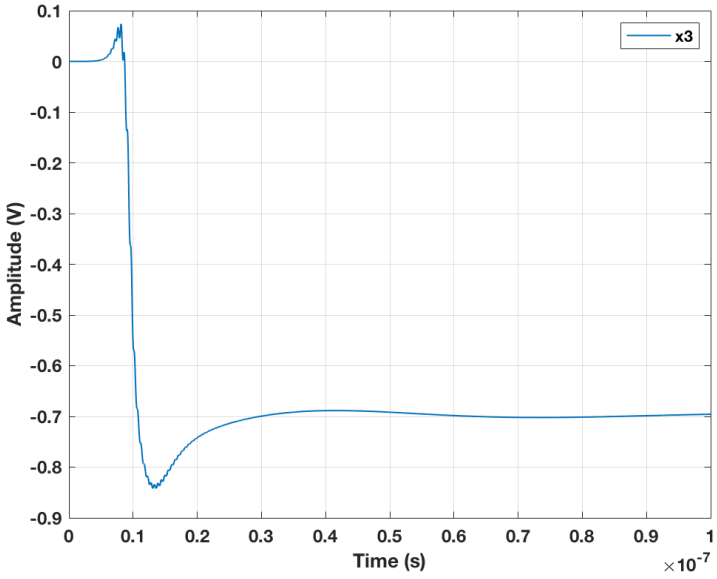

Figure 6.20: X3 performance of the real main oscillator, K and P matrix blocks with 0.95GHz input. The frequency estimate x_3 quickly converges to 1 percent of the corresponding steady-state value within 10 cycles.

6.5 Proposed X3 implementation

Figure 6.21 shows the implementation of x_3, based on the derived x_3 model Eq. 3.51. P_{13} is multiplied by input y and x_1, respectively, and both multiplication results are fed into the current sink or source driving a capacitor C. This current sink/source is similar to the charge pump in PLL [51]. During each signal period, the output voltage x_3 changes when y and x_1 are different, and the changing voltage Δx_3 is decided by the phase difference $\Delta\phi$ and the amplitude of P_{13}.

$$\Delta x_3 = \frac{\Delta Q}{C} = \frac{a_{13}\Delta t I_{CP}}{C} \tag{6.18}$$

$$= \frac{\Delta\phi}{2\pi} T_{in} \frac{a_{13} I_{CP}}{C}. \tag{6.19}$$

Note that x_3 remains constant when $y * P_{13}$ is equal to $x_1 * P_{13}$, and changes when

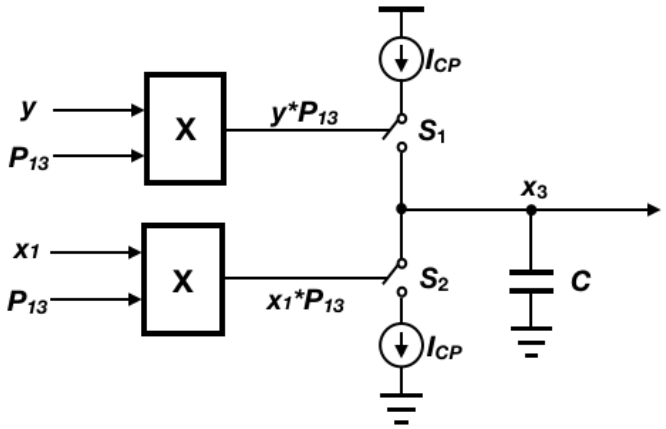

Figure 6.21: Model for X3 implementation. $y * P_{13}$ and $x_1 * P_{13}$ are fed into the current sink or source driving a capacitor C.

there is a difference. Hence, the changing rate of x_3 is nonlinear. We can linearize the voltage change by approximating it as a ramp with a slope of:

$$\frac{dx_3}{dt} \simeq \frac{\Delta x_3}{T_{in}} = \frac{\Delta\phi}{2\pi} \frac{a_{13} I_{CP}}{C}. \tag{6.20}$$

This approximated model matches with Eq. (3.51), where

$$\frac{a}{2r} = \frac{I_{CP}}{2\pi C}. \tag{6.21}$$

Figure 6.22 shows the performance for the FFE fully implemented in Cadence SpectreRF. To implement this x_3, $P_{13} * y$ and $P_{13} * x_1$ are generated in Figure 6.23. As we have derived in chapter 3:

$$P_{13} * y = \cos\omega t * \sin(\omega t + \phi_{ex}) = \frac{\sin 2\omega t}{2} + \frac{1 + \cos\omega t}{2}\phi_{ex}, \tag{6.22}$$

$$P_{13} * x_1 = \cos\omega t * \sin\omega t = \frac{\sin 2\omega t}{2}. \tag{6.23}$$

The amplitude difference of $P_{13} * y$ and $P_{13} * x_1$ contains the information of the excess phase between y and x_1.

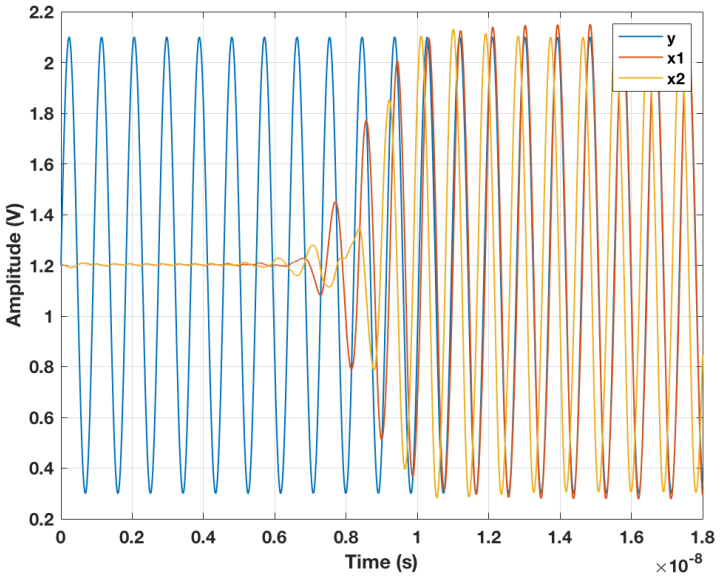

Figure 6.22: Performance of real FFE with 1.1GHz input.

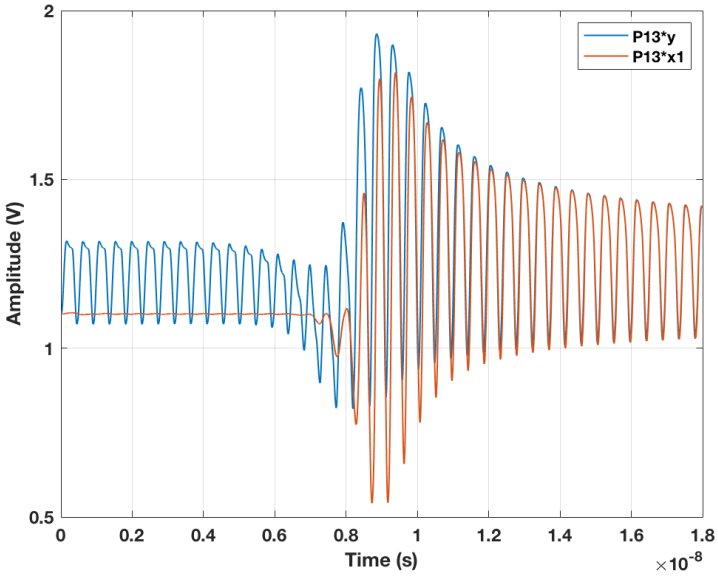

Figure 6.23: Comparison of $P_{13} * y$ and $P_{13} * x_1$. The amplitude difference of $P_{13} * y$ and $P_{13} * x_1$ contains the information of the excess phase between y and x_1.

Then, the inverters are used as buffers to generate the control signals UP and DOWN into the charge pump as in Figure 6.24. Finally, in Figure 6.25, x_3 changes with the pulse width differences between UP and DOWN according to the phase difference between $P_{13} * y$ and $P_{13} * x_1$, then reaches steady state within 10 cycles.

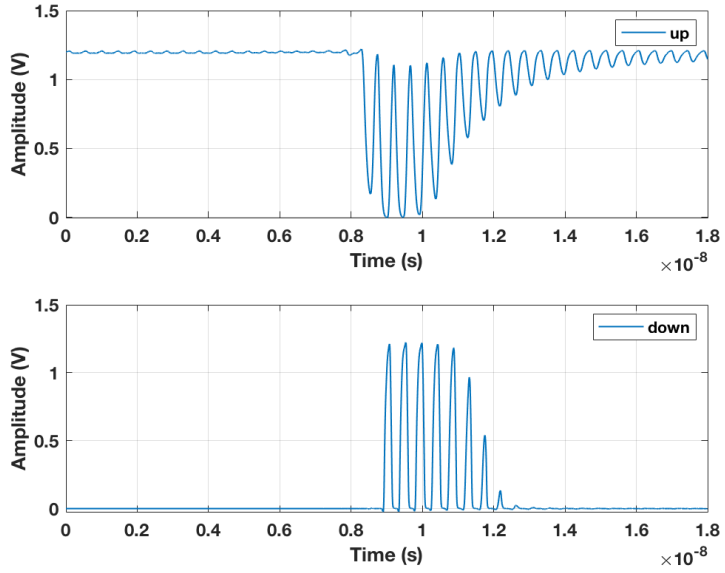

Figure 6.24: Up and down signals from $P_{13} * y$ and $P_{13} * x_1$.

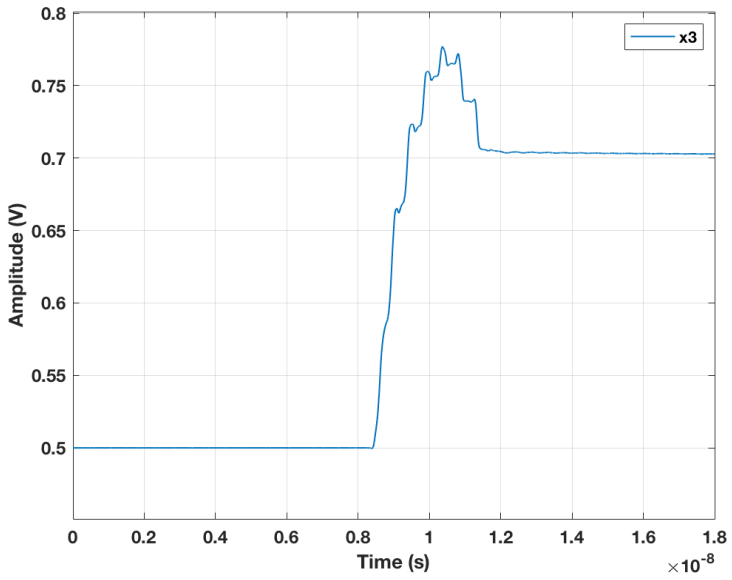

Figure 6.25: X3 Performance of real FFE with 1.1GHz input. x_3 changes with the pulse width differences between UP and DOWN according to the phase difference between $P_{13} * y$ and $P_{13} * x_1$, then reaches steady state within 10 cycles.

6.6 Summary

In this chapter, we discussed the implementation of the K matrix and P matrix blocks. First, a 2-stage ring oscillator is studied and used for the K matrix block. We then explore the simplified implementation of K and P matrix blocks. The phases of all the signals are studied to support the simplification in theory. We also made a simulation experiment and have demonstrated that simplified P_{11} and P_{12} can keep the performance of frequency, phase and amplitude curve trend. The implementation of x_3 is based on the concept of a charge pump. The difference is that the control signals have brought in P_{13} by multiplication. Finally, the whole FFE system is simulated in Cadence spectreRF.

Chapter 7

Conclusion

A frequency estimator based on the Kalman filter has been widely studied and designed. Different models have been discussed in discrete time or continuous time. However, we found that the implementation of the Kalman filter based estimator was rarely studied. We, therefore, intend to implement an estimator in analog integrated circuits that could, to some degree, fill the blank. The contribution of the dissertation work can be summarized in the following four paragraphs.

We derived both the discrete-time and continuous-time state space models for the FFE. A discrete-time FFE was simulated in Matlab and the choices of error covariances Q and R were discussed. Inspired by analyses on PLLs, we analyzed the steady-state performance of the continuous-time FFE and approximately derived its phase transfer function. The FFE is a feedback system and the output phase is decided by two paths, i.e., the control voltage x_3 the injection signals by P_{11} and P_{12}. The steady-state transfer function shows that the FFE is a second-order type-2 feedback loop. During the acquisition, the FFE has very large bandwidth, which can achieve fast settling. After acquisition, the bandwidth returns to a much smaller value. With a changeable bandwidth and relative constant damping factor, the FFE can break the tradeoff between loop

bandwidth and acquisition time.

This work is the first time that analog circuits are designed to implement a Kalman filter based frequency estimator. The internal structure of the FFE is divided into three main blocks: the main oscillator block performing the update of the state equations, the K and P matrix blocks providing the Riccati equation. We proposed both G_mC and LC structures, and the performances were simulated using the ideal Cadence SpectreRF model. Based on the ideal circuit model, several design constraints were discussed. First, very low corner frequency integrator and a loss compensated main oscillator are required to make FFE work. Then the frequency detuning tolerance between the main oscillator, K matrix and P matrix was simulated based on the G_mC structure, which showed that twice frequency detuning can be highly tolerated. Finally, the loss in K matrix was found to be able to improve the tolerance of frequency detuning and phase delay.

We then investigated the LC oscillator with injection and its dynamic amplitude and phase equations were derived. The LC quadrature oscillator was also studied from the view of the oscillator with injection signals. The equations for the main oscillator in the FFE also showed that it can be expressed as an oscillator with injections, which shares the same format of amplitude and phase equations with LC quadrature oscillator. Thus, a quadrature LC cross-coupled oscillator was proposed to implement the main oscillator. All the injection signals were generated by transconductance multipliers. Q factor is a key factor in the study of the LC oscillator. The LC tank impedance performance was further studied as it is related with the multi-phase sequence issue in the LC quadrature oscillator.

Compared with LC oscillators, ring oscillators have the advantages of compact layout and are easy to generate multiple phases. The 2-stage ring oscillator was studied and applied to the K matrix block. We then explored the simplified

implementation of the K and P matrix blocks. The phases of all the signals were studied to support the simplification in theory. Meanwhile, simulation results have demonstrated that the simplified P_{11} and P_{12} signals can maintain the same frequency, phase and amplitude curve trend. The implementation of x_3 was based on the concept of charge pump. The difference is that the control signals have brought in the variable P_{13} by multiplication. Finally, the whole FFE system was simulated and verified in Cadence SpectreRF with GlobalFoundries $0.13\mu m$ 8HP process.

In summary, this work leads to a conclusion that analog integrated circuits can be adopted to implement the EKF based FFE. Compared with the traditional type-2 PLL, the FFE can achieve much faster acquisition with a changeable loop dynamics. In particular, we have shown that the settling time for the second-order type-2 PLL of 2MHz bandwidth is around 3500 cycles, whereas for our simplified, preliminary, stable implementation of the FFE, the settling time is around 10 cycles.

There are some potential future work, namely: (1) solve the loading issue between each block, especially in the post-simulation of the layout; (2) investigate a main oscillator, whose amplitude could follow that of the input signal; (3) explore a larger acquisition range; (4) current implementation of the FFE is more complicated than a traditional PLL, and it is worthwhile to study a simpler implementation with lower noise.

Bibliography

[1] David Slepian. Estimation of signal parameters in the presence of noise. *Transactions of the IRE Professional Group on Information Theory*, 3(3):68–89, 1954.

[2] D.C.B.P. Rife and Robert Boorstyn. Single tone parameter estimation from discrete-time observations. *IEEE Transactions on information theory*, 20(5):591–598, 1974.

[3] Boualem Boashash. Estimating and interpreting the instantaneous frequency of a signal – part 2: Algorithms and applications. *Proceedings of the IEEE*, 80(4):540–568, 1992.

[4] Barbara F. La Scala and Robert R. Bitmead. Design of an extended kalman filter frequency tracker. *IEEE Transactions on Signal Processing*, 44(3):739–742, 1996.

[5] Sergio Bittanti and Sergio M Savaresi. On the parametrization and design of an extended kalman filter frequency tracker. *IEEE transactions on automatic control*, 45(9):1718–1724, 2000.

[6] Aurobinda Routray, Ashok Kumar Pradhan, and K. Prahallad Rao. A novel kalman filter for frequency estimation of distorted signals in power systems. *IEEE Transactions on Instrumentation and Measurement*, 51(3):469–479, 2002.

[7] Dan Simon. *Optimal state estimation: Kalman, H infinity, and nonlinear approaches*. John Wiley & Sons, 2006.

[8] Edward Victor Appleton. Automatic synchronization of triode oscillators. In *Proc. Cambridge Phil. Soc*, volume 21, page 1923, 1922.

[9] A. Grebene and H. Camenzind. Phase locking as a new approach for tuned integrated circuits. In *1969 IEEE International Solid-State Circuits Conference. Digest of Technical Papers*, volume 12, pages 100–101. IEEE, 1969.

[10] Simon Haykin. *Communication systems*. John Wiley & Sons, 2008.

[11] Pedro Rodríguez, Josep Pou, Joan Bergas, J Ignacio Candela, Rolando P Burgos, and Dushan Boroyevich. Decoupled double synchronous reference frame pll for power converters control. *IEEE Transactions on Power Electronics*, 22(2):584–592, 2007.

[12] Guan-Chyun Hsieh and James C Hung. Phase-locked loop techniques. a survey. *IEEE Transactions on industrial electronics*, 43(6):609–615, 1996.

[13] Floyd M Gardner. *Phaselock techniques*. John Wiley & Sons, 2005.

[14] R Jaffe and Eberhardt Rechtin. Design and performance of phase-lock circuits capable of near-optimum performance over a wide range of input signal and noise levels. *IRE Transactions on Information Theory*, 1(1):66–76, 1955.

[15] Long Kong and Behzad Razavi. A 2.4-ghz 6.4-mw fractional-n inductorless rf synthesizer. *IEEE Journal of Solid-State Circuits*, 52(8):2117–2127, 2017.

[16] JF Bellantoni and KW Dodge. A square root formulation of the kalman-schmidt filter. *AIAA journal*, 5(7):1309–1314, 1967.

[17] Paul Zarchan and Howard Musoff. *Fundamentals of Kalman filtering: a practical approach*. American Institute of Aeronautics and Astronautics, Inc., 2013.

[18] Rudolph Emil Kalman et al. A new approach to linear filtering and prediction problems. *Journal of Basic Engineering*, 82(1):35–45, 1960.

[19] S. Bittanti and AJ Laub. The riccati equation, 1991.

[20] M Sanjeev Arulampalam, Simon Maskell, Neil Gordon, and Tim Clapp. A tutorial on particle filters for online nonlinear/non-gaussian bayesian tracking. *IEEE Transactions on signal processing*, 50(2):174–188, 2002.

[21] R.S. Bucy P.D. Joseph. *Filtering for stochastic processes with applications to guidance*. Interscience, 1968.

[22] Richard S. Bucy and Peter D. Joseph. *Filtering for stochastic processes with applications to guidance*, volume 326. American Mathematical Soc., 2005.

[23] Thomas Kailath, Ali H Sayed, and Babak Hassibi. *Linear estimation*. Number BOOK. Prentice Hall, 2000.

[24] Behzad Razavi. *Monolithic phase-locked loops and clock recovery circuits: theory and design*. John Wiley & Sons, 1996.

[25] Behzad Razavi. *RF microelectronics*, volume 2. Prentice hall New Jersey, 1998.

[26] Floyd Gardner. Charge-pump phase-lock loops. *IEEE transactions on Communications*, 28(11):1849–1858, 1980.

[27] Alfreza Zolfaghari, Andrew Chan, and Behzad Razavi. A 2.4 ghz 34 mw cmos transceiver for frequency-hopping and direct-sequence applications. In *2001 IEEE International Solid-State Circuits Conference. Digest of Technical Papers. ISSCC (Cat. No. 01CH37177)*, pages 418–419. IEEE, 2001.

[28] Tai-Cheng Lee and Behzad Razavi. A stabilization technique for phase-locked frequency synthesizers. *IEEE journal of solid-state circuits*, 38(6):888–894, 2003.

[29] Amber Han-Yuan Tan and Gu-Yeon Wei. Adaptive-bandwidth mixing pll/dll based multi-phase clock generator for optimal jitter performance. In *IEEE Custom Integrated Circuits Conference 2006*, pages 749–752. IEEE, 2006.

[30] Tom A.D. Riley, Miles A. Copeland, and Tad A. Kwasniewski. Delta-sigma modulation in fractional-n frequency synthesis. *IEEE journal of solid-state circuits*, 28(5):553–559, 1993.

[31] Gennady A. Leonov, Nikolay V. Kuznetsov, Marat V. Yuldashev, and Renat V. Yuldashev. Hold-in, pull-in, and lock-in ranges of pll circuits: rigorous mathematical definitions and limitations of classical theory. *IEEE Transactions on Circuits and Systems I: Regular Papers*, 62(10):2454–2464, 2015.

[32] G.S. Moschytz. Miniaturized rc filters using phase locked loop. *Bell System Technical Journal*, 44(5):823–870, 1965.

[33] Alan B. Grebene. The monolithic phase-locked loop-a versatile building block. *IEEE spectrum*, 8(3):38–49, 1971.

[34] Asad A. Abidi. Phase noise and jitter in cmos ring oscillators. *IEEE journal of solid-state circuits*, 41(8):1803–1816, 2006.

[35] Robert Adler. A study of locking phenomena in oscillators. *Proceedings of the IRE*, 34(6):351–357, 1946.

[36] D.P.M. Millar. A two-phase audio-frequency oscillator. *Journal of the Institution of Electrical Engineers*, 74(448):365–371, 1934.

[37] E.L. Ginzton and LMx Hollingsworth. Phase-shift oscillators. *Proceedings of the IRE*, 29(2):43–49, 1941.

[38] Ahmad Mirzaei, Mohammad E Heidari, Rahim Bagheri, Saeed Chehrazi, and Asad A. Abidi. The quadrature LC oscillator: A complete portrait based on injection locking. *IEEE Journal of Solid-State Circuits*, 42(9):1916–1932, 2007.

[39] Ahmadreza Rofougaran, Jacob Rael, Maryam Rofougaran, and Asad Abidi. A 900 mhz cmos lc-oscillator with quadrature outputs. In *1996 IEEE International Solid-State Circuits Conference. Digest of Technical Papers, ISSCC*, pages 392–393. IEEE, 1996.

[40] Pietro Andreani, Andrea Bonfanti, Luca Romano, and Carlo Samori. Analysis and design of a 1.8-GHz CMOS LC quadrature VCO. *IEEE Journal of Solid-State Circuits*, 37(12):1737–1747, 2002.

[41] Gunhee Han and Edgar Sanchez-Sinencio. Cmos transconductance multipliers: A tutorial. *IEEE Transactions on Circuits and Systems II: Analog and Digital Signal Processing*, 45(12):1550–1563, 1998.

[42] J.J. Rael and Asad A. Abidi. Physical processes of phase noise in differential lc oscillators. In *Proceedings of the IEEE 2000 Custom Integrated Circuits Conference (Cat. No. 00CH37044)*, pages 569–572. IEEE, 2000.

[43] Emad Hegazi and Asad A. Abidi. Varactor characteristics, oscillator tuning curves, and am-fm conversion. *IEEE Journal of Solid-State Circuits*, 38(6):1033–1039, 2003.

[44] Heinrich Barkhausen. Lehrbuch der elektronenröhren und ihrer technischen anwendungen. 1963.

[45] Afshin Rezayee and Ken Martin. A coupled two-stage ring oscillator. In *Proceedings of the 44th IEEE 2001 Midwest Symposium on Circuits and Systems. MWSCAS 2001 (Cat. No. 01CH37257)*, volume 2, pages 878–881. IEEE, 2001.

[46] John G Maneatis and Mark A. Horowitz. Precise delay generation using coupled oscillators. *IEEE Journal of Solid-State Circuits*, 28(12):1273–1282, 1993.

[47] Woorham Bae, Haram Ju, Kwanseo Park, Sung-Yong Cho, and Deog-Kyoon Jeong. A 7.6 mw, 414 fs rms-jitter 10 ghz phase-locked loop for a 40 gb/s serial link transmitter based on a two-stage ring oscillator in 65 nm cmos. *IEEE Journal of Solid-State Circuits*, 51(10):2357–2367, 2016.

[48] Bassem Fahs, Walid Y. Ali-Ahmad, and Patrice Gamand. A two-stage ring oscillator in 0.13-m cmos for uwb impulse radio. *IEEE Transactions on Microwave Theory and Techniques*, 57(5), 2009.

[49] Behzad Razavi. The ring oscillator [a circuit for all seasons]. *IEEE Solid-State Circuits Magazine*, 11(4):10–81, 2019.

[50] A. Nader Mohieldin, Edgar Sánchez-Sinencio, and José Silva-Martínez. A fully balanced pseudo-differential ota with common-mode feedforward and inherent common-mode feedback detector. *IEEE journal of solid-state circuits*, 38(4):663–668, 2003.

[51] Woogeun Rhee. Design of high-performance cmos charge pumps in phase-locked loops. In *ISCAS'99. Proceedings of the 1999 IEEE International Symposium on Circuits and Systems VLSI (Cat. No. 99CH36349)*, volume 2, pages 545–548. IEEE, 1999.

[52] Behzad Razavi. A study of phase noise in cmos oscillators. *IEEE journal of Solid-State circuits*, 31(3):331–343, 1996.